Attosecond interferometry: techniques and spectroscopy

Kroon, David

2016

Attosecond interferometry: techniques and spectroscopy

David Kroon

Doctoral Thesis
2016

Lund University

Attosecond interferometry: techniques and spectroscopy

Printed in Sweden by Media-Tryck, Lund, 2016

Division of Atomic Physics
Department of Physics
Faculty of Engineering, LTH
Lund University
P.O. Box 118
SE–221 00 Lund
Sweden

http://www.atomic.physics.lu.se

ISSN 0281-2762
Lund Reports on Atomic Physics, LRAP 514 (2016)

ISBN (print): 978-91-7623-688-8
ISBN (pdf): 978-91-7623-689-5

Till Egon

Abstract

The interaction between an intense laser pulse and a gas medium leads to the emission of coherent bursts of light in the extreme ultra violet range. This process, known as high-order harmonic generation, has today, almost three decades after its discovery, developed into a reliable source of extremely short ($\sim$100 as, 1 as=10^{-18} s) pulses of electromagnetic radiation, with a wide range of applications in the atomic, molecular and optical sciences. The access to radiation with attosecond duration opens up new possibilities for studying and even controlling electronic processes that takes place on this timescale.

This thesis presents a series of experiments where sequences of attosecond pulses, attosecond pulse trains, are used to perform photoelectron interferometry. Free electronic wave packets, launched via photoabsorption of a coherent train of ionizing attosecond pulses, are manipulated by an infrared laser field and brought to interfere. From the resulting interferogram the phase of the escaping wave packets can be partly reconstructed. This phase in turn carries a signature of the interactions that lead to the ejection of the electron. Under certain conditions the measured phase can be related to a delay of the wave packet, corresponding to the time it takes for it to escape the ionic binding potential, called photoionization time delay.

This method was applied to a range of atomic systems and ejection mechanisms in order to study the influence of atomic electronic structure on the ejection of electrons. Since the composition of the electronic wave packets is partly determined by the temporal structure of the ionizing radiation, a comparative approach was applied to isolate the effect of the ion-electron interactions. The photoionization time delay for ionization from the $3s$ subshell of argon was measured relative to that of the $3p$ shell. In another experiment the delay of a two electron wave packet resulting from double ionization of xenon was referenced to single ionization from the valence shell. In an iterative measurement procedure, interferograms were cross-referenced from ionization of the valence shells of argon, helium and neon. Finally, the significant phase distortion resulting from an autoionizing resonance in argon was mapped out by stepwise tuning the central frequency of the exciting pulse train.

The interferometric method was also utilized to study the temporal synchronization between the attosecond pulse train and the laser pulse used to produce it. The results show that the synchronization is dependent on the density of the gaseous medium due to the specific dispersion properties of the gas.

Populärventsakplig sammanfattning

Egenskaperna hos de material som utgör och omger oss, som t.ex. färg, struktur och kemiska egenskaper, bestäms av hur elektronerna som är en del av dess byggstenar, atomerna, är strukturerade. Ett sätt att undersöka elektronstrukturen är med hjälp den fotoelektriska effekten. Ljus, elektromagnetiska fält, kan beskrivas som en ström av ljuspartiklar, fotoner, som alla bär på en bestämd mängd energi. Den fotoelektriska effekten är den process där en foton, med tillräckligt hög energi, absorberas av atomen och en (eller flera) elektron(er) frigörs. Genom att mäta rörelseenergin hos de elektroner som kommer ut, får man reda på hur starkt bundna de är till atomen. Att studera elektronernas energi ger tyvärr bara begränsad kunskap om hur det går till när elektronenrna lossnar.

I den här avhandlingen beskrivs experiment där extremt korta ljusblixtar med våglängder inom det extrem-ultravioletta området, s.k. attosekundspulser (as, 1 as=10^{-18} s), utnyttjats för att studera hur växelverkan mellan atomkärnan och elektronen påverkar tidsförloppet då elektronen slits loss. Vidare har processen att generera attosekundspulser studerats, detta i syfte att svara på frågan hur precisa den här sortens experiment kan göras. Metoden som använts utnyttjar materiens vågnatur i den mikroskopiska världen och kan beskrivas som interferometi med elektroner.

Attosekundspulser

En sekvens av attosekundspulser, ett pulståg, skapas när man fokuserar en stark laserpuls in en gas. Mekanismen bygger på att de yttersta elektronerna i atomerna plötsligt blir fria då den elektriska kraften med vilken laserpulsen påverkar atomerna övervinner den kraft som binder elektronerna till atomen. Styrkan och riktningen på kraften varierar dock periodiskt, varför de fria elektonerna inom en kort tidsram (1.6 fs, 1 fs=10^{-15}s) drivs tillbaka och kolliderar med atomen. Kollisionen ger upphov till en ljusblixt med en varaktighet på bara ett hundratal attosekunder. Det faktum att alla atomer i gasen påverkas på samma sätt, det vill säga ljusblixtarna avges samtidigt, gör att alla ljusvågorna svänger likadant, man säger att de är koherenta. Koherens är en förutsättning för att ljuspulserna ska kunna användas till experimenten som beskrivs i den här avhandlingen. Till exempel visade ett av experimenten i avhandlingen att synkroniseringen mellan attosekundspulserna och laserpulsen som skapar dem, påverkas av densiteten hos gasen i vilken de genereras.

Interferometri med elektroner

På mikroskopisk nivå beskrivs all materia som vågor. Efter det att en elektron frigjorts från en atom fortplantar sig dess vågrörelse och sprids likt det som sker när en droppe träffar en vattenyta. Lokalt, nära atomkärnan störs dock vågrörelsen av de krafter som verkar mellan atomkärnan, elektronen och de övriga elektornerna som är bundna till atomen. Detta ändrar hur elektronvågorna ser ut då de detekteras långt borta från atomen, det ändrar när dalarna och topparna kommer. Kvantmekaniken, som beskriver den mikroskopiska världen, säger oss dock att sådana s.k. fasskiften inte är direkt mätbara. Istället måste vi utnyttja en teknik som kallas interferometri. När två vågor med samma våglängd adderas blir resultatet en ny våg, vars våglängd är den samma men vars amplitud beror på var vågdalarna och vågtopparna befinner sig relativt varandra hos de ursprungliga vågorna. Denna process kan vi åstadkomma genom att ändra våglängden hos de ursprungliga elektronvågorna något, med hjälp av en infraröd laserpuls. Genom att mäta amplituden hos de resulterande vågorna går det alltså att mäta hur mycket en våg är skiftad i förhållande till en annan. Vågamplituder är direkt mätbara eftersom de är proportionella mot sannolikheten att vår detektor registrerar en elektron med en viss kinetisk energi. Dessa resultat kan sedan jämföras med förutsägelser från teoretiska modeller av atomens elektronstruktur och man kan dra slutsatser om vilka mekanismer i dessa komplexa system som spelar stor roll och vilka man eventuellt kan bortse ifrån. Samma teknik kan också användas för att karakterisera sekvenser av attosekundspulser, eftersom karakteristiken hos pulserna påverkar sammansättningen av elektronvågen.

List of Publications

This thesis is based on the following papers, which will be referred to by their roman numerals in the text.

I **Photoemission-time-delay measurements and calculations close to the 3s-ionization-cross-section minimum in Ar**
D. Guénot, K. Klünder, C. L. Arnold, D. Kroon, J. M. Dahlström, M. Miranda, T. Fordell, M. Gisselbrecht, P. Johnsson, J. Mauritsson, E. Lindroth, A. Maquet, R. Taïeb, A. L'Huillier and A. S. Kheifets.
Phys. Rev. A **85**, 053424 (2012).

II **Measurements of relative photoemission time delays in noble gas atoms**
D. Guénot, D. Kroon, E. Balogh, E. W. Larsen, M. Kotur, M. Miranda, T. Fordell, P. Johnsson, J. Mauritsson, M. Gisselbrecht, K. Varjú, C. L. Arnold, T. Carette, A. S. Kheifets, E. Lindroth, A. L'Huillier and J. M. Dahlström.
J. Phys. B **47**, 245602 (2014).

III **Double ionization probed on the attosecond timescale**
E. P. Månsson, D. Guénot, C. L. Arnold, D. Kroon, S. Kasper, J. M. Dahlström, E. Lindroth, A. S. Kheifets, A L'Huillier, S. L Sorensen and M. Gisselbrecht.
Nat. Phys. **10**, 207-211 (2014).

IV **Attosecond pulse walk-off in high-order harmonic generation**
D. Kroon, D. Guénot, M. Kotur, E. Balogh, E. W. Larsen, C. M. Heyl, M. Miranda, M. Gisselbrecht, J. Mauritsson, P. Johnsson, K. Varjú, A. L'Huillier and C. L. Arnold.
Opt. Lett. **39**, 2218-2221 (2014).

V **Spectral phase measurement of a Fano resonance using tunable attosecond pulses**
M. Kotur, D. Guénot, Á. Jiménez-Galán, D. Kroon, E. W. Larsen, M. Louisy, S. Bengtsson, M. Miranda, J. Mauritsson, C. L. Arnold, S. E. Canton, M. Gisselbrecht, T. Carette, J. M. Dahlström, E. Lindroth, A. Maquet, L. Argenti, F. Martín and A. L'Huillier.
Accepted for publication in Nat. Commun.

VI **Efficient high-order harmonic generation boosted by below-threshold harmonics**
F. Brizuela, C. M. Heyl, P. Rudawski, D. Kroon, L. Rading, J. M. Dahlström, J. Mauritsson, P. Johnsson, C. L. Arnold and A. L'Huillier.
Sci. Rep. **3**, 1410 (2013).

VII **Seeded Coherent Harmonic Generation with in-line Gas Target**
F. Curbis, N. Cutic, O. Karlberg, F. Lindau, E. Mansten, S. Thorin, S. Werin, F. Brizuela, B. Kim, D. Kroon, A. L'Huillier and M. Gisselbrecht.
Proceedings International Free Electron Laser Conference 2012.

VIII **Multi-purpose two- and three-dimensional momentum imaging of charged particles for attosecond experiments at 1 kHz repetition rate**
E. P. Månsson, S. L. Sorensen, C. L. Arnold, D. Kroon, D. Guénot, T. Fordell, F Lépine, P. Johnsson, A. L'Huillier and M. Gisselbrecht.
Rev. Sci. Instrum. **85**, 123304 (2014).

Abbreviations

APT	Attosecond Pulse Train
CPA	Chirped Pulse Amplification
CW	Continuous Wave
FEL	Free-Electron Laser
FWHM	Full-Width at Half-Maximum
HHG	High-order Harmonic Generation
IR	Infrared
KLM	Kerr-Lens Modelocking
MBES	Magnetic Bottle Electron Spectrometer
MCP	Microchannel Plate
RABBITT	Reconstruction of Attosecond Beating By Interference of Two-photon Transitions
SFA	Strong-Field approximation
SPIDER	Spectral Phase Interferometry for Direct Electric-field Reconstruction
TDSE	Time-Dependent Schrödinger Equation
TOF	Time Of Flight
XUV	Extreme Ultraviolet ($10 < \hbar\omega < 124$ eV)

Contents

Abstract **v**

Populärventsakplig sammanfattning **vii**

1 Introduction **1**
1.1 A brief background . . . 1
1.2 The atomic time-scale . . . 2
1.3 Electron interferometry . . . 2
1.4 Papers and outline . . . 3

2 High-order Harmonic Generation **5**
2.1 Introduction . . . 5
2.2 Production of high-power ultrashort optical laser pulses . . . 7
2.3 Laser-atom interaction . . . 10
2.3.1 The weak field regime . . . 11
2.3.2 The strong field regime . . . 12
2.4 Macroscopic ensemble effects - Phase matching . . . 17
2.4.1 Controlling phase-matching . . . 20
2.5 High-order harmonics and attosecond pulses . . . 24

3 Photoelectron interferometry **31**
3.1 Photoelectron spectroscopy . . . 31
3.2 Photoelectron interferometry - The RABBITT technique . . . 32
3.2.1 Applications of RABBITT . . . 34
3.2.2 Conditions for RABBITT . . . 35
3.3 Detection of photoelectrons . . . 37
3.4 Optical interferometers for photoelectron interferometry . . . 39
3.4.1 Old setup . . . 39
3.4.2 New setup . . . 43

4 Atomic phases and time delays **47**
4.1 Time delays of scattering wave packets . . . 47
4.2 Time delays in photoemission . . . 48
4.3 Measuring time delays in photoemission . . . 49
4.3.1 Electron correlation and angular channels . . . 51
4.4 Experiments and results . . . 52
4.4.1 Comparing ionization form subshells of argon . . . 53
4.4.2 Comparing ionization from valence shells of noble gas atoms . . . 54
4.4.3 Comparing double and single ionization from xenon . . . 55
4.4.4 Measuring the phase variation across a Fano resonance . . . 57

5 Summary and Outlook **61**
5.1 Summary . . . 61
5.2 Outlook . . . 62

Comments on the papers **65**

Acknowledgments **67**

References **77**

Papers

I **Photoemission-time-delay measurements and calculations close to the 3s-ionization-cross-section minimum in Ar** **79**

II **Measurements of relative photoemission time delays in noble gas atoms** **89**

III **Double ionization probed on the attosecond timescale** **101**

IV **Attosecond pulse walk-off in high-order harmonic generation** **108**

V **Spectral phase measurement of a Fano resonance using tunable attosecond pulses** **115**

VI **Efficient high-order harmonic generation boosted by below-threshold harmonics** **123**

VII **Seeded Coherent Harmonic Generation with in-line Gas Target** **130**

VIII **Multi-purpose two- and three-dimensional momentum imaging of charged particles for attosecond experiments at 1 kHz repetition rate** **136**

Chapter 1

Introduction

1.1 A brief background

The development of attosecond science sprung from the experimental discovery of the generation of high-order harmonics [1, 2]. When atoms were exposed to an intense laser field, optical frequency up-conversion was observed yielding higher harmonic orders than ever reported before, and higher than what was expected from the understanding of the mechanisms of non-linear optics at that time. The light emission thus generated was found to be confined in a narrow angular region around the forward direction of the generating laser beam and restricted to narrow spectral regions, centered around odd order harmonics of the driving laser frequency.

These properties give the light generated through high-order harmonic generation a high spectral brightness, compared to other types of table-top sources in the VUV/XUV spectral range. Thus, despite a relatively low conversion efficiency, it was directly realized that this process had potential for spectroscopic applications.

What was not directly apparent in the first experimental observations was the prospect of achieving light emission temporally confined down to $\sim$100 as (1 as=10^{-18} s), that is, on a timescale much shorter than the driving laser pulse. The understanding of this temporal confinement grew out of further experimental and theoretical work. While it was explicitly proposed in 1992 that high-order harmonics can be used to produce attosecond pulses [3], it was not experimentally demonstrated until 2001 [4]. This discovery gave rise to a rich flora of applications for this light source (for contemporary overviews, see Refs. [5–9]).

The new scientific field that developed around the high-order harmonic generation (HHG) technique is called attosecond science, due to the timescales one can access with these short duration electromagnetic pulses. With light bursts with a duration on the order of 100 as, the current world record of characterized attosecond pulse being 67 as [10], the timescale of electronic dynamics in atoms and molecules is within reach.

1.2 The atomic time-scale

To understand why attosecond pulses allow us to time resolve electronic processes in atoms, we consider the atomic valence states, where the typical energy spacing is on the order of 10 eV. Dynamics in a quantum system can in general be described by the time evolution of a superposition of stationary states. Thus if the system is left in a superposition of states a and b at a at $t = 0$, with spatial wave functions $\varphi_a(r)$ and $\varphi_b(r)$ and corresponding energies E_a and E_b, the wave function evolves as,

$$\Psi(r,t) = c_a\varphi_a(r)e^{-i\frac{E_a}{\hbar}t} + c_b\varphi_b(r)e^{-i\frac{E_b}{\hbar}t}, \tag{1.1}$$

where c_a and c_b are complex, possibly time dependent numbers. We ignore the time dependence of c_a and c_b in a first approximation. The electronic probability density can be written as,

$$|\Psi(r,t)|^2 = |c_a\varphi_a(r)|^2 + |c_b\varphi_b(r)|^2 + 2|c_a\varphi_a(r)c_b\varphi_b(r)|\cos[(\omega_a - \omega_b)t + \Delta\phi_{ab}], \tag{1.2}$$

where $E_{a,b}/\hbar$ has been replaced by $\omega_{a,b}$ and $\Delta\phi_{ab}$ is a phase originating from the fact that $c_{a,b}$ and $\varphi_{a,b}(r)$ are complex quantities. Equation 1.2 indicates that the relevant timescale in these dynamics, i.e. the timescale on which the charge distribution actually moves, is on the order of $2\pi/(\omega_a - \omega_b)$. Assuming that the energy spacing between the involved states is 10 eV this time amounts to about 400 as.

It is possible to catch this motion in a so called pump-probe experiment, where a short pump pulse initiates the dynamics and a delayed probe pulse gives rise to a signal which depends on the instantaneous charge distribution. For the fast motion mentioned above, pump and probe pulses must have a duration less than 400 as. Furthermore the control of these pulses, in terms of when they arrive on target, would have to have an uncertainty of less than or on the same order of magnitude as the pulses themselves. If these two criteria are not met, the resulting experimental signal becomes an average over a time that exceeds the period of the last term in eq. 1.2. Since the time average over the cosine is zero, such an experiment would only capture some aspects of the static charge distribution.

Pump-probe experiments using attosecond pulses, where the outcome can be interpreted and understood directly in terms of a time evolution of bound state superpositions or bound wave packet formation have been performed [11–13]. In these studies, a short pulse generated by the HHG process serves as either a pump pulse, starting the dynamics, or as a probe pulse, creating an observable outcome such as electron emission or molecular fragmentation by photoionization.

1.3 Electron interferometry

The time evolution of $\Psi(r,t)$ can also be determined from its Fourier transform, $\Phi(r,\omega)$. To retrieve the time evolution from the spectral information it is necessary to know both the spectral amplitude and the spectral phase. Measuring spectral amplitudes has been done for decades with, for example, photoelectron spectroscopy in combination with synchrotron radiation sources. Maybe one of the major achievements of attosecond science is to provide the means to measure spectral phases.

The experimental method applied throughout in this thesis is based upon photoelectron interferometry. The method was originally suggested in 1996 [14] and demonstrated in 2001 [4, 15] when it was launched under the acronym RABBITT (Reconstruction of Attosecond Beating By Interference of Two-photon Transitions). Conceptually, this method has a great deal in common with a method for the characterization of optical wave packets, or pulses, based on spectral interferometry, known by the acronym SPIDER [16].

Briefly, the RABBITT technique uses the frequency comb of high-order harmonics and a delayed infrared field. These two fields are lead to ionize an atomic gas and induce quantum interferences in the photoelectron signal. From these interferences the spectral phase variation of the photoionization amplitude can be recovered. This technique does not require isolated pump and probe attosecond pulses. Interestingly, the time resolution that can be obtained is not limited by the pulse duration of the attosecond pulses but rather by the precision of the optical interferometer controlling the delay between the two fields (below 50 as), and the resolution of the photoelectron spectrometer.

In this thesis photoelectron interferometry has been used to study the dynamics of both single- and double photoionization, including ionization in the vicinity of a resonance.

1.4 Papers and outline

This thesis is based on eight papers. Papers **I**, **II**, **III** and **V** present studies of photo ionization dynamics for various atoms and electron ejection mechanisms. The results presented in Paper **I** complement the measurements in [17]. The results are also presented together with a more elaborate theoretical interpretation. In Paper **II** photoionization time delays from the outer valence shell of different noble gas atoms are compared. In Paper **III** it is demonstrated how photoelectron interferometry can be applied to measure an ionization delay of a two electron wave packet resulting from double ionization. Paper **V** presents a measurement of the phase distortion that an autoionizing state causes on an ionized wave packet.

This thesis also presents work that is concerned with exploring certain aspects of the HHG light source. Paper **IV** is an investigation of the effect of the density of the harmonic generation medium on the temporal synchronization between the emitted radiation and the driving laser field. In Paper **VI** it is demonstrated how low order harmonics generated from a gas target can enhance the high order harmonic generation from a second gas target. Paper **VII** is a feasibility study of a scheme for seeding a free-electron laser with harmonics of a high-power laser generated form a gas target. Finally, Paper **VIII** describes the design an tests of a charged particle momentum imaging spectrometer, designed for attosecond experiments.

The outline of this thesis is as follows. Chapter 2 contains an introduction to the fundamentals of HHG. The physical processes involved in the generation are explained as well as how these processes can be optimized to best serve the purposes of attosecond science. Chapter 3 describes photoelectron interferometry, the main experimental method used during this thesis work, and how it was implemented. In Chapter 4, experiments carried out using this technique are described and discussed in detail.

These experiments have in common that they are designed to extract information about the dynamics of photoionization. Finally, Chapter 5 gives a summary and an outlook.

Chapter 2

High-order Harmonic Generation

This chapter introduces non-linear optics from a strong field perspective. The possibility of non-linear frequency conversion through laser-matter interaction has been known of since the 1960's, when Franken and co-workers demonstrated second harmonic generation in quartz [18]. For their experiment they used the first working laser, based on a flash-lamp pumped Ruby crystal, invented by Mainman just the year before [19]. The maximum field strength achievable with this laser, quoted by Franken, was on the order of 10^3 V/m. In the HHG process non-linear frequency conversion is driven to the extreme, and thus into a different physical regime.

2.1 Introduction

As mentioned above, HHG is a process that results from laser-matter interaction, but can only occur if the laser field is sufficiently strong. What is considered a strong field is of course somewhat dependent on the target in question. In this thesis only HHG from neutral atomic species in gas phase will be considered. This method of generating short wavelength light has proven, thus far, to be superior to harmonic sources based on other targets, in terms of conversion efficiency and pulse quality. The field intensity required to drive this process is on the order of 10^{14} W/cm^2, which in vacuum corresponds to a field strength of about $3{\cdot}10^{10}$ V/m. This field strength is sufficient to substantially distort the static electric field that confines the valence electrons in an atom.

To achieve these high field strengths in a laboratory the available laser energy has to be concentrated, i.e. confined, in both time and space. The transversal confinement of a laser beam is easily achievable by focusing it using a curved mirror or a lens. There are however both a practical and a theoretical limit to how small a laser beam spot can be focused.

The longitudinal and temporal confinement is obtained by the production of pulsed light. The shorter the driving pulse the less energy per pulse is required to achieve a given intensity. This relaxed requirement can be utilized to increase the repetition rate of the experiment [20–22] without having to significantly increase the average output power. Short laser pulses, limited to just a few optical cycles, are also instrumental

in producing isolated attosecond pulses [6]. Multiple cycle driving pulses result, as we shall see, in a train of attosecond pulses. The development of HHG sources are thus closely interlinked with the progress of short pulse laser technology.

The laser system used in all experiments presented in this thesis delivers pulses with a central wavelength of 800 nm and a typical energy of 3 mJ available for harmonic generation, at a repetition rate of 1 kHz. Typical parameters for the focusing geometry is a 1 inch beam diameter and a focal-length of 50 cm. Given diffraction limited focal conditions, this gives a focal spot with a diameter of about 200 microns and an average fluence of 1 J/cm^2. This puts a restriction on the laser pulse duration of the order tens of fs to reach the required intensities over a significant volume. At its current state this system can produce pulses with a FWHM duration of 20 fs. From a contemporary attosecond science perspective this is relatively long, since a vacuum wavelength of 800 nm corresponds to a field cycle time of 2.7 fs. It is most definitely a multi-cycle pulse.

This system relies on femtosecond laser technology which is now standard in many research laboratories. Its key concepts are a Ti:Sapphire based Kerr-lens mode-locked (KLM) laser oscillator [23, 24] combined with an amplifier chain working along the principles of chirped pulse amplification (CPA)[25], both of which will be briefly described in the next section.

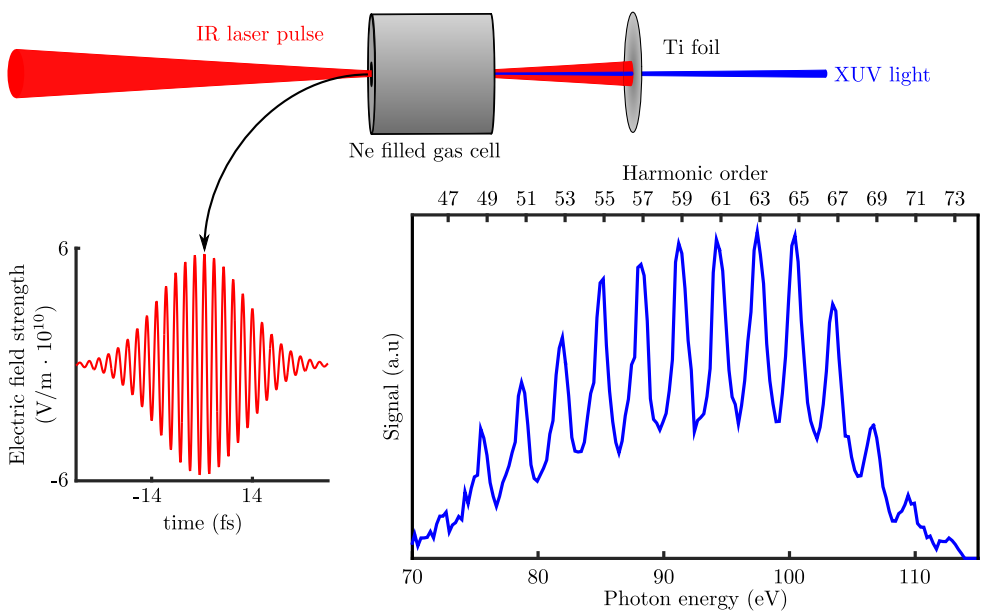

Figure 2.1: Illustration of HHG in neon gas. The displayed spectrum was retrieved using a flat field grating spectrometer after the generated light had been spectrally filtered through a thin Ti foil. The displayed laser pulse is a rough estimate of the pulse used in the experiment, based on a pulse length measurement and the cut-off frequency of the harmonic spectrum, which allowed us to estimate the laser intensity (see eq. 2.9). A Gaussian pulse shape was assumed.

Figure 2.1 illustrates how an HHG source based on a gas target is operates using an example where the aim was to generate photons in the energy range of 100 eV.

The NIR laser pulse was focused in to a open ended cell filled with neon gas. After the harmonic beam passed though a 200 nm thick titanium foil it was spectrally dispersed using a flat field grating spectrometer. The foil serves two purposes. It acts as a spectral filter, in this case a high-pass filter, in order to only allow the spectral components relevant for the experiment to propagate to the experimental vacuum chamber further downstream. It also allows us to remove the intense IR light from the beam, which otherwise would interfere with the experiment.

As is evident from the spectrum presented in the Fig. 2.1, the spectral structure of the emitted radiation consists in regularly spaced peaks centered around the odd-order harmonics of the frequency of the IR laser pulse. The central peaks are of comparable strength, indicating that they belong to the so called harmonic plateau. This term originates from the generic shape of an HHG spectrum, which divide into three characteristic energy regions. For the low-order harmonics the peak strength drops rapidly with increasing photon energy. Between this region and an abrupt cut-off on the high energy side, the harmonic peak strength is more or less constant.

Before turning to the details of the laser-atom interaction responsible for the emission of these high energy photons, a brief overview of high-power laser technology is given.

2.2 Production of high-power ultrashort optical laser pulses

Laser systems producing pulses with an mJ pulse energy and an fs duration yield peak powers in the TW range. Such systems are commercially available today and widely used in laser laboratories. The enabling concepts of femtosecond laser systems were developed during the 1980's and led to a leap in technology in the early 1990's, when these concepts were combined. For a more exhaustive overview than presented here see, for example, [26].

Ti:sapphire

The titanium ion (Ti^{3+}) doped sapphire (Al_2O_3) crystal, investigated by Moulton [27] in the 1980's, has qualities that make it an excellent laser gain medium for production and amplification of short intense pulses. Its gain profile, which peaks around 800 nm, spans more than 400 nm and thus supports production of very short pulses. It also has a good quantum efficiency, meaning that the pump energy is efficiently transferred into to laser light. Furthermore, the sapphire crystal has high thermal conductivity, which facilitates removal of excess heat, which could otherwise damage the crystal. The laser transition can be pumped at wavelengths around 530 nm, which matches well with frequency doubled Nd-ion or Yt-ion based solid state lasers.

Kerr-lens mode-locking

In order to utilize the broad amplification bandwidth of the Ti:sapphire crystal for short pulse production the laser oscillator has to allow for a large number of longitudinal modes to lase simultaneously. The individual modes also need to have a well-defined phase relation in order for their superposition to add up to a traveling pulse inside the cavity (see discussion in sec. 2.5). In a conventional resonator, differences in gain and losses between the modes leads to that the lasing is limited to

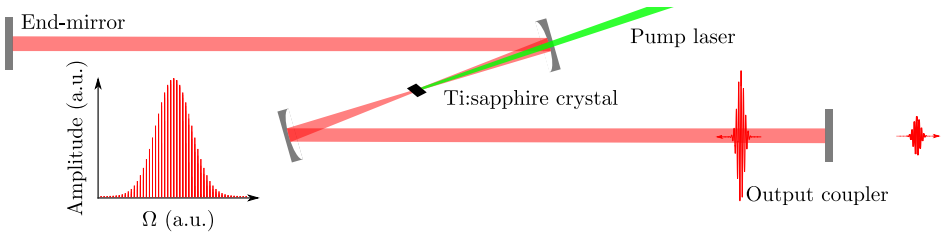

Figure 2.2: Schematic outline of a z-shaped Ti:sapphire mode-locked oscillator.

a narrow bandwidth. This limitation can however be circumvented by a careful design of the laser cavity and utilization of an optical non-linearity in the laser gain medium. The optical Kerr effect is a third order non-linear effect (see sec. 2.3.1) which makes the refractive index intensity dependent. As a result, the gain medium will act as a lens. The strength of this effect depends on the instantaneous intensity. When the light energy is temporally confined, the Kerr-lens will significantly influence the transversal cavity modes. A mode-locked oscillator is thus deigned to meet the stability conditions, and to induce both minimum losses and maximum gain on the transversal modes induced by the Kerr-lens. Once a short pulse is produced, the oscillator remains mode-locked, as long as the round-trip gain and losses favor mode-locked operation. To achieve mode-locked operation of the oscillator, a short pulse thus has to spontaneously appear. This can be achieved, for example, by randomly inducing different transient states in the cavity by swiftly shifting the cavity end-mirror out of position and back again. Once one of the transients happens to be a short pulse, the oscillator is mode-locked. Figure 2.2 shows a schematic outline of a z-shaped Ti:sapphire mode-locked oscillator. This construction would, however, not support pulses of fs duration. In order to do that, the dispersion of the pulse while traveling inside the cavity, has to be compensated for. This can be achieved by, for example, introducing chirped mirrors, combined with tunable dispersive elements (wedges or prisms), in the cavity [28, 29]. Properly dispersion-compensated mode-locked Ti:sapphire oscillators can support pulses of sub 10 fs approaching the NIR single optical cycle limit [30].

Chirped pulse amplification

The output pulse energy from a mode-locked oscillator is typically limited to a few nJ. In order to reach TW peak powers the pulses have to be amplified by a factor of 10^6-10^7. Such high peak powers are however difficult to handle in an amplifier chain. Due to practical constraints on the size of the amplification crystals and optical components, the fluence quickly exceeds their damage thresholds. Furthermore, non-linear propagation, caused by high peak intensities, can heavily distort the time-structure of the pulses. This problem can be circumvented by strongly chirping the pulses, in a controlled manner, before they are amplified. Using carefully aligned dispersive elements, for example a grating or a grating pair in combination with imaging optics, pulses with a duration of a few fs can be stretched to ∼100 ps. After amplification, the reverse operation can then be applied to re-compress the pulses in time.

Figure 2.3 illustrates the principle of chirped pulse amplification. The ideal spectral

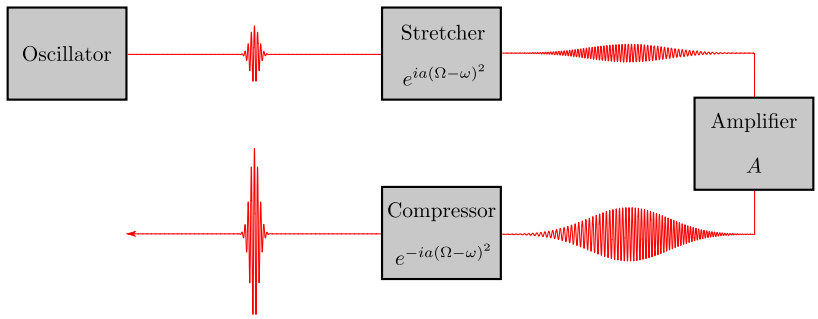

Figure 2.3: Schematic overview of an ideal CPA laser-chain.

transfer function of each unit in the chain is indicated. The stretcher adds a phase that is a quadratic function of the angular frequency Ω and symmetric with respect to the central angular frequency of the pulse, ω. After amplification with a factor A, which ideally is independent of frequency, the initial spectral phase is restored by the compressor. The chirp rate (a) and the amplification factor in the figure are merely illustrative; in reality they are many orders of magnitude larger.

Two common types of amplifiers used in CPA-laser chains are the multi-pass and the regenerative amplifier. In the multi-pass amplifier, the pulse is guided multiple times through the pumped gain medium from slightly different angles. In the regenerative amplifier the gain medium is instead contained in a cavity. The pulse is switched in and out of the cavity using a combination of reflective polarizers and pockel-cells that rotates the polarization of the pulse when high voltage is applied.

The 1kHz laser in Lund

The laser system used for retrieving the experimental results in Papers **I**, **II**, **III**, **IV** and **V** is described here. During this thesis work the laser system underwent a substantial upgrade, yielding more output power and shorter pulses. This description applies to the current state of the system.

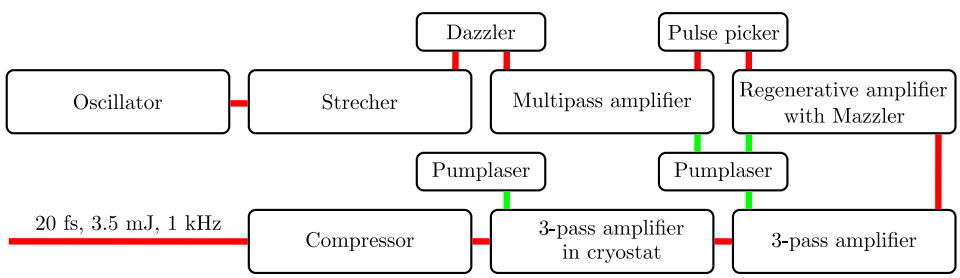

Figure 2.4: Schematic outline of the 1kHz CPA laser-chain in Lund.

The CPA laser chain, schematically outlined in Fig. 2.4, is seeded with a 76 MHz pulse train from a KLM-mode-locked Ti:sapphire, "Rainbow", oscillator built by Femtolasers. The pulses, that originally have a duration of 7 fs and a pulse energy of

2.5 nJ, are stretched using a configuration of a single grating and reflective imaging optics [31]. Before being amplified the seed pulses are reshaped in an acousto-optic programmable dispersive filter (AOPDF, a Dazzler from Fastlite). In normal operation this device is used for correcting errors in the spectral phase, introduced in the process of stretching, amplifying and compressing, such that a Fourier-transform limited pulse is retrieved at the end of the laser-chain. The Dazzler can, however, also be used to selectively limit the bandwidth of the seed pulse, which in addition of generating a slightly longer pulse after compression, makes it possible to tune its carrier frequency (see Paper **V**).

Two diode pumped, Q-switched and frequency doubled Nd:YAG lasers pump the Ti:sapphire crystals in four different amplification stages at a repetition rate of 1 kHz. After initial amplification in the multi-pass amplifier, to about 250 nJ, the pulse is "cleaned" by a pulse-picker and switched in to the cavity of the regenerative amplifier. This cavity contains another AOPDF (a Mazzler, also from Fastlite), operating as a spectral amplitude filter, whose purpose is to counteract gain-bandwidth-narrowing. Since the Ti:sapphire gain profile peaks around 800 nm, the Mazzler attenuates these spectral components after each pass through the gain medium, in order to achieve a flat round-trip gain profile. After 14 round-trips in the regenerative amplifier, the pulse is switched out, containing an energy of about 0.5 mJ, and is further amplified in two 3-pass amplifiers to a final energy of typically 6 mJ. The pulse is then re-compressed via a double pass on a grating pair in a parallel configuration according to the methods developed in [32, 33]. After compression the pulse energy is about 3.5 mJ. The spectral bandwidth of the amplified pulses is close to 100 nm, which supports a Fourier transform limited pulse duration of 20 fs. Alternatively, the bandwidth can be limited to 50 nm and the central wavelength tuned to between 780 and 830 nm, as shown if Fig. 2.5.

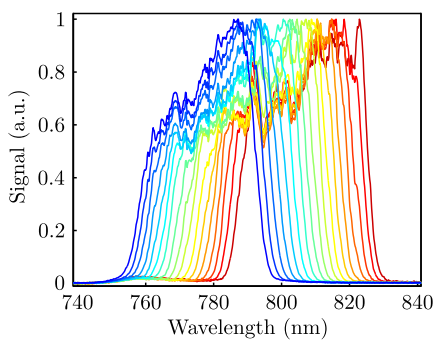

Figure 2.5: Normalized spectra, demonstrating the tuning of the central wavelength from the laser-chain using the Dazzler.

2.3 Laser-atom interaction

The interaction between optical light and atoms is well described within the dipole approximation. Light propagating through a medium will induce dipole moments along its path via the force exerted by the electric field on bound electrons. In classical

physics the radiation emitted from an oscillating dipole is proportional to the dipole acceleration, or to the second order time derivative of the dipole moment. When an ensemble of atoms is considered the corresponding quantity is called the polarization density, $\mathbf{P}$, which is proportional to the sum of the individual atomic dipole moments. From this perspective it is intuitive that the second order time derivative of the polarization density plays the role of a self induced source term in the electric field wave equation for propagation in a non-magnetic material,

$$\nabla^2\mathbf{E} - \frac{1}{c_0}\frac{\partial^2\mathbf{E}}{\partial t^2} = \mu_0 \frac{\partial^2\mathbf{P}}{\partial t^2} \tag{2.1}$$

For a coherent ensemble of atoms the polarization density can be calculated via the quantum mechanical correspondence to a classical dipole which is related to the time-dependent expectation value of the position operator $\hat{r}$,

$$\mathbf{P}(t) = Ne\langle\Psi(t)|\hat{r}|\Psi(t)\rangle, \tag{2.2}$$

where N is the number density of atoms and $\Psi(t)$ is the atomic wave function of the atom *dressed* by the light field. In this way the quantum mechanical Schrödinger equation is coupled to the Maxwell equations.

2.3.1 The weak field regime

If the dressing field strength is weak, in the sense that the dominating interactions are those between the electrons and the atomic core and among the electrons, then time-dependent perturbation theory provides a tool to solve the quantum-mechanical problem.

In applying this approach, the starting point is the Schrödinger equation,

$$i\hbar\frac{\partial|\Psi(t)\rangle}{\partial t} = (\hat{H}_0 + \lambda e\mathbf{E}(t)\cdot\hat{r})|\Psi(t)\rangle, \tag{2.3}$$

where $\hat{H}_0$ is the unperturbed Hamiltonian, $\mathbf{E}(t)$ the dressing electric field and λ is a scalar parameter that controls the strength of the perturbation. This approach guarantees a smooth deformation from the unperturbed state as the strength of the perturbation increases from zero. Given that the electric field is not driving the atom at a frequency close to a resonance, the system can be assumed to remain in its ground state. The anzats for the perturbed ground state wave function is that it can be expanded as a power series of λ in the basis set of the unperturbed Hamiltonian, $|\phi_n\rangle$

$$|\Psi(t)\rangle = a_0|\phi_0\rangle + \sum_{m=1}^{\infty}\sum_{n=1}^{\infty}\lambda^m a_n^{(m)}(t)|\phi_n\rangle e^{-i\omega_n t} \tag{2.4}$$

Plugging this ansatz into eq. 2.3, multiplying from the left with $\langle\Psi(t)|$ and equating the terms of the same power of λ, yields a set of differential equations for the expansion coefficients $a_n^{(m)}(t)$, which can be solved iteratively for increasing order m. The solutions to these equations are significantly simplified if the calculations are carried out in the Fourier plane i.e. if the field is monochromatic or is expressed as a sum over monochromatic waves. Under the condition that $\mathbf{E}(t)$ is monochromatic, and thus can be written as the real part of $E_0e^{-i\omega t}$, plugging the wave function, expanded

to order m into eq. 2.2 yields an expansion of the polarization density in powers of the electric field amplitude,

$$\mathbf{P}^{(m)}(t) = \sum_{k=1}^{m} E_0^k \chi^{(k)}(\omega)(e^{-i\omega t} + e^{i\omega t})^k, \tag{2.5}$$

where the expansion coefficients are called the susceptibilities of order k. The linear response, expressed by the first order susceptibility $\chi^{(1)}(\omega)$, describes the dispersion and absorption of the medium. Inserting 2.5, expanded to first order, into eq. 2.1 it can be concluded that the refractive index, $n(\omega)$, can be expressed as,

$$n(\omega) = \sqrt{1 + \chi^{(1)}(\omega)} \tag{2.6}$$

The susceptibilities of order $k > 1$ describe the non-linear response of the medium and are associated with the generation of new frequencies, which are harmonics of the fundamental frequency ω.

From this treatment we can draw some conclusions about the physical properties of the harmonic light. For the perturbative approach to be valid the included terms have to converge, which implies that the intensities of the generated harmonics should rapidly decrease with order. Furthermore the intensity of an individual harmonic should depend on the intensity of the driving field to the power of the order. However, as noted in the previous section, neither of these statements are true for high-order harmonics. For HHG the intensity of the harmonics is approximately constant after the lowest orders up until an abrupt cut-off. The harmonic strength does not vary as E_0^k, but instead is, for the harmonics in the plateau region, rather independent of order. This departure from the predictions of perturbation theory indicate that the assumptions made in formulating certain aspects of the theory are invalid and calls for a different understanding of HHG.

2.3.2 The strong field regime

The current understanding of the generation of high-order harmonics is based on a model put forward in 1993 [34, 35], called the Three-step Model. As it was formulated using concepts from both classical physics and quantum mechanics, it is refereed to as semi-classical. Soon after this model was published, the insight it brought was used to describe the process in quantum mechanical terms [36]. These models provided an explanation for the lacks in the perturbative model.

The semi-classical model

The key to understanding where the perturbative model breaks down relates to the concept of tunnel ionization. Under the influence of a sufficiently strong, long-wavelength (opical) electric field there is a non-vanishing probability for an electron originally bound by an atom to tunnel through the potential barrier formed by the Coulomb potential distorted by the optical field. Thus, since tunneling is a strong field effect, the distortion of the atomic field cannot be treated as a perturbation.

The tunneling phenomenon is taken into account in the first step in the Three-step Model, as indicated in Fig. 2.6. The part of the electronic wave function that tunnels through the barrier forms a "free" wave packet, which will interact predominantly

with the strong laser field. The Three-step Model focuses on the dynamics of this continuum wave packet.

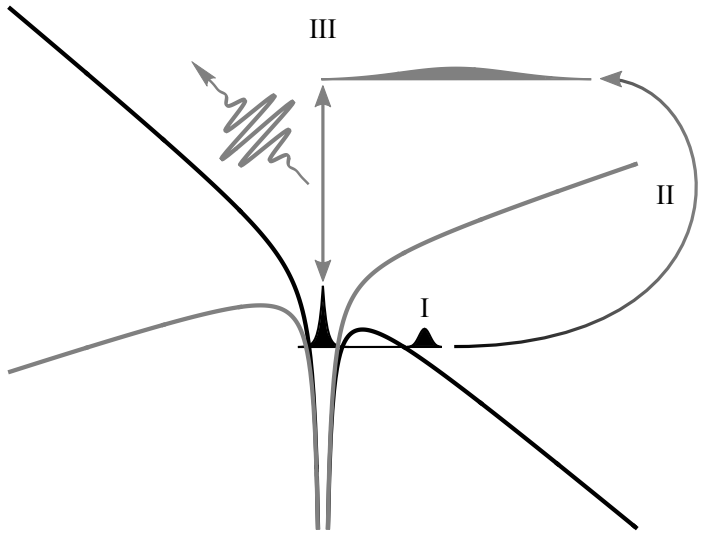

Figure 2.6: Illustration of the Three-step Model for HHG, indicating the three time ordered events of the model, tunneling (I), acceleration(II) and recombination (III).

As the continuum wave packet is formed it can be accelerated by the light field. This process is treated semi-classically in the model. The electron is modeled as a classical particle appearing at the position of the nucleus with zero velocity at time t_i, the tunneling time, with a certain probability. As its interaction with the remaining ion is neglected, its trajectory, $x(t_i, t)$, is trivially found by Newtonian mechanics,

$$x(t_i, t) = \frac{eE_0}{m\omega^2}[\sin(\omega t) - \sin(\omega t_i) - \omega(t - t_i)\cos(\omega t_i)], t > t_i \tag{2.7}$$

for a linear polarized, electric field, $E(t) = E_0 \sin(\omega t)$, where e and m are is the electron charge and mass, respectively. Some of these trajectories will cross the position of the nucleus again, as indicated by the black solid lines in Fig. 2.7, while others will acquire a drift momentum large enough for the electron to escape from the vicinity of the ion, indicated by gray dashed lines. In this semi-classical picture the trajectories that cross the zero position describe a wave packet that has been accelerated and driven back to its original position by the electromagnetic field (process labeled II in Fig. 2.6). The returning wave packet has a non-vanishing spatial overlap with the part of the wave function that is left in the atomic ground state and their interference will therefore contribute to the dipole moment in eq. 2.2.

The energy difference between the ground state and the distribution of states forming the continuum wave packet defines the beat frequencies at which the dipole moment will radiate. This is step III in the model, where the interaction between the returning wave packet and the remaining ground state results in a burst of light being emitted. The kinetic energy of the returning electron, E_{kin}, is a function of the tunneling time and the time of return, t_r, and can be calculated from eq. 2.7. The

range of photon energies emitted in the recombination process is consequently given by $E_{kin} + I_p$.

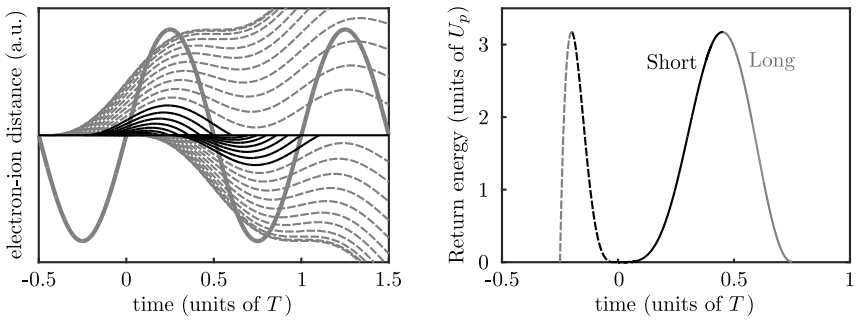

Figure 2.7: Left, classical trajectories of an electron in a electromagnetic field for different release or tunneling times. Right, kinetic energy of a returning electron as a function of tunneling (dashed lines) and return time (solid lines).

The right panel in Fig. 2.7 shows the return kinetic energies as a function of tunneling and return times. The energy is expressed in units of the ponderomotive potential, which is the average kinetic energy of a free electron driven by an oscillating electromagnetic field. The pondermotive potential depends on the intensity, I, and the frequency, ω, of the driving field as,

$$U_p = \frac{e^2 I}{2m_e \omega^2 \epsilon_0 c}. \tag{2.8}$$

The maximum kinetic energy for a returning electron is $3.17U_p$, which means that the highest photon energy in the emitted radiation is,

$$E_{max} = 3.17U_p + I_p. \tag{2.9}$$

This equation thus gives the position of the high energy cut-off. In a more elaborate analysis that takes in to account all possible electron trajectories, not just those fulfilling the initial conditions of eq. 2.7, it can be shown that the emitted radiation extends to higher photon energies than given by eq. 2.9. The cut-off energy is thus rather an estimate of where the harmonic plateau ends and the generation process becomes inefficient.

Two different classes of trajectories can be identified, labeled long and short in Fig. 2.7. For the long trajectories, the time between tunneling and return are long compared to the class of trajectories labeled short. This picture also partly explains the temporal structure of the emitted radiation. To understand how, we relate the return time to the spectral phase of the wave packet (ϕ) by interpreting the return time as a group delay,

$$t_r = \hbar \frac{\partial \phi}{\partial E} \tag{2.10}$$

The propagation of the electron wave packet in the continuum leads to a significant dispersion and the time window of return is longer than that for tunneling (see Fig. 2.7). This stretch in time leads to a chirp of the emitted radiation. The leading

edge of the wave packet which contains contributions from the short trajectories, is positively chirped ($\frac{\partial\phi}{\partial E} > 0$) while the trailing edge is negatively chirped ($\frac{\partial\phi}{\partial E} < 0$) due to the contributions from the long trajectories. From an experimental perspective this fact constitutes a potential problem. The interference between the harmonic fields with different spectral phases could potentially distort the time-structure of the pulse. Luckily, the different contributions can be experimentally selected by choosing the generation conditions, as discussed in the next section.

A quantum-mechanical model: The strong field approximation

The semi-classical model gives an intuitive picture and explains some aspects of HHG, such as the cut-off law and the intrinsically chirped generated pulses. In the long wavelength limit, the propagation of the wave packet in the continuum along the spatial coordinate defined by the polarization direction of the driving field can be rather well described classically. However, pure quantum effects such as tunneling or transversal spreading of the wave packet due to quantum diffusion have to be added ad-hoc rather than derived from first principles.

As stated, the quantum version of the three-step model was introduced by Lewenstein and co-authors in [36]. It is derived under what is known as the strong field approximation, which makes is possible to derive an analytical expression for the time-dependent wave function and the atomic dipole moment under the influence of a strong laser field.

The strong field approximation consists in neglecting the influence of the bound states, other than the ground state, on the formation and return of the wave packet, and also in neglecting the influence of the atomic potential on its continuum propagation and assuming that the ground state is not depleted. The Schrödinger equation can be written as,

$$\left(-\frac{\hbar^2}{2m}\hat{p}^2 + V(\hat{r}) + e\mathbf{E}(t)\cdot\hat{r}\right)|\Psi(t)\rangle = i\hbar\frac{\partial}{\partial t}|\Psi(t)\rangle, \tag{2.11}$$

which is equivalent to eq. 2.3. Here, however, the full Hamiltonian is explicitly written in order to point out some properties of the SFA anzats. Following the derivation in [37], the continuum part of the wave function is represented by Volkov states,

$$\langle\mathbf{r}|\mathbf{p}+e\mathbf{A}(t),t_0,t\rangle = \frac{1}{\sqrt{2\pi}}e^{i\frac{1}{\hbar}[\mathbf{p}+e\mathbf{A}(t)]\cdot\mathbf{r}}e^{-i\frac{1}{\hbar}\int_{t_0}^{t}d\tau\frac{\hbar^2}{2m}[\mathbf{p}+e\mathbf{A}(\tau)]^2+I_p}. \tag{2.12}$$

These are the exact solutions to the time-dependent Schrödinger equation if the atomic potential were not present, and are simply plane waves where the instantaneous momentum is modulated by the vector potential $\mathbf{A}(t)$ due to the presence of the external field. The vector potential is, in the gauge chosen in eq. 2.11, the time integral over the electromagnetic field,

$$\mathbf{A}(t) = -\int_{-\infty}^{t} d\tau\ \mathbf{E}(\tau). \tag{2.13}$$

Since all other bound states but the ground state are assumed not to play a role for the continuum dynamics responsible for HHG, and since the ground state population

is assumed to be approximately constant, the full SFA wave function can be written as,

$$|\Psi(t)\rangle = |\phi_0\rangle + \int d\mathbf{p}\ a_{\mathbf{p}}(t)|\mathbf{p} + e\mathbf{A}(t)\rangle e^{-i\frac{1}{\hbar}\int_{t_0}^{t} d\tau \frac{\hbar^2}{2m}[\mathbf{p}+e\mathbf{A}(\tau)]^2 + I_p}, \tag{2.14}$$

i.e. as a superposition of the ground-state and a continuum wave packet. Plugging the ansatz into eq. 2.11 and multiplying from the left by $\langle\Psi(t)|$ yields a set of integral equations for the expansion coefficients $a_{\mathbf{p}}(t)$. Here another approximation comes into play. Since the states $|\mathbf{p}+e\mathbf{A}(t)\rangle$ are not eigenstates of the full Hamiltonian they will be mixed by the presence of the atomic potential. In other words there is a finite probability at each point in time for the plane wave $|\mathbf{p}+e\mathbf{A}(t)\rangle$ to scatter off the ion to another plane wave $|\mathbf{p}'+e\mathbf{A}(t)\rangle$. In a first order approximation the term representing scattering can be left out, giving the following equation for the expansion coefficients,

$$a_{\mathbf{p}}(t) = \int_{-\infty}^{t} dt'\ \mathbf{E}(t)\cdot\langle\mathbf{p}+\mathbf{A}(t)|\hat{r}|\phi_0\rangle e^{-i\frac{1}{\hbar}\int_{t'}^{t} d\tau \frac{\hbar^2}{2m}[\mathbf{p}+e\mathbf{A}(\tau)]^2 + I_p} \tag{2.15}$$

Having found the wave function, the time-dependent dipole moment can be calculated. In doing so we neglect the term representing radiative transitions between the Volkov states. This should not have a big influence on the result since the continuum population is assumed to be small. The final approximate expression for the time-dependent dipole moment under the SFA approximation can accordingly be written as,

$$\begin{aligned}\langle\Psi(t)|\hat{r}|\Psi(t)\rangle \approx \frac{e}{i\hbar}\int d\mathbf{p}\int_{-\infty}^{t} dt'\ \mathbf{E}(t')\cdot\langle\mathbf{p}+\mathbf{A}(t')|\hat{r}|\phi_0\rangle \\ e^{-i\frac{1}{\hbar}\int_{t'}^{t} d\tau \frac{\hbar^2}{2m}[\mathbf{p}+e\mathbf{A}(\tau)]^2 + I_p}\langle\phi_0|\hat{r}|\mathbf{p}+\mathbf{A}(t)\rangle + c.c\end{aligned} \tag{2.16}$$

Here we can recognize the three steps from the semi-classical theory. The first factor on the upper row represents tunneling at time t'. The electron then propagates in the continuum acquiring a phase given by the exponential factor, to a time t when it recombines with the ion. The recombination is represented by the last factor in the second row.

This interpretation of eq. 2.16 has a grate deal in common with Feynman's path integral formulation of quantum mechanics [38]. The exponential factor acts as a propagator, and the phase accumulated can be identified as the classical action for the path defined by t, t' and $\mathbf{p}$, divided by $\hbar$. Fourier transforming the time-dependent dipole moment reveals the spectral content of the emitted radiation.

The resulting triple integral can be evaluated in an approximate fashion by only considering the dominating contributions, which appears when the phase of the propagator is stationary with respect to t, t' and $\mathbf{p}$. This approach to evaluating integrals with rapidly oscillating integrands is known as the saddle point approximation. In this context the method also has a physical meaning. In classical mechanics, the path of a particle is defined by a stationary action. Using the saddle point approximation is thus equivalent to excluding all quantum paths or trajectories but the classically allowed ones. Not surprisingly, carrying out this analysis, one then recovers many of the results from the semi-classical model. For example, over a large spectral range

that corresponds to the plateau region, the Fourier components are the sum of two contributions, given by two different branches of the stationary action. These two classes of quantum trajectories are similar to the classical short and long trajectories and also give rise to the emission of *two* chirped attosecond pulses per half cycle [39].

There are several methods for including the neglected contributions or correcting for some of the approximations made in this derivation. The effects of ground state depletion [36] and the scattering of the Volkov states in the atomic potential can be included. Further corrections to the model can be made in order to account for the effect that the Coulomb potential has on the propagation of the wave packet [40]. To get a good qualitative agreement with experiments, however, the time-dependent Schrödinger equation has to be solved numerically.

Limitations of HHG

The high-order harmonic cut-off law (eq. 2.9) stipulates an upper limit to what photon energies can be generated from an HHG source. Pushing this limit as high as possible is of course desirable as it increases the applicability of the source.

Since the ponderomotive potential scales linearly with the intensity of the driving field (see eq. 2.8), a high intensity generally generates a high cut-off. However, the generation of high-order harmonics is closely linked to field ionization. In a sense they are competing processes. Thus the conversion efficiency drops if a large fraction of the target atoms becomes ionized by the driving field [41]. For a given laser pulse length there is thus an upper limit for the peak intensity of the pulse, a saturation intensity, below which the frequency conversion can be considered efficient. Higher intensities can be used with target atoms that has a higher ionization potential, since these have a smaller probability to be field ionized [42]. The price paid then, however, is an overall lower conversion efficiency. On the other hand, as we shall see later on, a small degree of ionization of the generation medium (on the order of a few percent) is often a prerequisite for efficient harmonic generation.

The ponderomotive potential scales quadratically with the driving field wavelength. In addition to generating a more dense spectrum, using a long wavelength driving pulse also generates a high cut-off frequency. Making use of this insight, it has been experimentally proven that HHG can be pushed to generate photons with keV energy by using MIR laser drivers [43]. This is accomplished, however, at the expense of a dramatically decreasing conversion efficiency. Theoretical and experimental studies suggest that the efficiency scales with wavelength as unfavorably as λ^{-6} [44, 45].

2.4 Macroscopic ensemble effects - Phase matching

Having discussed how an atom responds to a strong optical field and its ability to act as a radiator at a harmonic frequency, we now consider the collective response of a large ensemble of coherently radiating atoms. From this perspective the electromagnetic field interacts with an optically homogeneous medium with macroscopic dimensions and the response is described by the polarization density. However, solving the full problem of the (non-linear) wave equation coupled to the Schrödinger equation in time and space is a tremendous computational task. Here we thus treat the problem on a high-level of approximation and rely on qualitative arguments rather than on a rigid mathematical derivation.

Phase-matching of monochromatic plane waves in a static medium

To introduce the concept of phase-matching we start with an unrealistic but simple case, where the fundamental field is described as a plane monochromatic wave. We can then assume slow spatio-temporal modulations of the complex amplitude with respect to the cycle time and wavelength and correct the model accordingly. The polarization density at the harmonic frequency, $q\omega$, includes two contributions. The induced dipole moment of an individual atom is not only driven by the fundamental field but also by the presence of the generated harmonic. The two contributions can however, be assumed to be independent. Therefore the polarization density can be written as a sum of the non-linear polarization density and a linear response to the harmonic electric fields, described by the first order susceptibility,

$$P^q = P^q_{NL} + \chi^{(1)}(q\omega)E_q, \tag{2.17}$$

This is a good approximation as long as the harmonic field itself is not strong enough to induce a non-linear response in the generation medium, which is generally the case. The interplay between these two contributions gives rise to the concept of phase-matching. Since we have decoupled the linear- from the non-linear polarization density we can also treat each harmonic frequency independently. Furthermore, since the density of the medium is low, we can assume that the overall conversion to harmonic light is small, meaning that the fundamental field itself is unaffected by the non-linear polarization density it induces.

Under these simplifying conditions, we can simply write the non-linear polarization density at the harmonic frequency in a complex representation as,

$$P^q_{NL}(r,z,t) = N\mathcal{A}_q(E_0)e^{i[-q\omega t+\phi_q^{dip}(E_0)+\phi_q(z)]}, \tag{2.18}$$

where N is the number density of atoms. $\mathcal{A}^q(E_0)$ is an amplitude and $\phi^q_{dip}(E_0)$, a phase which both depend on the single atom response to a fundamental field with an amplitude of E_0. The spatial phase variation, $\phi_q(z)$, along the coordinate that defines the propagation axis of the fundamental field is, owing to the coherence of all the oscillating dipole moments, locked to the spatial phase of the fundamental field. This can be understood by considering that the driving field is shifted by ϕ_0. For a monochromatic wave this is equivalent to a time shift of $\Delta t = -\phi_0\omega^{-1}$. Since the non-linear dipole moment only depends on the driving field, the same transformation should be made in eq. 2.18, $t \to t + \Delta t$, which establishes the phase relation $\phi_q(z) = q\phi_0(z)$. Therefore, under the plane wave approximation, $\phi_q(z) = qk_0z$, where $k_0 = \omega n(\omega)c_0^{-1}$.

Inserted into the wave equation it becomes apparent that the non-linear polarization density acts as a source term that generates a new plane wave with a frequency $q\omega$ and a field strength proportional to $iq^2\omega^2P_{NL}(r,z,t)$. The linear response of the medium at this frequency causes the generated wave to propagate with a wave vector $k_q = q\omega n(q\omega)c_0^{-1}$. The total field at a point z is thus proportional to the coherent sum over the fields that have their source point at z' and have propagated a distance $z - z'$. Since the medium from a macroscopic point of view can be considered a continuum the sum turns into an integral. Given that the fundamental laser beam enters the medium at $z = 0$ and that the density is approximately constant, the complex harmonic field can be written as,

$$E_q(r,z,t) \propto iN\mathcal{A}_q e^{i[-q\omega t+\phi_q^{dip}]} \int_0^z dz' \; e^{iqk_0z'+k_q(z-z')}, \tag{2.19}$$

where the explicit E_0 dependence is implied. Carrying out the integration and introducing the wavenumber mismatch, $\Delta k_q = k_q - qk_0$, the resulting field can be written as,

$$E_q(r,z,t) \propto iN\mathcal{A}_q z \frac{\sin(\Delta k_q z/2)}{\Delta k_q z/2} e^{i[\frac{z}{2}(k_q+qk_0)+\phi_q^{dip}-q\omega t]} \tag{2.20}$$

The wave vector mismatch expresses the fact that the non-linear and linear polarization fields propagate with different phase velocities. As is evident from eq. 2.20 this can have large consequences for the conversion efficiency. Figure 2.8 illustrates how the real harmonic field, $\mathcal{E}(z)$, build up along the propagation axis in two different cases.

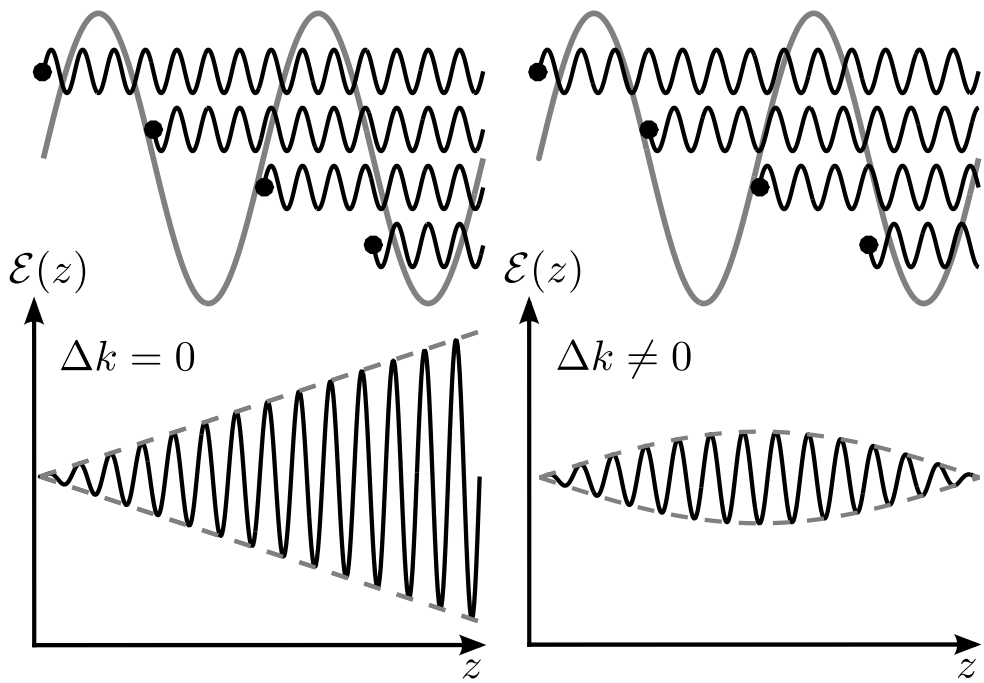

Figure 2.8: Illustration of the effect of wave vector mismatch. To the left, no mismatch, the field envelope grows linearly with z. To the right, a mismatch, the field envelope is sinusoidal in z.

In the fully phase-matched case, i.e. when $\Delta k_q = 0$, the factor $\mathrm{sinc}(\Delta k_q z/2)$ in eq. 2.20 is 1, and therefore the amplitude of the field grows linearly with z. The field generated from an individual atom, symbolized by black dots in the figure, is in phase with the dressing field at the harmonic frequency, which optimizes the conversion efficiency.

On the left side in the figure, the wavelength of the harmonic field is slightly longer, or equivalently, the wave vector is smaller. The fundamental field and the non-linear

response are, however unchanged, which results in a situation where the emitted light is slightly out of phase with the dressing harmonic field. This in general reduces the total conversion efficiency, and sets an upper limit on the length of the generation medium. If the medium were to end where the axis ends in the figure, none of the available fundamental laser energy would be converted into harmonic light.

A more convenient way to describe the wave vector mismatch, when relating it to the length of the non-linear medium, is to use the coherence length, L_c^q,

$$L_c^q = \frac{\pi}{|\Delta k_q|}. \tag{2.21}$$

The coherence length is the distance over which the traveling harmonic field dephases by π relative to the non-linear polarization field under non phase-matched generation conditions. As a consequence, to have as efficient harmonic generation as possible, the medium length should be about half the coherence length.

Re-absorption

The model introduced above for HHG on a single atom level, describes and explains how photons with an energy greater than the ionization potential of the target atom are produced. On a macroscopic level this also means that the generated light will photoionize the generation medium along its path. The attenuation of the harmonic field due to photoabsorption can be included in our current model by allowing the wave vector, k_q, to have an an imaginary part, $i\kappa_q$. This follows from the fact that an optically absorbing medium has a complex susceptibility. To a good degree of approximation $\kappa_q = \sigma(\omega_q)N/2$, where $\sigma(\omega_q)$ is the photoabsorption cross section at the q^{th} harmonic frequency. Carrying out the integration in eq. 2.19 with the modified wave vector gives the following expression for the harmonic intensity as a function of the longitudinal coordinate z,

$$I_q(z) \propto N^2 \mathcal{A}_q^2 e^{-\kappa_q z} \frac{\cosh(\kappa_q z) - \cos(\Delta k_q z)}{\Delta k_q^2 + \kappa_q^2}. \tag{2.22}$$

Analogous to the coherence length we can define an absorption length,

$$L_{abs}^q = \frac{1}{2\kappa_q}. \tag{2.23}$$

Figure 2.9 shows how the longitudinal build-up of the harmonic intensity is affected by re-absorption, under different phase-matching conditions. To estimate the impact, the absorption limited curves, in black, can be compared to the quadratic growth (linear for the electric field) of phase-matched generation in a non-absorbing medium, in blue.

Re-absorption of the harmonic light limits the effective length over which the field is built up. Therefore, the non-linear frequency conversion eventually saturates if the generation medium is extended to more than a few times the absorption length [46].

2.4.1 Controlling phase-matching

An important question that has generated a great deal of interest since the discovery of HHG is how the collective response of a gaseous medium can be controlled or ma-

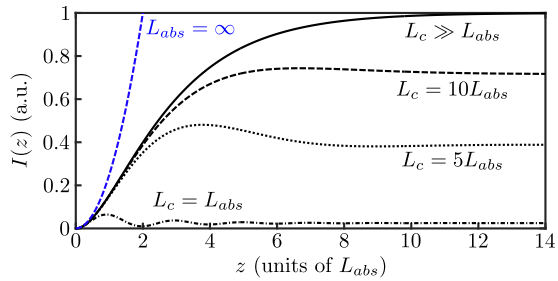

Figure 2.9: Intensity of the harmonic field as a function of the longitudinal coordinate in units of the absorption length, under different phase-matching conditions. The blue curve displays the quadratic growth of absorption free phase-matched harmonic generation. The figure is adapted for [46].

nipulated in such a way that the photon flux for a given experiment can be optimized (see e.g. [47–50]).

The simple model presented above does not provide any tools for this type of optimization control. The wave vector mismatch is given by the target atom and the density of the generation medium. Reducing the mismatch can only be achieved by reducing the gas density, but this also reduces the number of atoms that contribute to the frequency conversion. The key to manipulating the generation conditions to favor a high level of conversion is to balance the wave vector mismatch by utilizing dynamical and geometrical effects that are not accounted for in the purely static, plane-wave model.

Ionization

Ionization of the generation medium induced by the strong fundamental field is an unavoidable secondary consequence of the production of high-order harmonics. If the level of ionization is moderate at the time and location where the driving pulse is maximum, the presence of free electrons can help to locally balance the wave vector mismatch and dramatically increase the total conversion efficiency.

For a medium with only neutral atoms $k_q < qk_0$, since the susceptibility (and the refractive index) generally decreases monotonically with frequency when $\hbar\omega > I_p$. For a low density plasma, where there is an abundance of free electrons, the dispersion relation is approximately,

$$k(\omega) \approx \frac{\omega}{c_0} - \frac{N_e e^2}{2m_e \epsilon_0 c_0 \omega^2}, \tag{2.24}$$

where N_e is the free electron number density. In an ionized gas the local wave vector mismatch is consequently altered by a *positive* correction,

$$\Delta k_q^e = \frac{N_e(r,z,t)e^2}{2m_e \epsilon_0 c_0 q^2 \omega^2}(q^2 - 1) \tag{2.25}$$

The local free electron density can be calculated using the general solution to a coupled rate equation,

$$N_e(r,z,t) = N\left(1 - e^{-\int_\infty^t d\tau\ \Gamma[\mathcal{E}_0(r,z,\tau)]}\right) \tag{2.26}$$

where Γ is the local ionization rate and N is the initial number density of neutral atoms. The ionization rates, which depend on the instantaneous electric field, can in turn be estimated from calculations based on, for example, ADK theory [51], if the driving laser pulse is known.

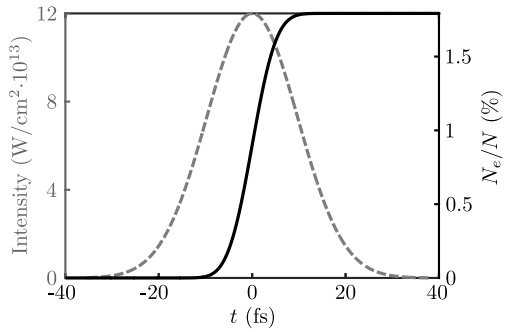

Figure 2.10: Fractional density of free electrons in argon gas, induced by strong field ionization, as a function of time. The laser pulse, whose intensity profile is mapped out by the gray line, has a duration (FWHM) of 23 fs, a peak intensity of $1.2{\cdot}10^{14}$ W/cm^2 and a carrier frequency corresponding to a vacuum wavelength of 800 nm.

Figure 2.10 illustrates how the fractional free electron density varies in time when argon gas is ionized by a laser pulse with a Gaussian time envelope. The rates used for the calculation are tabulated cycle averaged rates extracted from numerically solving the TDSE [41]. The figure does thus not show the true sub-cycle behavior of strong field ionization, which is, however, not important in this context. A potentially more important aspect that is left out in this simplified calculation is the spatial and temporal distortion of the pulse caused by rapidly changing dispersion properties and strong dispersion gradients in the generation medium [41]. The most prominent sign of a moderate plasma formation is a blue shift of the carrier frequency of the pulse, due to the temporal change in the refractive index of the medium, and a "de-focusing" of the laser beam, due to a plasma induced transversal gradient in the refractive index.

To a large extent, the wave vector balance can be controlled by varying the pulse energy, duration and focal geometry. Good phase matching conditions can normally be reached by an ionization degree of a few percent, which also means that the generation is far from saturating due to depletion of the atomic ground state.

Focusing geometry

With a low degree of ionization, where the plasma reshaping of the fundamental pulse is negligible, the phase-matching conditions should again be rather independent of medium density, since the dispersion contributions from both neutral atoms and free electrons scale almost linearly with the initial pressure. From an experimental point of view it is clear, however, that phase-matched harmonic generation can normally only be achieved within a limited pressure interval [52], which is a consequence of that the laser energy has to be confined to a small volume. For a freely propagating beam, close to the focus the phase gradient along the axis is not simply k_0, but rather k_0 plus a contribution that depends on the focal geometry. The most widely used mathematical

model to describe a laser beam is the Gaussian beam, for which geometrical phase shift is,

$$\phi_g(z) = -\arctan\left(\frac{z}{z_0}\right), \tag{2.27}$$

given that the focus i located at $z = 0$. z_0 is a parameter, called the Rayleigh length, that depends on the initial beam diameter and the focal length. In this case the on-axis spatial phase of the non-linear dipole moment is thus $qk_0z + q\phi_g(z)$, which, put into eq. 2.19, clearly changes the phase-matching conditions. In a loose focusing geometry, where the medium length is much smaller than z_0, it is motivated to Taylor expand $\phi_g(z)$ around the focal position to first order. In that case one finds that the geometrical phase shift gives rise to a correction to the wave vector mismatch which amounts to,

$$\Delta k_q^g = -\frac{q}{z_0} \tag{2.28}$$

This contribution is pressure *independent* and therefore the total phase mismatch does not necessarily scale with the medium density. Clearly, extremely loose focusing, i.e. with the focal length very long or the beam diameter very small, will lead to a situation where the effect of the geometrical phase shift is negligible.

The phase of the non-linear polarization density

In a focused beam the on-axis intensity will of-course also vary with position. For a Gaussian beam this variation is Lorenzian,

$$I(z) = \frac{I_0}{1 + (z/z_0)^2}, \tag{2.29}$$

where I_0 is the intensity at the focus position. From a phase-matching perspective this is important since it means that the phase factor ϕ_{dip} cannot be considered a constant, in space or time.

The phase of the non-linear dipole moment has its origin in the exponential propagation factor in the SFA integral expression given in eq. 2.16. The phase imprinted on the electronic wave packet during propagation will be reflected in the radiation emitted. A saddle-point analysis of the Fourier transformed dipole moment shows that the phase corresponding to a given quasi-classical trajectory varies predominately linearly with the intensity of the driving field [53]. Consequently, the two contributions to the Fourier component of the dipole moment at a frequency $q\omega$ have a phase that can be written approximately as,

$$\phi_{dip}^{S,L}(q\omega) = \beta_q^{S,L} + \alpha_q^{S,L} I(z), \tag{2.30}$$

where α and β are coefficients that vary smoothly with frequency and the indexes S and L denotes the long- and short trajectories, respectively. Since the two contributions have comparable amplitudes, their interference causes the total spectral phase to vary rapidly and seemingly randomly in the plateau region. The long trajectories have, however, a much longer excursion time than the short, which means that the phase accumulated along these trajectories is more sensitive to a change of intensity. In other

words $\alpha_q^S < \alpha_q^L$. This fact can be utilized by tailoring the macroscopic generation conditions to select the contribution from one group of trajectories, and thereby to smoothen the spectral phase [54]. Effectively this means selecting one of the two chirped pulses emitted every half cycle. Generally, it is easier to optimize the short trajectory contribution due to the smaller phase gradient along the axis. The phase gradient contribution due to the intensity sensitive dipole phase, Δk^{dip}, is positive before the focus position ($\frac{\partial I}{\partial z} > 0$) and negative after ($\frac{\partial I}{\partial z} < 0$). Therefore it can be balanced locally with the negative geometrical wave vector mismatch, after the focus.

Due to the transversal intensity gradient across the focused beam the short and long trajectory contributions also have different behaviors in the far-field. The generated wave front is curved by the transversal dipole phase variation. This curvature is much more pronounced for the long trajectory contribution, which therefore produces a more divergent beam in the far field. The spectral phase and temporal structure of the harmonic field can consequently also be filtered by introducing an aperture somewhere in the far-field as seen from the generation point [55].

Summary

In summary, the efficiency and spectral characteristics of a HHG source depend heavily on how well the phase-matching conditions can be tailored such that the total wave vector mismatch over a substantial volume and during a majority of the driving pulse duration, is minimized. To achieve this the four contributions to the total wave vector mismatch have to be balanced against each-other such that,

$$\Delta k_q^{tot} = \Delta k_q^n + \Delta k_q^e + \Delta k_q^g + \Delta k_q^{dip} \approx 0. \tag{2.31}$$

Furthermore, the available parameter space in terms of, medium density and length, focal conditions, peak intensity and pulse duration, is limited by re-absorption and strong-field ionization.

2.5 High-order harmonics and attosecond pulses

At the atomic level, strong field non-linear optics are governed by the sub-cycle dynamics of electronic continuum wave packets. At the same time the propagation of the generated electromagnetic field is most conveniently treated in the spectral domain, and is therefore described as a sum of or integral over monochromatic waves. Furthermore, since no photodetector has a sufficiently fast response to resolve attosecond (or even femtosecond) time structures, characterization of attosecond pulses has to be carried out in the spectral domain. This, sometimes confusing, dual perspectives calls for a brief discussion.

At the atomic level, a short burst of light is emitted during an interval that corresponds to the duration of the returning electronic wave packet. This event repeats itself once every half cycle of the driving field, with the only difference being that the dipole moment changes sign at each consecutive event. In the time domain it is easily realized that this generates a train of pulses separated by half a cycle ($T/2$), with a π phase-shift between consecutive pulses. The Fourier transform of the pulse train can be written as a sum over the contributions from each cycle n,

$$E(\Omega) = \sum_n \left[E_I(\Omega) e^{i\Omega nT} - E_I(\Omega) e^{i\Omega(n+\frac{1}{2})T} \right], \tag{2.32}$$

where $E_I(\Omega)$ is the Fourier transform of the individual (assumed identical) pulses and T is the duration of one cycle of the driving field. The time-shift between the pulses is accounted for by the phase factors given by the Fourier shift theorem. Using the fact that $T = 2\pi\omega^{-1}$ and summing eq. 2.32 from $n = -N$ to N, we obtain,

$$E(\Omega) = E_I(\Omega) \frac{\sin\left[(2N+1)\pi\frac{\Omega}{\omega}\right]}{\sin\left(\pi\frac{\Omega}{\omega}\right)} (1 - e^{i\pi\frac{\Omega}{\omega}}) \tag{2.33}$$

The middle factor of this equation is similar to the expression describing a diffraction pattern from a grating with N rulings. This factor peaks when the numerator tends to zero, i.e when Ω/ω approaches an integer value. The last factor is, however, zero when Ω/ω takes an even integer value, and thus cancels out the peaks corresponding to even integers. Figure 2.11 illustrates how $|E(\Omega)|^2$ changes with the number of contributing sub-cycles. The more pulses that are included in the sum, the more the spectral power becomes concentrated in sharp peaks at odd order multiples of ω.

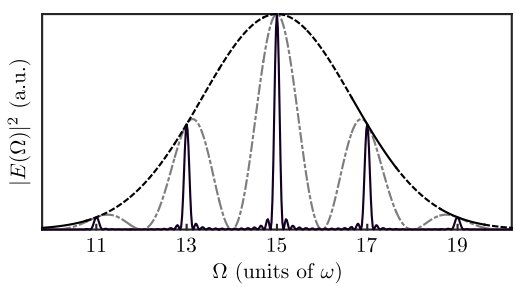

Figure 2.11: Illustration of the effect of multi-pulse interference. The black dashed line shows $E_I(\Omega)$, the gray dash-dotted line the case when two pulses from the same cycle are added ($N = 0$) and the black solid line when 14 pulses from 7 consecutive cycles are added ($N = 3$).

In the limit, $N \to \infty$, the middle factor tends to a series of Dirac delta functions and the spectral representation of the electric field becomes,

$$E(\Omega) = E_I(\Omega) \sum_q \delta(\Omega - q\omega)(1 - e^{i\pi q}) = 2E_I(\Omega) \sum_q \delta[\Omega - (2q+1)\omega], \tag{2.34}$$

This shows that only frequencies that are odd order harmonics of ω survive the pulse to pulse interference.

The fact that a broad bandwidth of frequencies can be generated simultaneously is a prerequisite for short pulse production. Since the time and frequency representation of a light pulse are linked by a Fourier transform the frequency bandwidth ($\Delta\nu$) and pulse duration ($\Delta\tau$), in terms of FWHM, are subject to the time-bandwidth product condition, $\Delta\nu\Delta\tau \geqslant 0.44$. A second condition is a well defined spectral phase, i.e. a fixed phase relation between the frequency components, or coherence. Equality in the time-bandwidth product condition holds for a Gaussian shaped spectrum with a linear spectral phase.

Figure 2.12 illustrates the frequency to time mapping in the case of harmonic generation as well as the role of the spectral phase.

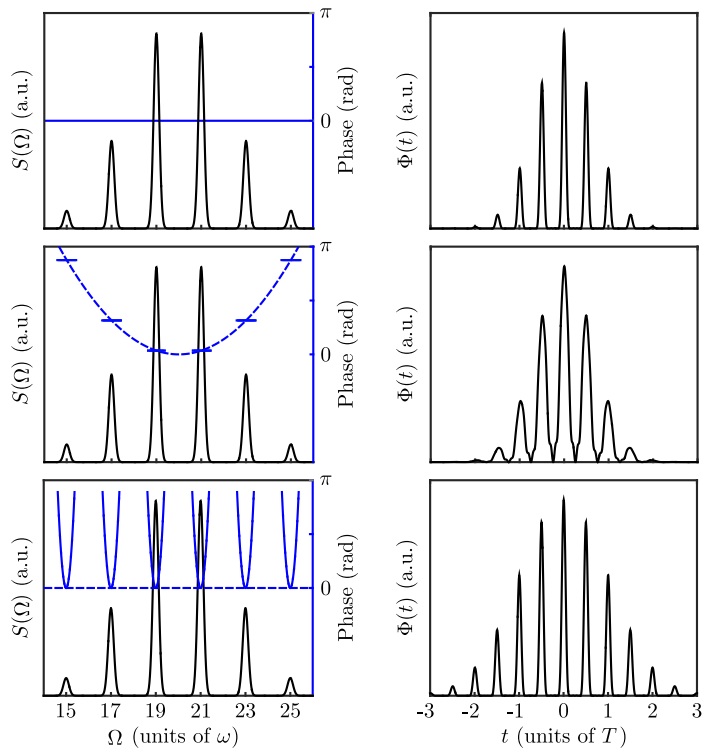

Figure 2.12: Illustration of the spectral- to time domain mapping of harmonics.

The left column shows three identical spectra, in terms of the spectral power density, $S(\Omega)$, but with different spectral phases. $S(\Omega)$ corresponds to what would be measured in an experiment such as the one illustrated in Fig. 2.1 using a laser pulse with a carrier angular frequency of ω. The right column shows the corresponding time representation in terms of the time dependent flux, $\Phi(t)$, where time is expressed in units of T. The 2ω periodicity of the spectra translates into a train of pulses that are spaced by one half cycle of the fundamental field.

In the upper row where the spectral phase is linear (flat) across the spectrum, the duration of the individual pulses are Fourier transform limited, and just inversely proportional to the bandwidth of the full spectrum. Furthermore, the duration of the pulse train is inversely proportional to the bandwidth of the individual harmonics. Moreover, an indication, although not proof, of an isolated pulse is the presence of a spectrum without the modulations due to the harmonic lines.

The central row shows an example where the phase relation between the harmonics is quadratic (dashed line), while the phase is flat across the spectral width of each individual harmonic. As a consequence the pulses in the train are chirped, i.e. their carrier frequency varies linearly in time, and are therefore stretched. The frequency content in each pulse is however the same, if they were to be isolated. Also, since

the phase is linear across the individual harmonic line, the envelope of the pulse train remains unchanged compared to that in the top row. This is an important example since, as described earlier, the pulses generated from HHG are intrinsically chirped, due to the characteristics of the laser-matter interaction. It is therefore often necessary to implement post generation compression schemes in order to retrieve the shortest possible pulses on the experimental target. The conventional way to do this is to let the radiation pass through thin foils of some dispersive material that will imprint a spectral phase with a variation opposite to the initial one [56].

In the lower row we illustrate the situation where the phase varies in a non-linear fashion across the harmonic lines. As can be seen from the corresponding time representation only the pulse envelope of the pulse train is affected while the duration of the individual pulse remains the same. Furthermore, while the carrier frequency of each pulse is constant, the frequency content now varies from pulse to pulse.

For a short fundamental pulse, the characteristics (phase and amplitude) of the half-cycle change rapidly. This leads to a situation where each pulse in the XUV pulse train is generated under different conditions and therefore has a varying spectral content. This effect is easier to analyze if we consider that each line in the harmonic spectrum represents a pulse with a duration comparable to that of the fundamental pulse. The temporal phase of these pulses can be estimated by inserting the time varying intensity of the fundamental pulse into eq. 2.30, which gives the phase of the non-linear dipole moment as a function of intensity. Around the peak of the fundamental pulse the temporal intensity profile will be approximately quadratic. As a consequence the harmonic pulses are generated with a chirp [57, 58]. The chirp rate will depend on the harmonic order (through the α coefficients), which means that,in addition to stretching the pulse train, this effect also results in a non-equidistant time spacing between the attosecond pulses.

A driving pulse with an initial chirp or a complicated temporal phase will also generate harmonic pulses with a non-linear spectral phase and consequently an ATP with a time varying carrier [59]. As already pointed out, ionization driven by the generation pulse will generally up-shift its carrier frequency, due to a close to linear time variation of the dispersion. This effect also blue-shifts the harmonic light. At the leading and trailing edges of the pulse, the dispersion change is not linear (see Fig. 2.10). As a consequence the spectrum of the driving pulse is broadened and the harmonic pulses are generated with a time varying chirp rate [60].

Chirped harmonic pulses will result in ATPs that are longer than indicated by the supported bandwidth of the harmonic lines in the power spectrum. This is the reason why a continuous harmonic spectrum is not a guarantee for a single isolated harmonic pulse. It is easy to imagine a situation where each attosecond pulse is sufficiently frequency shifted to smear out the harmonic spectral structure.

Of course the chirp originating from the sub-cycle dynamics, often called the atto-chirp, and the chirp of the harmonic pulses, which comes from the cycle to cycle variation, in reality are both present simultaneously. In Fig. 2.12 the effects have been separated for pedagogic purposes.

Attosecond pulse walk-off

The spectral phase and time-structure of an ATP is not only a product of the single atom response, but also depends on propagation effects [61]. Using the simple static

on-axis 1D-model introduced earlier in eq. 2.18, the phase of the q^{th} harmonic due to propagation through the generation medium can be written as,

$$\phi_q(L) = (qk_1 + k_q)\frac{L}{2} - \arctan\left(\frac{\tan(\Delta k_q \frac{L}{2})}{\tanh(\kappa_q \frac{L}{2})}\right) + \arctan\left(\frac{\Delta k_q}{\kappa_q}\right), \tag{2.35}$$

where L is the length of the harmonic medium. In Paper **IV** we used this model to understand how the relative phase between the fundamental and the harmonic fields changes as a function of the pressure in the harmonic generation gas cell. Previous work has also studied the phase locking between the harmonics and the fundamental in detail, but then focused instead on the atomic response [62–64].

At the output of the generation medium the accumulated phase difference is $\Delta\phi_q = \phi_q(L) - qk_1L$, which put into eq. 2.35 yields,

$$\Delta\phi_q = \Delta k_q \frac{L}{2} - \arctan\left(\frac{\tan(\Delta k_q \frac{L}{2})}{\tanh(\kappa_q \frac{L}{2})}\right) + \arctan\left(\frac{\Delta k_q}{\kappa_q}\right). \tag{2.36}$$

When there is no absorption ($\kappa_q = 0$), the de-phasing between the harmonic- and fundamental field is just the average accumulated phase mismatch between linear- and non-linear polarization densities. Absorption shortens the effective build-up length and therefore consequently limits the accumulation of phase mismatch.

Using the RABBITT method, implemented with an actively stabilized interferometer, we studied the quantity $\Delta\phi_{q+1} - \Delta\phi_{q-1}$ for a set of harmonics generated in argon gas, while changing the amount of gas ejected into the cell at each laser shot. Combining a phase measurement with a measurement of the spectral amplitude allows for a reconstruction of the average pulse in the pulse train. Figure 2.13 shows reconstructed attosecond pulses for three different pressures, together with the absolute value of the fundamental field. Our method only allows us to reference one pulse train to the next in terms of timing. The group delay of the pulses with respect to the sub-cycle of the fundamental is estimated using eq. 2.30 with coefficients extracted from SFA calculations and the intensity using the high-order harmonic cut-off law (eq. 2.9).

The experiment confirms that the timing of the attosecond pulses with respect to the sub-cycle of the fundamental field, depends on the phase-matching conditions, since changing the generation pressure should not alter the single atomic dipole moment. This result can be understood by rewriting the measured quantity as a finite difference approximation,

$$\frac{\Delta\phi_{q+1} - \Delta\phi_{q-1}}{2\omega} \approx \frac{\partial\phi_\Omega}{\partial\Omega} - \frac{\phi_1}{\omega}, \tag{2.37}$$

where ϕ_Ω is the spectral phase at the harmonic frequency Ω, and ϕ_1 is the phase of the fundamental. The shift of the ATP is a consequence of altered dispersion conditions in the generation medium, which changes the group delay of the ATP *and* phase delay of the fundamental. It is thus a matter of, in common non-linear optics terminology, a sub-cycle temporal walk-off of the ATP.

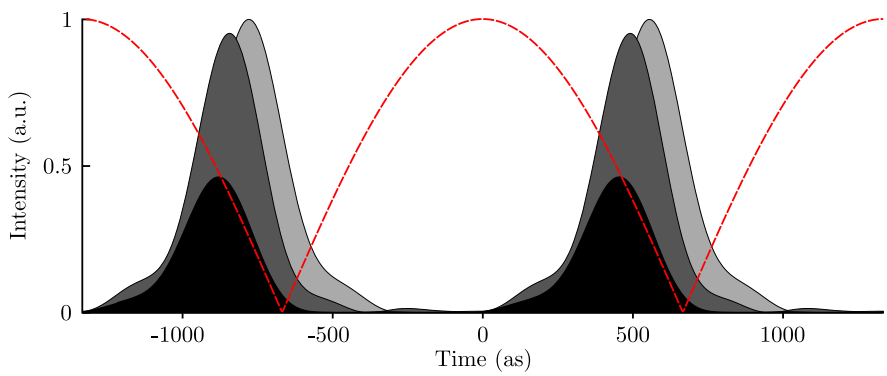

Figure 2.13: Reconstructed attosecond pulses generated in argon gas at different pressures. The background pressure in the vacuum chamber where the gas was injected is used as an indicator of the pressure in the generation cell. The background pressure was 2.5×10^{-3} mbar when the light gray pulse was recorded, 3.5×10^{-3} mbar for the dark grey pulse and 4.5×10^{-3} mbar for the black pulse. The red curve indicates the absolute value of the fundamental field amplitude, with an estimated phase.

Chapter 3

Photoelectron interferometry

Photoelectron interferometry is an experimental method for characterizing electronic wave packets that have been created via a coherent excitation of continuum states. The interferometric signal carries a signature of the electronic structure and dynamics involved in the subsequent ejection of one or several electrons as well as of the time structure of the ionizing electromagnetic radiation. The method can also be considered as an extension of photoelectron spectroscopy, which utilizes the fact that photoionization occurs by absorption of a coherent frequency comb of XUV light in the presence of an intrinsically synchronized low frequency light field.

3.1 Photoelectron spectroscopy

When the photon energy of XUV radiation exceeds the ionization energy of an atom, the interaction between them leads to photo ionization. In this thesis the majority of the work has been carried out using angular integrating photoelectron spectrometers (see Section 3.3). Applying such an instrument to study the outcome of a photoionization event driven by a XUV pulse amounts to mapping out the probability densities of continuum energy eigenstates at a time after the interaction is over [65]. More specifically, the experimental signal, which is a function of the kinetic energy of the detected electrons, E_{kin}, is

$$S(E_{kin}) \propto \sum_{l,m} |c_{\epsilon,l,m}|^2, \tag{3.1}$$

where $c_{\epsilon,l,m}$ is the probability amplitude of a state with an energy ϵ, and angular and magnetic quantum numbers l and m, respectively. When the electron is sufficiently far away from its parent ion, such that they no longer interact, all the energy of the electron is kinetic, i.e $E_{kin} = \epsilon$. The interaction between the atom and the XUV field is described, to a very high degree of accuracy, by first order time-dependent perturbation theory. By formally taking the limit $t \to \infty$, the first order probability amplitude $c^{(1)}_{\epsilon,l,m}$ can be written with the help of the spectral representation of the XUV field $E_{XUV}(\Omega)$,

$$c^{(1)}_{\epsilon,l,m} = \frac{e}{i\hbar}\langle \epsilon, m, l|\hat{r}|g\rangle E_{XUV}(\Omega)\delta\left(\hbar\Omega + E_g - \epsilon\right), \tag{3.2}$$

where $|g\rangle$ is the initial state, the bound ground state with an energy E_g, and $|\epsilon, m, l\rangle$ is the continuum final state. The Dirac delta expresses energy conservation, which must be fulfilled once the interaction is over. Figure 3.1(a) shows a schematic energy level diagram and the resulting experimental signal from ionization of an atom A using a frequency comb of three harmonics.

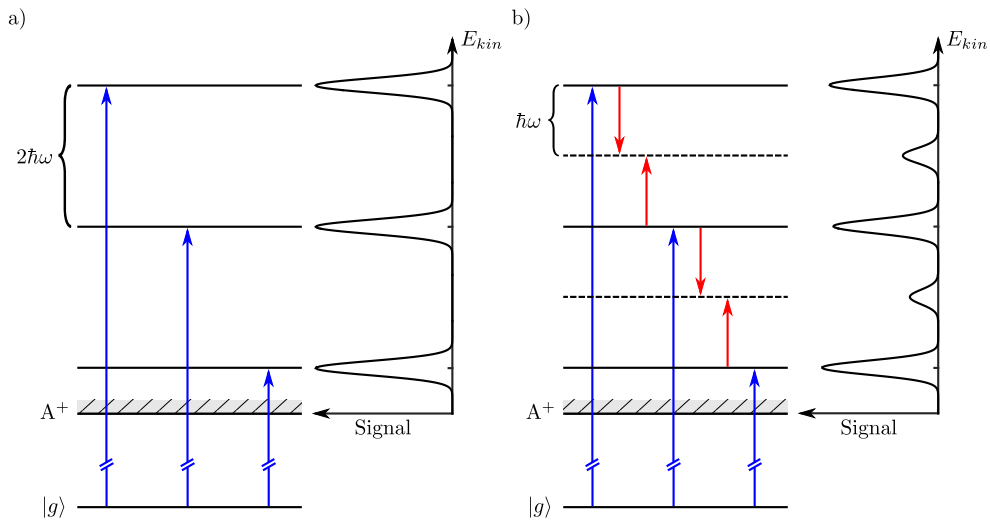

Figure 3.1: a) Photo-ionization of an atom A by a harmonic frequency-comb with a line-spacing of 2ω. (b) Two-color two-photon ionization of the same system as in (a), by a combination of the harmonic frequency-comb and a probe field with an angular frequency of ω.

3.2 Photoelectron interferometry - The RABBITT technique

Our interferometric method is based on the RABBITT (Reconstruction of Attosecond Beating by Interference of Two-photon Transitions) technique, which consists in recording photoelectron spectra of two-photon two-color ionization, i.e., the process illustrated in Fig. 3.1(b). The second color field is generally a weaker copy of the IR pulse used to drive the harmonic generation, which is overlapped with the XUV pulse train at the experimental target. The two-photon transitions generate new peaks (called sidebands) in the photoelectron spectrum. These peaks appear at positions that correspond to a one-photon transition driven by an even order harmonic, since the spacing between the harmonic lines in the spectrum is twice the energy of an IR photon. The RABBITT scheme requires that the field strength of the IR field, the probe field, be sufficiently high to induce two-photon transitions, but not so strong that the probability for higher order transitions becomes non-negligible [66]. The combined action of the XUV- and probe fields can then be treated by second-order perturbation theory. The probability amplitude for the two-color two-photon interaction is in the

limit $t \to \infty$,

$$c^{(2)}_{\epsilon,l,m} = \lim_{\varepsilon \to +0} \frac{e^2}{i\hbar^2} E_{XUV}(\Omega) E_{IR}(\omega) \sum_{\nu} \frac{\langle \epsilon, m, l | \hat{r} | \nu \rangle \langle \nu | \hat{r} | g \rangle}{\hbar\Omega - E_\nu + E_g - i\varepsilon} \delta(\hbar\Omega \pm \hbar\omega + E_g - \epsilon), \quad (3.3)$$

where the sum integral runs over all eigenstates, ν, of the field-free Hamiltonian, both its bound and continuum spectrum, and $E_{IR}(\omega)$ is the Fourier transform of the probe field. The parameter ε, which tends to zero from the positive side, is introduced to make the integral well defined despite the pole at $E_\nu = \hbar\Omega + E_g$. Again, the Dirac delta function guarantees that the energy is conserved when the interaction is over. After the two-photon transition, one XUV photon has been absorbed and one probe field photon has either been absorbed ($+\hbar\omega$) or emitted ($-\hbar\omega$). This means that the same sideband state can be reached via interaction with different spectral components of the XUV field, as indicated in Fig. 3.2(b). Temporarily ignoring the fact that the transition can be made in a number of angular momentum channels, as stipulated by the dipole selection rules, the spectral signal, S_q, at an energy corresponding to an even harmonic transition $\epsilon = \hbar q\omega - E_g$ is,

$$S_q \propto \left| c_q^{(2,+)} + c_q^{(2,-)} \right|^2, \quad (3.4)$$

where $(+)$ and $(-)$ denote the contributions to the total amplitude associated with absorption and emission of a probe field photon, respectively. Equation 3.4 can be rewritten by introducing the phases $\phi_q^{(2,\pm)}$ as the argument of $c_q^{(2,\pm)}$,

$$S_q \propto \left| c_q^{(2,+)} \right|^2 + \left| c_q^{(2,-)} \right|^2 + \left| c_q^{(2,+)} \right| \left| c_q^{(2,-)} \right| 2\cos\left(\phi_q^{(2,+)} - \phi_q^{(2,-)} \right), \quad (3.5)$$

which shows that the sideband amplitude is sensitive to the relative phase between the probability amplitudes involved. Referring to eq. 3.3 it is clear that these phases can be decomposed into three terms,

$$\phi_q^{(2,+)} = \phi_{q-1} + \phi_1 + \phi_{q-1}^{T(2)} \quad (3.6)$$

where ϕ_{q-1} is the phase of the $(q-1)^{th}$ harmonic field, ϕ_1 is the phase of the probe field and $\phi_{q-1}^{T(2)}$, the argument of the two-photon dipole transition matrix element induced by these two fields. Since $E_{IR}(-\omega) = E_{IR}(\omega)^*$ we also have,

$$\phi_q^{(2,-)} = \phi_{q+1} - \phi_1 + \phi_{q+1}^{T(2)} \quad (3.7)$$

The phase delay of the probe field relative to the XUV pulse train, $\tau = \phi_1/\omega$, can be controlled in an adjustable delay line. By recording a spectrogram composed of two-color photoelectron spectra at different values of τ, the phase information can be retrieved. Figure 3.2 shows a schematic RABBITT spectrogram and illustrates how the sideband signal oscillates when τ is scanned. The phase of the sideband oscillation only depends on the phase difference between the matrix elements associated with the transition to the sideband state,

$$\phi_q^{(2,+)} - \phi_q^{(2,-)} = 2\omega\tau - (\phi_{q+1} - \phi_{q-1}) - (\phi_{q+1}^{T(2)} - \phi_{q-1}^{T(2)}) \quad (3.8)$$

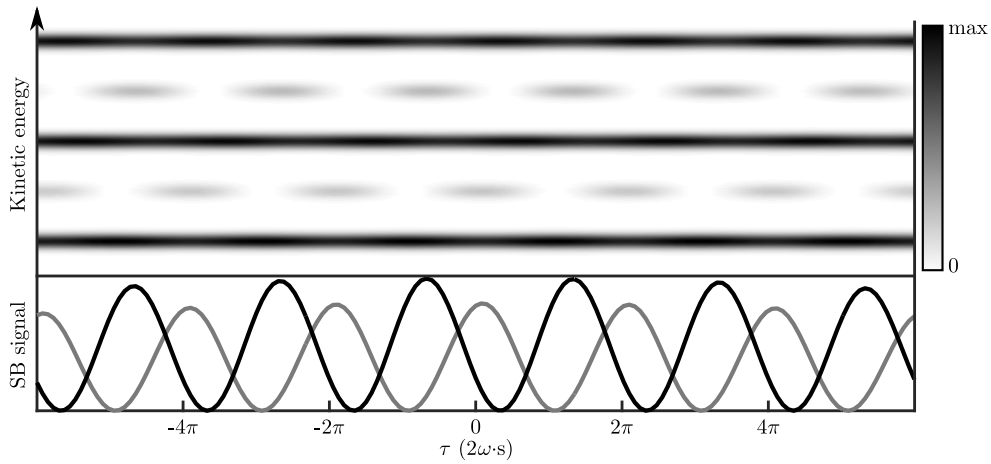

Figure 3.2: Upper panel, schematic RABBITT spectrogram showing how the two-color two-photon photoelectron spectra from three harmonics and a probe field changes as a function of τ. Lower panel, the signal integrated over the sideband peaks. The black curve and the gray curve correspond to the high energy and low energy sideband, respectively.

The sideband signal can therefore be analyzed in terms of the following equation,

$$S_q = A_q + B_q \cos\left(2\omega\tau - [\phi_{q+1} - \phi_{q-1}] - [\phi_{q+1}^{T(2)} - \phi_{q-1}^{T(2)}]\right), \tag{3.9}$$

where A_q and B_q depend on the intensity of the fields involved, the strengths of the transitions, the density of the target and the detection efficiency. The phase of the oscillation can be retrieved independently of these parameters via curve fitting or a numerical Fourier transform of the sideband signal, since it is spectrally separated and free of background.

3.2.1 Applications of RABBITT

The RABBITT method was originally introduced as a tool for characterizing the spectral phase of the XUV pulse train. Together with a measurement of the relative spectral amplitudes of the harmonics, E_q, the relative spectral phases, $\phi_{q+1} - \phi_{q-1}$ can be used to reconstruct the temporal structure of the average pulse in the XUV pulse train. The relative amplitudes of the harmonic fields can be extracted from a photoelectron spectra given that the photon energy dependent photoionization partial cross section of the target is known. The intensity profile of the average pulse is given by,

$$I_{XUV}(t) \propto \left| \sum_{q\ odd} E_q e^{i\phi_q - iq\omega t} \right|^2 . \tag{3.10}$$

The spectral phases can be determined, up to a constant, by summing up the relative phases cumulatively,

$$\sum_{n=q_i}^{q} \phi_{n+1} - \phi_{n-1} = \phi_{q+1} - \phi_{q_i - 1}, \tag{3.11}$$

where q_i is the lowest order sideband of the sidebands in the recorded spectrogram. Measuring the phase relation between consecutive harmonics is also equivalent to determining the spectrally resolved group delay of attosecond pulses, τ_q^{XUV}, within the finite difference approximation,

$$\tau_q^{XUV} = \frac{\phi_{q+1} - \phi_{q-1}}{2\omega} \tag{3.12}$$

As explained in Section 2.5, this aspect was used in Paper **IV** to characterize the effect of the generation conditions on the timing of the attosecond pulses relative to the fundamental field.

A reconstruction of the attosecond pulses using the RABBITT method requires that the phases of the two-photon dipole transition matrix element can be either neglected or calculated [67–73] (see eq. 3.9). In Papers **I**, **II**, **III** and **V** it is instead measurements of this phase contribution that constitute the main results. Just as the relative spectral phases of the harmonic fields are associated with a group delay of the XUV pulses, the relative phases of the transition matrix elements constitute an additional group delay of the emitted electron wave packet,

$$\tau_q^{T(2)} = \frac{\phi_{q+1}^{T(2)} - \phi_{q-1}^{T(2)}}{2\omega}. \tag{3.13}$$

This delay is a consequence of the interaction between the escaping electron, the probe field, and the ionic core that takes place when the electron has made a transition to a continuum state [74]. The group delay of the electron wave packet thus carries a signature of the ultrafast dynamics of photoionization, which is accessible with photoelectron interferometry.

By identifying the spectral phase differences encoded in the second order transition amplitude as a spectrally resolved group delay of the second order continuum wave packet enables us to write the equation for the sideband modulations in a RABBITT spectrogram in a more compact and intuitive form,

$$S_q = A_q + B_q \sin(2\omega[\tau - \tau_q^{XUV} - \tau_q^{T(2)}]). \tag{3.14}$$

3.2.2 Conditions for RABBITT

When implementing the RABBITT method and interpreting the results, it is important to keep in mind that this approach is only valid under the condition that second-order perturbation theory is applicable. It is therefore necessary to have precise control of the probe pulse energy. In order to obtain a sense of the general validity of this approximation, it is instructive to study the same process under a different approximation, namely the strong field approximation. As explained in Section 2.3.2, this approximation assumes that the continuum wave functions are plane waves, which is a consequence of ignoring the interaction between the ionized electron and the ionic core. The probability amplitude of a continuum state with a final momentum $\mathbf{p}$ after interaction with the APT and the probe pulse is then [75, 76],

$$c_{\mathbf{p}} = \int_{-\infty}^{\infty} dt' \; \mathbf{E}_{XUV}(t') \cdot \langle \mathbf{p} + \mathbf{A}(t') | \hat{r} | g \rangle e^{-i\frac{1}{\hbar}\int_{t'}^{\infty} dt'' \frac{\hbar^2}{2m}[\mathbf{p}+e\mathbf{A}(t'')]^2 + I_p}, \tag{3.15}$$

where $\mathbf{E}_{XUV}$ is the electric field of the APT and $\mathbf{A}$ is the vector potential of the probe pulse. Just as for the SFA expression for HHG, eq. 3.15 can be interpreted in terms of a sequence of events. The electron emerges in the continuum at a time t' when it is ionized by the APT. It then propagates with an average momentum $\mathbf{p}$, which is modulated by the vector potential of the probe field. Mathematically, the integral takes the form of a Fourier transform of the one photon probability amplitude, frequency modulated via the action of the probe field. The dominant time-dependent term in the exponential phase factor is proportional to $\mathbf{p} \cdot \mathbf{A}(t'')$, meaning that the energy modulation amplitude is proportional to the final momentum. As a consequence the probability of sideband formation increases with the energy of the photoelectrons.

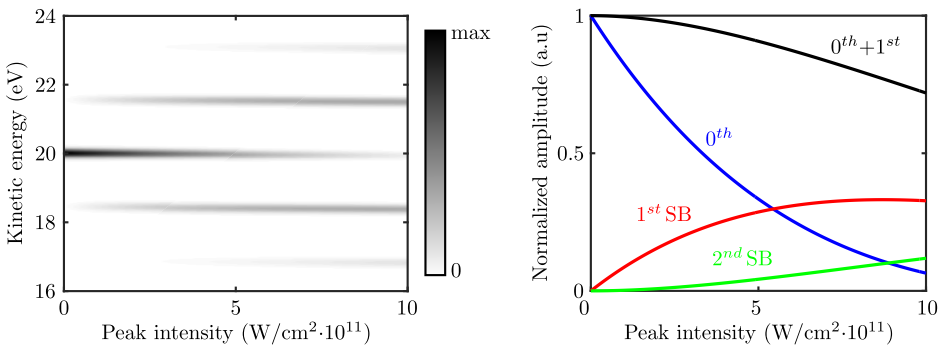

Figure 3.3: SFA calculation of photoelectron spectrum as a function of probe pulse intensity.

The left panel of Fig. 3.3 shows the spectrum of photoelectrons with an initial kinetic energy of 20 eV as a function of the peak intensity of a 30 fs long probe pulse with a central wavelength of 800 nm, calculated using eq. 3.15. As the probe field strength increases sidebands start to form. From the perspective of perturbation theory, sideband formation is a consequence of absorption or emission of an additional photon. From the perspective of the strong field approximation, sideband formation instead has to be understood as a consequence of a periodic energy modulation of the continuum wave packet driven by the probe field. Increasing the intensity further results in the appearance of additional sidebands. Explaining the this process within a perturbative model requires that the model is extended to third-order perturbation theory that accounts for the interaction with yet another probe field photon.

The right panel of Fig. 3.3 shows the integrated signals over the central peak (labeled 0^{th}) and the first and second order sidebands. The black curve indicates the ratio to which the central peak and the first order sidebands account for the total signal. It can be shown, via manipulations of eq. 3.15, that these curves are described by generalized Bessel functions (of zeroth-,first- and second order).

Second order perturbation theory predicts that the first order sideband should grow linearly with the probe pulse intensity. Furthermore, if no higher order processes is accounted for, the probability density should only be redistributed from the central peak to the first order sideband. Figure 3.3 indicates that these predictions start to be wrong for electrons with a kinetic energy of 20 eV, when the probe pulse intensity exceeds $3{\cdot}10^{11}$ W/cm^2.

When dealing with extremely broadband XUV pulses (several tens of eV) it is

challenging to set the intensity of the probe pulse such that the RABBITT conditions are fulfilled over the entire spectral range, while still managing to have detectable sidebands on the low energy side.

3.3 Detection of photoelectrons

Most of the results in this thesis (Papers **I-IV**) have been obtained using a magnetic-bottle electron spectrometer (MBES). In this instrument the kinetic energy of the photoelectrons, emerging from an effusive gas jet target, is analyzed by determining the photoelectron flight-time in a drift tube. The main advantage of this instrument is its high collection efficiency, which is enabled by a magnetic field designed to direct the electron towards the microchannel plates at the end of the drift tube, independently of its emission angle and without altering its kinetic energy [77]. The field lines of this guiding magnetic filed, schematically outlined in Fig. 3.4, maps out the shape of a bottle. The bottle shaped magnetic field lines have given the instrument its name. The

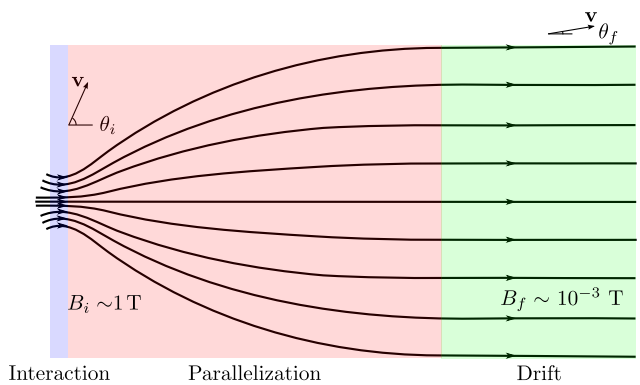

Figure 3.4: Schematic diagram the magnetic field in a MBES, adapted from [77].

strong, divergent field in the interaction region is created by an electro- or permanent magnet, supplied with one or two conical pole pieces that concentrate the magnetic field into the volume where the electrons are emitted. The weaker magnetic field in the drift region is induced by a solenoid magnet that encircles the drift tube.

An electron emitted in the interaction region with a speed v and a velocity component perpendicular to the magnetic field lines, $v\sin(\theta_i)$, will follow a helical trajectory. In a plane perpendicular to the magnetic field lines, the electron will travel in a circular, cyclotron motion with a radius

$$r_i = \frac{vm\sin(\theta_i)}{eB_i}, \tag{3.16}$$

while drifting into the parallelization region, due to its longitudinal velocity component. If the variation of the magnetic field that the electron experiences changes negligibly during one revolution of the cyclotron motion, the component of the electron angular momentum that is parallel to the magnetic field lines is conserved. We can therefore equate the final angular momentum of the cyclotron motion in the ho-

mogeneous field of the drift region, with the initial angular momentum,

$$r_i m v \sin(\theta_i) = r_f m v \sin(\theta_f), \tag{3.17}$$

which together with eq. 3.16 gives a relation between the initial and final traveling angles relative to the magnetic field lines,

$$\frac{\sin(\theta_f)}{\sin(\theta_i)} = \sqrt{\frac{B_f}{B_i}}. \tag{3.18}$$

The momentum of the electron is thus essentially parallel to the magnetic field lines once it reaches the drift region. The transition from the high to low field region should be made relatively short, a few mm, so that the travel time of the electron from the interaction region to the detector is a good measure of the particle speed, independently of the emission angle from the target. However, the transition should not be made over a too short distance. The magnetic field gradient then becomes too large for the adiabatic approximation to be valid, i.e the magnetic field strength changes significantly during one revolution of the electron cyclotron motion.

The time-of-flight (TOF) of the electrons is recorded by a time-to-digital converter that registers the time between two trigger events. The first is generated by a photodiode that fires when hit by the laser pulse, and the second by the electron impact on the MCP. From a recorded list of TOFs, a histogram is constructed that, after rebinning from time to energy bins, constitutes a photoelectron energy spectrum. The conversion between TOF and kinetic energy in eV is accomplished using the formula [78],

$$E_{kin} = \left(\frac{m}{2e}\right)\left[\frac{L}{T+T_d}\right]^2 + V_a + V_r, \tag{3.19}$$

where L is the length of the drift tube, T is the TOF and T_d is the delay of the first trigger event relative to the true emission time of the electron. A voltage V_a can be applied to a grid located in the drift tube to slow the electrons down, and thereby increase the energy resolution. V_r is any residual voltage not accounted for when measuring V_a. A calibration of the energy scale is achieved by fitting eq. 3.19 to a range of spectral peaks with known energies, generally using L, T_d and V_r as free parameters.

Equation 3.19 also dictates that the energy resolution (ΔE_{kin}) is related to the TOF resolution (ΔT) by,

$$\frac{\Delta E_{kin}}{E_{kin}} = \frac{2\Delta T}{T}. \tag{3.20}$$

The energy resolution is thus better at low electron energies. Furthermore long drift tubes (long TOF) are to prefer from a resolution point of view. The time resolution is in general limited by the efficiency in the parallelization of the electron momentum.

The spectroscopic results presented in Papers **I-V** are obtained using a MBES that collects electrons emitted over a solid angle of 2π steradians. The strong magnetic field in the interaction region of this instrument is created by an electromagnet mounted on the outside of the vacuumchamber and two hollow conical pole pieces facing each other from opposite sides of the interaction region (similar to the instrument described in [77]). The 0.8 m drift tube is encircled by a solenoid magnet and two Helmholtz-coils which compensate for the Earth's magnetic field.

The results presented in Chapter 5, on Auger electron spectroscopy, were obtained with a different instrument. This other MBES collects electrons emitted over a solid angle of 4π steradians. The magnetic field in the interaction region forms a magnetic mirror that is created by a permanent magnet with a single conical pole piece, mounted inside the vacuum chamber, as in refs. [79, 80]. The 2 m drift tube is encircled by a solenoid magnet and screened from the Earth's magnetic field by a μ-metal shield.

3.4 Optical interferometers for photoelectron interferometry

From an experimental perspective RABBITT is equivalent to a cross-correlation measurement between an APT and an optical pulse. Interferometry in general requires good experimental stability and precise control. In attosecond science this is particularly true. To shift the arrival time of an electromagnetic pulse on target by 100 as, it is sufficient to alter its optical path-length by only 30 nm. Optical experimental setups for photoelectron interferometry are therefore built as two-color interferometers, with a high requirement on interferometric stability.

Here, two of these setups are described which were both used to obtain some of the results presented in this thesis. The first one was constructed before I joined the Lund attosecond physics group and is therefore referred to as the old setup. The second setup was built during this thesis work and will therefore be refereed to as the new setup. I contributed largely to the design and building of this experimental setup.

3.4.1 Old setup

The photoelectron interferometry experiments presented in Papers **I-IV** were performed using the optical setup schematically outlined in Fig. 3.5.

The setup consists in a Mach-Zehnder type interferometer with a gas-cell inserted in one of the arms for generation of high-order harmonics. The other arm guides the probe pulse to the active region of the electron spectrometer.

The output beam from the laser is split by a thin (3 mm) beam-splitter. Seventy percent of the pulse energy is focused by a spherical mirror (or an off-axis parabolic mirror) through an open-ended gas cell into which the generation gas is released in a pulsed manner, synchronized with the arrival of the pulse. The IR-beam is then blocked and separated from the generated XUV beam by a thin foil. The XUV beam is passed through a hole in the center of the mirror that re-combines the two arms of the interferometer, and is then focused by a gold coated toroidal mirror onto the gas target in the interaction region of the MBES. Focusing of the XUV beam is performed in a 2f-2f configuration, i.e. the toroidal mirror images the point where the beam is generated in the gas target.

The remaining 30% of the IR pulse energy goes into the probe arm of the interferometer. In order to be able to adjust the pulse energy to the experimental conditions, a rotatable half-wave plate and two reflective polarizers are mounted in the beam path. The pulse is passed through a delay line for course adjustments of the probe delay. Fine adjustments and scans of the delay are achieved by translating a mirror using a piezo-eletric actuator. The outer part of the beam is reflected off the recombination mirror and overlapped in time and space with the APT in the electron spectrometer. The recombination mirror has a curvature designed to create a virtual focus of the

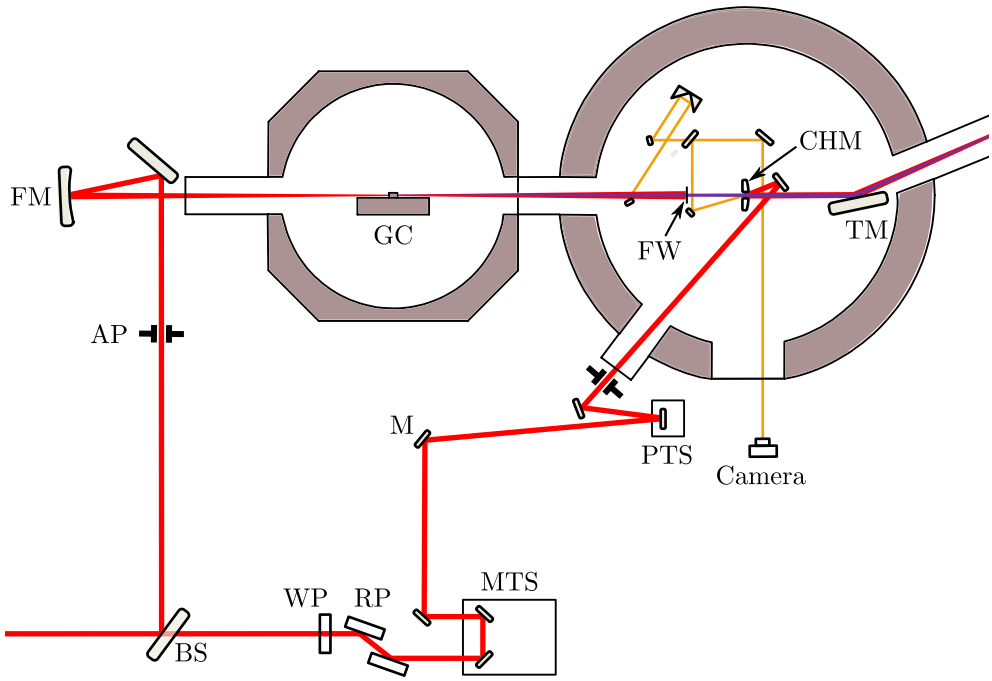

Figure 3.5: Optical setup for attosecond interferometry experiments. The labels are abbreviations of: AP, aperture; BS, beam-splitter; CHM, curved holey mirror; FM, focusing mirror; FW, filter-wheel; GC, gas-cell; M, mirror; MTS, motorized translation-stage; PTS, piezoelectric translation-stage; RP, reflective polarizers; TM, toroidal mirror; WP, half-wave plate.

collimated probe beam at the position of the HHG gas cell in order for the XUV- and IR to focus at the same position.

The beam path marked in yellow in Fig. 3.5 constitutes a second interferometer, which is designed to monitor and control the probe pulse delay. The part of the probe beam that leaks through the hole in the recombination mirror is combined with a part of the generation beam picked off by a small d-shaped mirror on a beam splitter. The two beams are then crossed, at a small angle, at a camera chip. The camera is provided with an interference filter that limits the bandwidth of the incident beams. The spatial interference pattern that forms on the camera when the two pulses overlap is used to create an error signal for a feed-back loop that controls the piezoelectric delay stage in the probe arm. The automatic control is implemented using a simple proportional-integral-derivative software controller. Its parameters are manually tuned to make the actual measured delay best follow a few fs step in the desired delay. This additional stabilizing interferometer serves two purposes, as discussed below.

In the experiments presented in Papers **I**, **III** and in the coincident measurements presented in Chapter 5, the signal level from the relevant process was relatively weak (less then 1 electron collected per laser shot). Under such conditions it is important to minimize the time jitter between the APT and the probe pulse, in order to obtain good quality statistics. A low signal also means that the time to record a spectrogram

is long. Slow drifts in the probe delay then become a potential problem. Since the signal is periodic (see Fig. 3.2) slow drifts can be partly compensated for in the data treatment, but this introduces an uncertainty that also degrades the statistical quality of the data.

In Papers **II** and **IV** the results were obtained by comparing spectrograms recorded using harmonics generated under different conditions and with different target gases, respectively. This comparison relies on the fact that the same range of probe delays can be scanned in a reproducible manner, which requires a reliable way to keep track of the probe delay.

The short term timing jitter is substantially reduced by the active stabilization of the main interferometer. For a measurement of 6 min the RMS in the measured delay drops from 200 as to 50 as when the active stabilization is switched on. The long term drift, however, has proved difficult to completely eliminate.

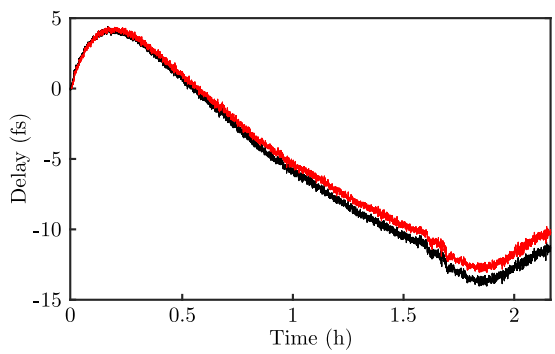

Figure 3.6: Delay measurements over time from the interferometer in a non-stabilized mode. The black curve is a recording of spatial fringes formed after the recombination of the beams. The red curve, a recording of spatial fringes in the interferometer with the beam path marked in yellow in Fig. 3.5.

Figure 3.6 shows a measurement of the long term interferometric stability. The red curve represents the probe delay measured by the small interferometer. The black curve shows the actual probe pulse delay, measured after the point where the two main beams are recombined. This measurement was performed by directing the beams towards a camera and forming an interference pattern by slightly misaligning the recombination mirror. The data were recorded using a He-Ne CW laser and not the IR laser, since the main aim was to study how the thermal load from the high-power beam affected the system. At the beginning of this measurement the IR-beam was let into the setup and the stabilization software was turned off. The IR beam was then left as it was for the entire time of the measurement. The thermal load on the optical components form this high-power laser beam induces a drift in the path length difference between the arms such that the delay of the probe pulse changes on a fs scale over hours. This effect should in principle be compensated for by the feed-back loop. However, the length of the beam path marked in yellow in Fig. 3.5 also drifts, which is shown by the fact that the two curves in Fig. 3.6 gradually separates. After two hours they are separated by about 1.5 fs. In a situation where the feed-back loop controls the delay of the probe pulse the error signal fed to the control software slowly becomes more and more incorrect due to this effect. To minimize this drift it

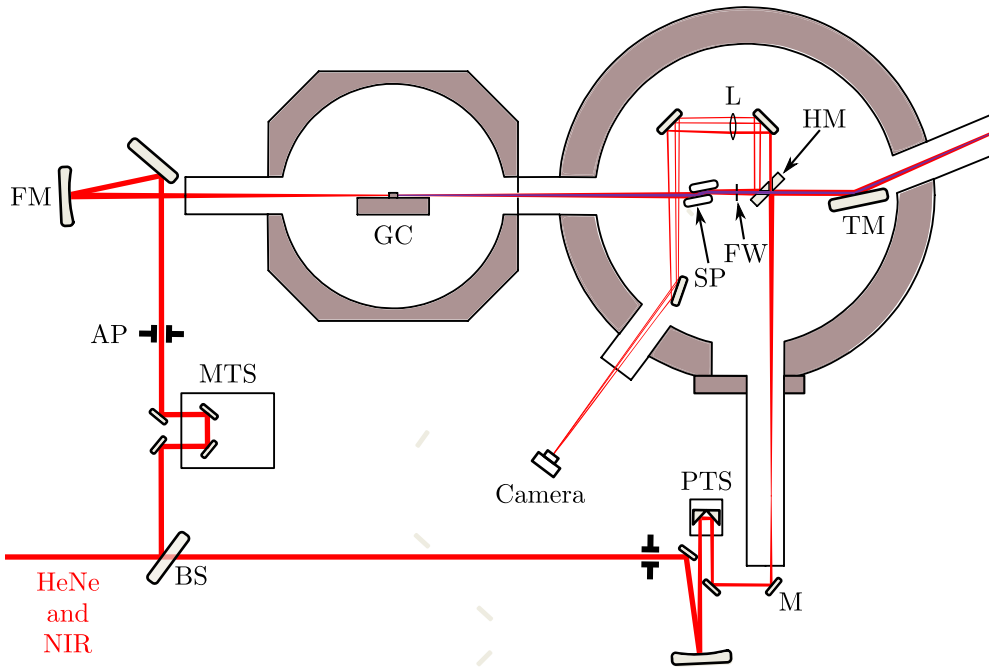

Figure 3.7: Plans for re-building of the optical setup presented in Fig. 3.5. The labels are abbreviations of: AP, Aperture; BS, beam-splitter; FM, focusing mirror; FW, filter-wheel; GC, gas-cell; HM, holey mirror; L, lens; M, mirror; MTS, motorized translation-stage; TM, toroidal mirror; SP, Anti-reflection coated silica plates.

is important to let the system reach a thermal equilibrium before data that depend on interferometric stability are recorded.

Outlook - A plan for improvements

Plans are presented below for a new version of the optical setup in Fig. 3.5. The main aim of this new version is to overcome the difficulties of maintaining a long term interferometric stability as discussed above. Fig. 3.7 shows the planed modifications. As in Fig. 3.5, the Mach-Zehnder type interferometer remains the main building block in the design, but the new version contains a number of conceptual changes. The curved recombination mirror has been replaced by a flat holey mirror. Instead of imaging a virtual focus, the toroidal mirror images a real focus in the probe arm into the target in the electron spectrometer. This modification lowers the level of complexity in the manufacturing of the drilled recombination mirror. It should also offer more flexibility for making small adjustments of the position and quality of the probe focus at the experimental target.

A pair of silica plates with high optical quality surfaces has been added in the XUV-beam path. At gracing incidence a high fraction of the harmonic beam is reflected off these plates, while most of the co-propagating IR pulse is transmitted through the front surfaces, thanks to a broadband multilayer anti-reflection coating. This

modification was introduced to separate the APT from the driving pulse before it is transmitted through the thin spectral filter foil. From experience we learned that there is otherwise a substantial risk, depending on the material of the foil, that foils will break, due to the heat load exerted on them by the IR-laser pulse. According to the manufacturer, the pair of silica plates should attenuate the IR beam such that only 2% of the power remains after two reflections.

The main reason for considering a redesign of the setup was, a mentioned, to improve the long term interferometric stability. The approach based on an active stabilization of the probe pulse delay in a feed-back loop is kept, but the delay is monitored by applying a design was inspired by the experimental setups described in refs. [81, 82], which both report a good long- and short-term interferometric stability. The relative optical path length of the interferometer arms is probed by a HeNe laser beam that co-propagates with the NIR laser pulse. The idea is to avoid that the beam path used to monitor the stability deviates from the paths of the main beams. The HeNe beam is therefore picked off from the generation arm first at the recombination mirror, via a reflection from its backside. This beam is then parallel with the part of the probe beam that leaks through the hole in front side of the mirror. Since the mirror substrate is thick (5 mm), passing two orthogonal beams through the mirror required that two channels be drilled in the substrate. The two channels meet at the front side of the mirror. The beams emerging form the backside are, however, displaced by 7 mm with respect to each other. These two, originally diverging beams, are then crossed via a positive lens. Where they overlap, spatial interference fringes are formed. As previously described, these fringes are registered by a camera and processed by a software. In order to prevent that a thermal expansion of the recombination mirror causes a non-registrable drift, its substrate is made of Zerodur, a glass with an extremely small thermal expansion coefficient.

In order for this scheme to work, a sufficiently large fraction of the power in the HeNe laser beam has to be transmitted past the pair of silica plates and the filter foil. The anti-reflection coating of the silica plates does not cover the wavelength of the HeNe laser (633 nm), and the pair transmit about 40% of the incoming power at this wavelength. The filter foils are held by custom made silica mounting rings. The diameter of the circular filters are only 2.5 mm, which allows for the outer part of the laser beam to pass around it.

The design has been partially verified by both computer ray-tracing and via a model setup built within the framework of a BSc-thesis work [83], supervised by me. This setup will soon be fully implemented and should lead to better long interferometric stability.

3.4.2 New setup

The results presented in Paper **V** were obtained using the optical interferometric setup designed and constructed as part of the work of this thesis and outlined in Fig. 3.8. In addition to being actively stabilized, this interferometer was designed to promote interferometric stability by being intrinsically resistant to vibrations and beam-pointing drifts that could induce a jitter and drift in the probe pulse delay.

All optical components are maintained under vacuum, except for a folding mirror and the beam splitter that splits the pulse. The separation between the two arms is only 10 cm, which allows the setup to be relatively compact. In both arms of

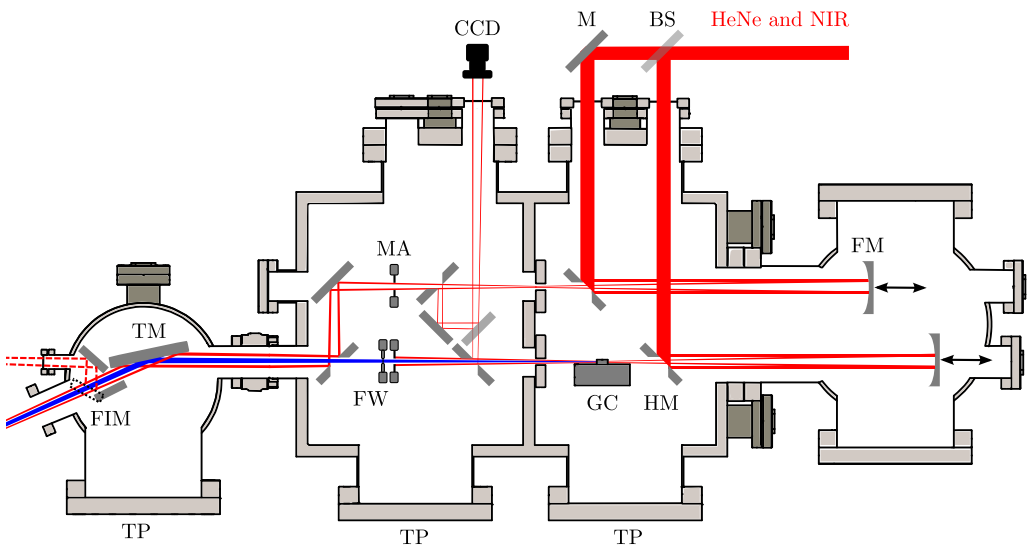

Figure 3.8: Optical setup for attosecond interferometry experiments. The labels are abbreviations of: BS, beam-splitter; FIM, flip-in mirror; FM, focusing mirror; FW, filter-wheel; GC, gas-cell; HM, holey mirror; M, mirror; MA, motorized aperture; TM, toroidal mirror; TP, turbomolecular pump.

the interferometer the beams are guided by an odd number of 45° and 0° incidence angle reflections and are focused using mirrors with the same radius of curvature. According to computer ray-tracing, simulations these conditions should minimize any relative arm length shift induced by an angular shift of the incoming laser beam [84].

The incoming beam is split on a beam splitter that directs 70% of the incident power to the arm in which the harmonic light is generated. Both of the beams are folded on holey mirrors and focused back though the hole in the folding mirror. In this configuration, off axis incidence on the spherical mirrors is avoided, which would otherwise generate astigmatic beams. The ray-tracing simulations also indicate that, the reduction of abberations should result in an intensity in focus which is about the same as if the full beam were to be focused on a position slightly off the optical axis of the spherical mirror, even though the central, most intense, part of the beam is dumped when passing the folding mirror.

The approach of using hollow beams has two advantages. Firstly, since this setup is intended for interferometric experiments it is important that the wave fronts over the experimental target volume be as flat and uniform as possible. A distortion of the probe beam wave front would, for example, mean that the phase delay, τ, varies across the focal volume, which in turn would reduce the contrast or visibility of the modulations in the photoelectron sidebands. Since the re-focusing of the beams is accomplished using a single toroidal mirror, it is difficult to retroactively correct an already distorted wave front. Secondly, even though the fundamental beam is hollow, the harmonic light is emitted mainly on the optical axis. Furthermore, the divergence of the plateau harmonics generated from short trajectories is generally smaller than the divergence of the fundamental beam [85]. By placing an adjustable aperture in

the far field of the generation point, most of the fundamental light can be removed from the beam without significantly attenuating the XUV pulses. This means that thin foils usually used for this task are exposed to less risk of being damaged. If there is no need for spectral filtering of the harmonic light, the filters can even be removed.

The probe pulse delay is monitored in a similar fashion to that described previously. Before entering the optical setup, the IR laser beam is combined with the beam from a frequency stabilized HeNe laser. Using holey mirrors, the outer parts of the HeNe beam are later picked off and re-combined via a beam splitter on a CCD camera chip. In order for spatial linear interference fringes to appear, one of the pick-off mirrors is slightly misaligned. The software generated feed-back signal, based on the phase of the fringes, is fed to a translation stage with a piezoelectric actuator that translates the focusing mirror in the probe arm. Both of the spherical mirrors can also be translated over a longer range (63 mm) via linear translation-stages mounted under the mirror holders. This allows for a precise positioning of the generation beam focus relative to the gas cell where the harmonic light is generated and also allows for coarse adjustments of the probe pulse delay.

After passing the toroidal mirror, the IR beam can by picked out via a motorized flip-in mirror and diagnosed. RABBITT measurements are very sensitive to any deviations from co-linearity between the harmonic and probe beams, since their wave fronts have to be parallel to achieve good contrast in the sideband modulations. The co-linearity and temporal overlap between the generation and probe pulse can be routinely checked and controlled via the beam pick-out.

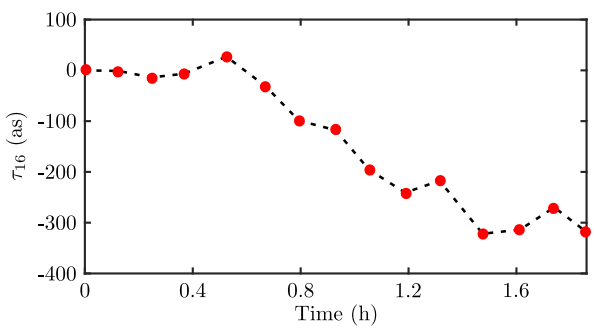

Figure 3.9: Delay of sideband 16 extracted from 15 RABBITT spectrograms, recorded under the same conditions, one after another during 1.8 hours.

The RMS jitter of the probe pulse delay is typically about 50 as when the interferometer is stabilized. The main contribution to this jitter is most likely vibrations at frequencies that exceed the update frequency of the feed-back loop. The bottleneck in the loop is the camera read out.

To obtain an estimate of the long term stability of the interferometer a series of RABBITT spectrograms were recorded one after another, under the same conditions, for 1.8 hours. Figure 3.9 shows the evolution of the delay ($\tau - \tau^{XUV} - \tau^{T(2)}$) of sideband 16 extracted from each spectrogram. The result suggests that there is a drift of the probe pulse delay (τ) of 300 as during this time. This is a substantial improvement relative to what could be achieved with the setup previously presented (about 1 fs drift per hour).

Chapter 4

Atomic phases and time delays

This chapter introduces the concept of time delays of wave packets in quantum mechanics. The connection with the phase measured by the RABBITT trace is described. The chapter also reviews a series of experiments (described in Papers **I-II** and **V**) where phases and delays of electronic wave packets where measured for different atomic species and ionization mechanisms.

4.1 Time delays of scattering wave packets

The concept of time delays in quantum mechanics was originally introduced by Wigner and Eisenbud within the framework of scattering theory [86]. In this context the time delay is defined as an asymptotic shift in the arrival time of a scattered wave packet due to the interaction with a scattering potential. For simplicity, here we consider a one-dimensional geometry, however, with a few modifications the same reasoning applies to the radial dimension of a three-dimensional problem if the scattering potential is spherically symmetric.

In the case where the potential is of limited range, the scattered wave packet can be written as a superposition of the free particle solutions to the Schrödinger equation, i.e plane waves, outside of this range. A wave packet that is traveling along the positive x-axis which has interacted with a potential, $V(x)$, ranging from 0 to a can in the region $x > a$ be written,

$$\Psi_{out}(x,t) = \int_p dp\ |c_p| \exp\left[i\left\{\frac{p}{\hbar}x - \frac{p^2}{2m\hbar}t + 2\eta(p)\right\}\right] \tag{4.1}$$

where p is the particle momentum. Assuming that the potential is sufficiently smooth, such that reflections can be neglected, the interaction with the potential does not significantly alter the amplitude, $|c_p|$. It does however induce a phase shift, $2\eta(p)$, relative to the phase of the incoming wave (which here is assumed to be zero). Physically, this phase shift originates from the fact that the local momentum,

$$p(x) = \sqrt{2m([E - V(x)])}, \quad 0 < x < a \tag{4.2}$$

where $E = p^2/2m$, is different from the asymptotic momentum, p, which the particle achieves outside the range of the potential. The phase that a given wavelet accumulates

within this region is thus different from what it would be if the potential were absent ($V(x) = 0$). Depending on whether the potential is attractive ($V(x) < 0$) or repulsive ($V(x) > 0$), the phase shift is positive or negative, respectively. Technically, the phase $\eta(p)$, called the scattering phase, is found by matching the solution of the time-independent Schrödinger equation that is outside the range of the potential to the solution that is inside, i.e. at the boundary between the regions [87].

The integrand in eq. 4.1 is an oscillating function with non-linear phase. Since rapid phase variations generally lead to destructive interference, the main contributions to the integral are given by instances of x and t, where a stationary phase coincides with the peak of the momentum distribution [88]. Equating the derivative of the phase with respect to the momentum with zero at the peak momentum, p_c, we get an equation of motion for the peak of the wave packet,

$$t = \frac{mx}{p_c} + \frac{m\hbar}{p_c}\frac{d\eta}{dp}\Big|_{p_c} = \frac{mx}{p_c} + 2\hbar\frac{d\eta}{dE}\Big|_{E_c}. \tag{4.3}$$

This shows that the wave packet is moving with a group velocity $v_g = p_c/m$ and is delayed with respect to a non-interacting wave packet by a group delay,

$$\tau_g = 2\hbar\frac{d\eta}{dE}\Big|_{E_c}. \tag{4.4}$$

4.2 Time delays in photoemission

The concepts used above to describe scattering can also be applied to photoionization. Since there is no incoming wave in this case, the interaction between the atomic potential and the escaping electron wave packet is often referred to as half a scattering event.

The concept of a scattering phase, in a case that is relevant for photoionization, is illustrated in Fig. 4.1. It displays the radial part of the hydrogen wave function with a positive energy of 15 eV and no angular momentum (s-wave), in red. The black line shows the hydrogenic Coulumb potential. For comparison, the radial part of a "free" s-wave with the same energy is displayed in gray. Due to its interaction with the potential, the phase accumulation is larger for the Coulomb wave than for the free wave, especially at small radial distances, where the potential is strong. However, the phase accumulation of the Coulomb wave is always larger than that of the free wave, at any radial distance. Since the Coulomb potential is not of limited range the interacting wave only slowly converges to a purely plane wave.

The asymptotic form of the radial part of a Coulumb scattering state with a wave vector $\mathbf{k} = \mathbf{p}/\hbar$ and angular momentum quantum number L can be written,

$$\lim_{r\to\infty} \phi_{\hat{k}}(r) \propto \sin\left(kr + \frac{\ln(2kr)}{ka_0} + \eta_L(k) - \frac{\pi L}{2}\right), \tag{4.5}$$

where a_0 is the Bohr radius. Thus, the asymptotic phase can be decomposed into two components, one dependent on the radial coordinate and one constant, which in the case of a pure hydrogenic potential takes the form,

$$\eta_L(k) = \arg\left[\Gamma\left(L + 1 - i\frac{1}{ka_0}\right)\right], \tag{4.6}$$

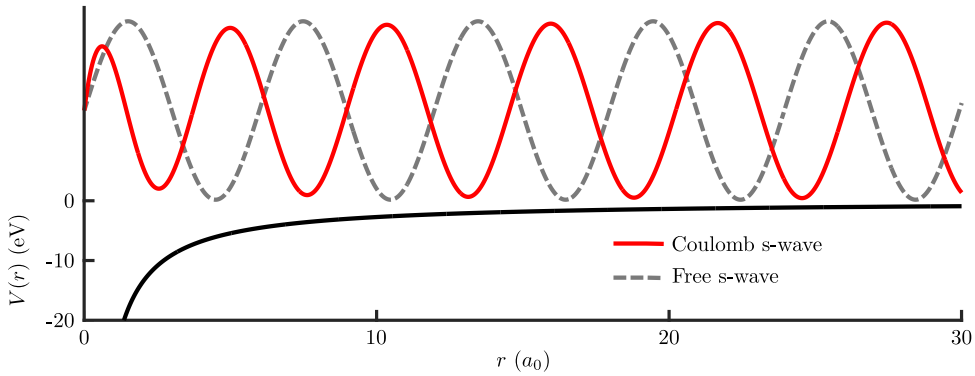

Figure 4.1: Comparison between a "free" s-wave and a Coulumb s-wave.

where $\Gamma(z)$ represents the complex gamma function. A short range deviation from a pure Coulomb potential would alter this quantity, i.e. introduce an additional phase shift, but would not change the form of the asymptotic solution to the Schrödinger equation. More complex atomic systems than hydrogen can therefore be analyzed in the same manner. As a result, the scattering phase can be said to carry a signature of the electron-ion interaction.

In a fashion similar to that in the previous section, we can define a group delay for a wave packet escaping the atom in a single angular channel L as,

$$\tau_L = \hbar \frac{d\eta_L}{dE} \tag{4.7}$$

Due to the logarithmic divergence in the phase of the asymptotic scattering state, the physical interpretation of this delay is, however, not as straight forward as in the case of a limited range potential. The group delay of a wave packet escaping a Coulomb-like potential, compared to that of a non-interacting wave packet, will depend on its radial position and can therefore not be defined in absolute terms (see ref. [65] for an elaborate discussion on this topic). This does not prevent us, however, from making meaningful comparisons between delays from different subshells (Paper **I**), different ejection mechanisms (Paper **III**) and different atomic species (Paper **II**). As long as the experiment can be designed such that one photoelectron wave packet can be referenced to one or several others the results will reveal differences in the short range interactions between the ion and the escaping electrons.

4.3 Measuring time delays in photoemission

Measuring the group delay of photoelectrons using the interferometric method presented in Chapter 3 relies on the fact that this delay can be related to the phase of the two photon transition matrix element,

$$\phi_q^{(2)} = \arg\left(\lim_{\varepsilon \to +0} \sum\!\!\!\!\!\!\int_\nu \frac{\langle \epsilon, m, l | \, \hat{r} \, | \nu \rangle \langle \nu | \, \hat{r} \, | g \rangle}{\hbar\Omega - E_\nu + E_g - i\varepsilon} \right). \tag{4.8}$$

In Papers **I-III** and **V** this relation is derived using an approximative treatment based upon perturbation theory. To do this, we consider only the asymptomatic behavior

of the continuum wave functions associated with the final, $|\epsilon, m, l\rangle$ and intermediate states $|\nu\rangle$. In the case of one angular channel L for the intermediate states, $\phi_q^{T(2)}$, can be written as [74, 89],

$$\phi_q^{T(2)} = \eta_L(\epsilon_\nu) - \frac{L\pi}{2} + \phi_{cc}(\epsilon_\nu, \epsilon), \tag{4.9}$$

where η_L is the scattering phase of the resonant state in the one photon ionizing transition from the ground state, and ϵ_ν is the energy of this state. The additional phase, ϕ_{cc} is a consequence of the continuum-continuum transition between the intermediate and final states in the presence of the long range Coulomb potential. An analytical expression for this phase is given in ref. [74]. An important property of ϕ_{cc} is that, to a very good approximation, it is independent of the scattering phase of the final state and does not depend on the angular orbital of either the intermediate (L) or final states (l). Since it does not depend on the short range behavior of the atomic potential, it is universal and can be considered a a simple correction term in the data analysis.

It is important, however, to consider the energy range within which the asymptotic approximation is valid. At low positive energies (small k) there is a slow convergence of the continuum scattering states to their asymptotic form. One cannot therefore assume that the scattering states can be treated using the asymptotic form at all radial distances. In ref. [74], it is shown that the energy range of the approximation can be extended as far down as ∼5 eV. This is achieved by introducing a correction term that takes into account the amplitude variation of the scattered wave in the long range tail of the Coulomb potential. Furthermore an *ad hoc* adjustment is introduced for the lower boundary of the radial integral representing the dipole transition from the intermediate to the final state. This adjustment is chosen such that the hydrogenic scattering phases are recovered when ϕ_{cc} is subtracted from the phases given by exact calculations of the two-photon matrix element.

In Chapter 3 we introduced the group delay $\tau_q^{T(2)}$ which, added to the group delay of the attosecond pulse train, determines the relative phase shifts of the sidebands in the RABBITT spectrogram. Considering eq. 4.9 $\tau_q^{T(2)}$ becomes,

$$\tau_q^{T(2)} = \frac{\eta_L(q+1) + \phi_{cc}(q, q+1)}{2\omega} - \frac{\eta_L(q-1) + \phi_{cc}(q, q-1)}{2\omega}, \tag{4.10}$$

where the state energy has been replaced by the order of the resonant harmonic and sideband states, i.e $\epsilon_\nu = q\hbar\omega - I_p$, in accordance with the labels in Fig. 4.2. This is

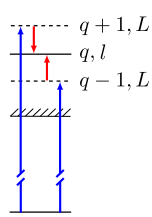

Figure 4.2: Schematic energy level diagram of the states involved in the two-photon transitions giving rise to sideband q.

equivalent to the sum of two group delays,

$$\tau_q^{T(2)} = \tau_L(q) + \tau_{cc}(q) \tag{4.11}$$

where

$$\tau_L(q) = \frac{\eta_L(q+1) - \eta_L(q-1)}{2\omega}. \tag{4.12}$$

$\tau_L(q)$ is thus a finite difference approximation of the group delay of a wave packet created via absorption of one XUV photon, i.e.

$$\tau_L(q) \approx \frac{\partial \eta_L}{\partial \epsilon}\Big|_{\epsilon = q\hbar\omega - I_p} \tag{4.13}$$

The delay originates, as explained earlier, from the short range interaction experienced by the escaping photoelectron. $\tau_{cc}(q)$ can be seen as a measurement-induced group delay, following from the fact that the original wave packet has to be manipulated in order for the measurement to reveal phase information.

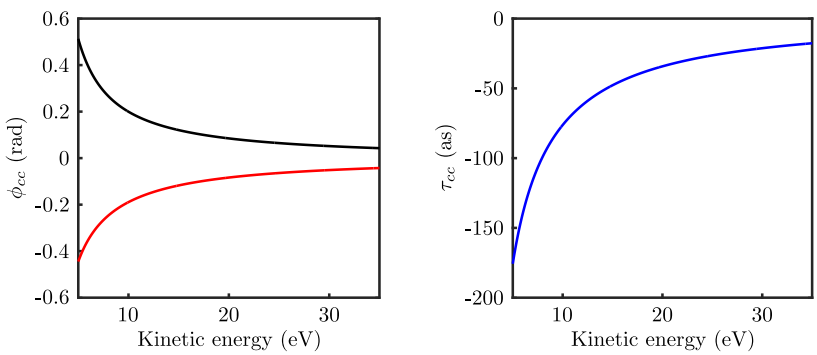

Figure 4.3: Phase and delay induced by a continuum-continuum transition driven by an 800 nm laser field.

Figure 4.3 displays ϕ_{cc} and τ_{cc} calculated following the procedure in [74]. The kinetic energy axis refers, in both cases, to the energy of the intermediate state, i.e. the final state of a one-photon resonant energy conserving transition. The case when the intermediate state has an energy of 1.55 eV higher than that of the final state ($\phi_{cc}(q, q+1)$) results in the black curve in the panel to the right. This case describes the stimulated emission of an IR photon. The red curve shows the situation when the final state has a higher energy than that of the intermediate state ($\phi_{cc}(q, q-1)$), which corresponds to the absorption of an IR photon. As can be seen in the panel to the right, the resulting group delay is negative, independently of energy. Hence the interaction between the electron and the probe field in the presence of the Coulomb potential advances the radially outgoing motion of the electronic wave packet, independently of its initial momentum. This effect is much more pronounced for low energy electrons.

4.3.1 Electron correlation and angular channels

The general description of the two-photon above-threshold ionization given here is only strictly valid within the single active electron approximation. This approximation

builds on the assumption that the electron that is interacting with the light fields moves as an independent particle in a static electric field created by the atomic nucleus and the other electrons. For a theoretical description of the experiments presented in this chapter, a reduction of the electron-electron interactions to a static potential is a drastic oversimplification. Neither one-photon double ionization (Paper **III**) nor autoionization (Paper **V**) can be explained within a mean field single active electron model. To explain these processes, our description must allow for interactions often referred to as electron correlations, that is, direct Coulomb interactions between the electrons in more than the mean field sense.

Electron correlations are included in the theoretical analysis of the experimental data presented in his thesis, by replacing the scattering phase with the phase of the one-photon dipole transition matrix element (see eq. 3.2), calculated using a model that takes into account electronic correlation. The asymptotic approximation is then applied to the final state of these interactions under the assumption that the asymptotic behavior of the scattering state is unaffected by the correlation interactions.

In the discussions in the previous section it was also assumed that available intermediate states of the two-photon transition were non-degenerate, or that one ionization channel strongly dominates the interaction. Figure 4.4 shows a more general situation,

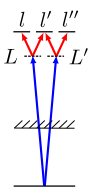

Figure 4.4: Two-photon ionization in multiple angular channels.

which occurs when this is not the case. Such a situation makes the interpretation of the sideband modulation phases in a RABBITT spectrogram more complicated since the phases of the population amplitudes of the final states depend on the angular momentum of the intermediate state. Furthermore, in an angular integrated measurement the final state population densities can not be disentangled.

In a comparison with a theoretical calculation, the strength of each transition to a final state l has to be considered separately and the resulting population amplitudes added. The phase of the sideband can then be calculated by adding up the modulations in the population densities of each final state. For more extensive discussions on this topic see Paper **II** and ref. [90]

4.4 Experiments and results

In a RABBITT spectrogram the phase of a sideband modulation is given by,

$$\tau + \tau_q^{XUV} + \tau_L(q) + \tau_{cc}(q). \tag{4.14}$$

Since we lack the possibility to independently characterize the absolute phase delay of the probe field (τ) and the relative group delay of the APT (τ_q^{XUV}, referenced to $\tau = 0$) these terms can only be eliminated by referencing two sidebands of the

same order, q, to each other. To be able to extract an absolute group delay difference between two processes (a and b), $\tau_L(q)^a - \tau_L(q)^b$, τ also has to be the same for both sideband traces. In other words an experiment has to be designed in such a way that it includes a fixed internal phase reference.

4.4.1 Comparing ionization form subshells of argon

The experiment described in Paper **I** follows up on work published by Klünder et al. in 2011 [17]. As [17] in photoelectrons from ionization of the $3s$ and $3p$ subshells of argon were measured at the same time.

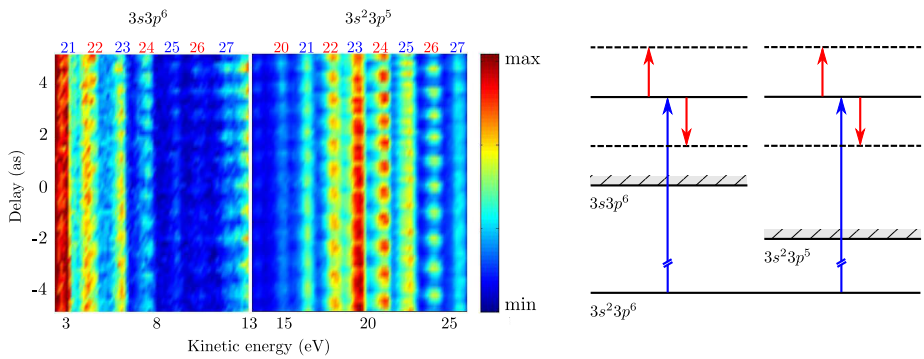

Figure 4.5: Experimental principle: Left panel, RABBITT spectrogram from photo ionization of argon. The signal in the low energy part of the spectrogram (2-13 eV) originating from ionization of the $3s$ subshell has been enhanced for the sake of visibility. The signal in the high energy part of the spectrum originates from ionization of the $3p$ subshell. Right panel, schematic energy level diagram of the two processes involved.

Figure 4.5 describes the principle of the experiment. The difference in ionization potential is just 13.4 eV. As a consequence, the bandwidth of the harmonic radiation had to be limited to four harmonic orders, 21-27 (32.6-41.9 eV), in order to avoid an overlap in kinetic energy between photoelectrons originating from the two different subshells. This was achieved by passing an APT generated in argon through a 0.2 μm thick chromium foil. In order to protect the chromium foil from IR laser radiation, an aluminum foil of the same thickness was also inserted. The combined attenuation of the two foils in combination with the low ionization cross section of the $3s$ subshell resulted in a signal level that required long acquisition times. The experiment therefore greatly benefited from the active stabilization of the interferometer described in Section 3.4.1.

The difference in photoemission delay between the subshells was estimated for sidebands 22-26 (marked with red labels in Fig. 4.5) by taking the difference between the sideband phases extracted from the spectrogram and correcting for τ_{cc}. The agreement with theoretical calculations based on the RPAE (Random Phase Approximation with Exchange) method [69, 91] is reasonable for sidebands 22 and 24, but not for sideband 26. Close to photon energies of 40 eV, the cross section of the process $3s \rightarrow \epsilon p$ goes through a minimum induced by electron correlation between the $3s$ and $3p$ shells. The calculation suggests that this effect is coupled to a rapid phase variation of the transition matrix element, which is not completely reflected in the measurement data.

4.4.2 Comparing ionization from valence shells of noble gas atoms

Paper **II** describes an experiment where photoemission delays from the outer valence shells of argon, neon and helium were referenced to each other. An essential component in this experiment was the use of the actively stabilized interferometer described in Section 3.4.1. This experimental setup allowed us to reproducibly scan the same range of probe pulse delays while recording RABBITT spectrograms using different target gases. Therefore, as the parameters of the high-order harmonic generation were kept constant, the sideband oscillation phase difference between those spectrograms could be directly attributed to a difference in photoemission delay among the target atoms. The harmonic light that was used to ionize the target gas was generated in argon gas and passed through an aluminum foil of 0.2 μm thickness.

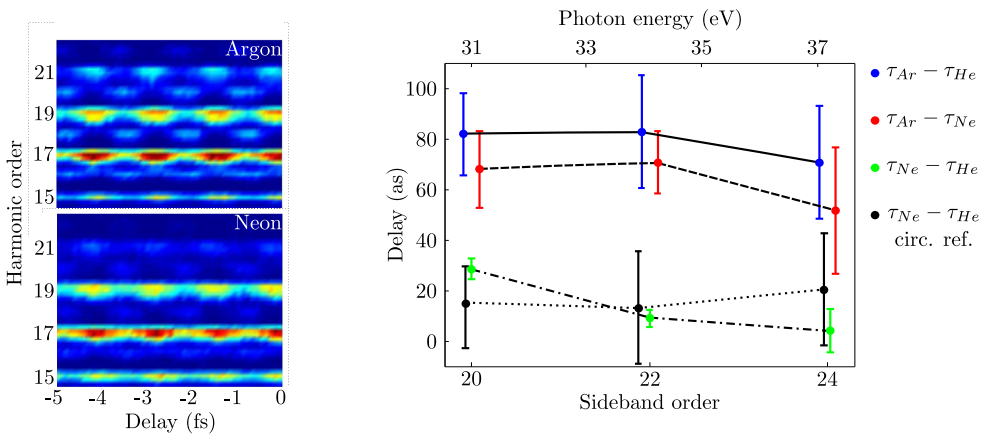

Figure 4.6: Illustration of the experimental procedure (left panel) and experimental results (right panel). The data points in the left panel are shifted in energy with respect to each other only for the sake of visibility.

The experimental procedure is exemplified in the left panel of Fig. 4.6, which shows two (cropped) spectrograms that were recorded as a part of the same data set using argon and neon as a target gas, respectively. Both spectrograms span the same probe pulse delay scale. Therefore the sideband delays extracted from the first spectrogram can be directly subtracted from the corresponding delays from the second spectrogram. The graph to the right shows measurements for three pairs of target gases.

Since the interferometer had a tendency to slowly drift off its temporal reference point, each pair of target gases had to be measured in alternating series, such that the drift could be interpolated from two consecutive measurements on the same target gas. The error bars in Fig. 4.6 represent the standard deviation calculated from a series of 9 such alternating measurements. To check the validity of this measurement procedure $\tau_{Ne} - \tau_{He}$ was also calculated by subtracting the measured values of $\tau_{Ar} - \tau_{Ne}$ from $\tau_{Ar} - \tau_{He}$. The result, which is displayed with black markers, matches the measured values within the precision of the experiment.

In a comparison with theoretical calculations based on both the RPAE and MCHF (Multi-Configural Hartree-Fock) [70] methods, the agreement between theory and experiment is by far the best for the quantity $\tau_{Ne} - \tau_{He}$. The disagreement between

the calculations and the experimental results involving argon is attributed to the theoretical difficulty of including the inter-shell correlation effects between the valence shells.

A similar experiment, presented in refs. [92, 93], used the attosecond streaking technique [94]. As they were detecting photoelectrons and ions in coincidence, two target gases could be measured simultaneously by injecting a mixture of them in the detector chamber. From this data they then reconstructed two spectrograms, one for each target gas, from the same probe pulse delay scan. Their results for $\tau_{Ar} - \tau_{Ne}$ also significantly deviate from theoretical calculations in the photon energy region covered in our experiment. They do however find evidence of sharp variations in the photoemission delay predicted by the argon MCHF calculations. Those variations can be attributed to a series of doubly excited state resonances.

4.4.3 Comparing double and single ionization from xenon

Electron interactions following absorption of a high energy photon might lead to the ejection of two electrons, given that the double ejection is energetically allowed. This process is called single photon double ionization. Paper **III** describes an experiment where the photoemission delay of single photon double ionization in xenon is referenced to the delay in the emission of a single electron from the same atomic species.

To be able to distinguish the double from single ionization events, the photoelectrons were detected in coincidence. The electron TOF was logged separately for each laser shot under conditions where the count rate was much less than one detector impact per shot. With a certain statistical uncertainty, a double impact can then be assigned to one double ionization event. In the left upper panel of Fig. 4.7 this data is presented in a two-dimensional histogram, or coincidence map. Each count in the histogram represents an electron pair. The energy of the least energetic electron is given on the horizontal axis and the sum energy of the pair on the vertical axis.

In order to obtain a ratio between the double to single ionization rates that would not induce a high fraction of false coincidences, the bandwidth of the harmonic light was restricted to four harmonic orders, (21-27) with a photon energy in the vicinity of the double ionization threshold of xenon (33.1 eV). This was achieved by filtering an APT generated in argon through a combination of chromium and aluminum foils. The horizontal stripes in the map each correspond to a final state of the Xe^{2+} ion that has been reached via an excitation by a photon of a given harmonic order. The populated spin-orbit levels all belong to a configuration with two holes in the $5p$ valence shell.

The continuous stripes indicate that the ionized electrons share the excess energy in a non-predetermined fashion, which is a result of the direct ionization mechanisms shake-off and knock-out.

The shake-off mechanism is often described within the sudden approximation [95]. A fast escape of the photoelectron is equivalent to a sudden removal of one electron from its orbital. However, when the remaining occupied atomic orbitals are projected onto the ionic states, there is a possibility that they will overlap with the continuum states of the ion. In that case there is a finite probability that the relaxation process will result in the emission of a second electron. The knock-out mechanism can rather be described as a direct collision between the photoelectron and a secondary electron. A Coulomb interaction between the escaping energetic photoelectron and a secondary electron transfers enough energy to the latter for both of them to escape.

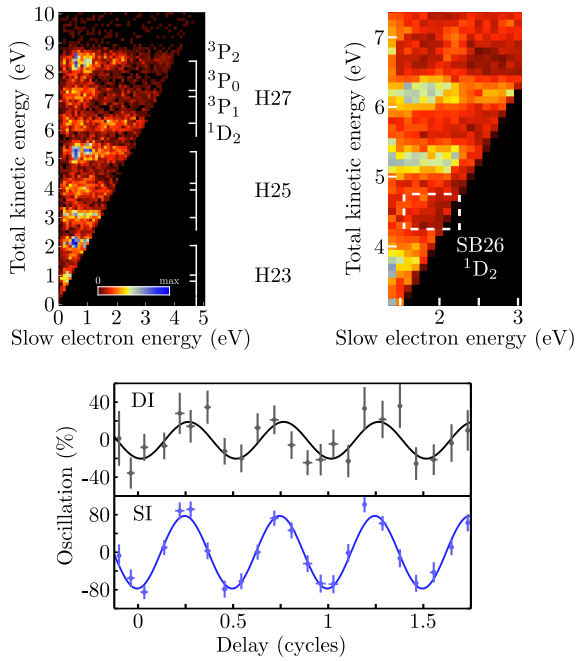

Figure 4.7: Single photon double ionization of xenon. Upper left panel, coincidence map recorded with XUV only. Upper right panel, coincidence map recorded with XUV and IR. Lower panel, comparison between sideband oscillations in the single and double ionization spectra.

The secondary electron is thus knocked out. Both processes lead to a continuous energy sharing between the electrons.

The sharp structures on top of the continuous stripes are signatures of bound excited states of the Xe^+ ion involved in the emission of the secondary electron, i.e. autoionizing states. The secondary electron then has a fixed kinetic energy, corresponding to the difference in energy between the excited state of the singly charged ion and the final state of the doubly charged ion. Since an intermediate state is involved, these ionization mechanisms are termed indirect.

The right upper panel in Fig. 4.7 shows part of a coincidence map recorded with the probe pulse overlapping the XUV pulse train. The presence of the probe field transfers some of the counts from the main lines into two electron sidebands. To show an example of the data analysis from the probe pulse delay scans, we focus on the area enclosed by the white dashed rectangle. This area could be uniquely identified as belonging to sideband 26 and associated with the $^1D_2$ state of the Xe^{2+} ion. The oscillation of the signal within this area could also be clearly discriminated from noise. The lower panel in Fig. 4.7 shows the variation of the signal integrated over the rectangular area as a function of probe pulse delay (DI), together a fitted sinusoidal curve. The same analysis was carried out with the single ionization data (SI), which was recorded simultaneously, for the corresponding sideband.

The shift between the two fitted curves provides an estimate of the single to double ionization two photon delay of 55±61 as. Correcting for the effect of the continuum-

continuum transition, the resulting difference in photoemission delay is 480 as, assuming that shake-off is the dominant process. If knock-out is the main ejection mechanism, the corresponding value is 535 as. These values agree well with theoretical calculations based on RPAE.

4.4.4 Measuring the phase variation across a Fano resonance

When approaching the ionization threshold of an inner atomic shell from below, the photoionization cross section passes through a series of sharp variations (see e.g [96]). These increasingly dense sharp features correlate in energy with bound atomic states in the Rydberg series converging to the inner shell ionization threshold. These phenomena can be explained by configuration interaction or equivalently channel coupling via electron correlations.

Due to the interactions between electrons, an atomic state cannot be fully represented by one configuration of single independent electron states. In the configuration interaction picture, individual configurations are instead treated as part of a basis set. Diagonalizing the atomic Hamiltonian leads to a mixing of configurations, i.e the atomic eigenstates are expressed as superpositions of individual configurations. The mixing is a consequence of the fact that the Hamiltonian term representing the Coulomb interactions between the electrons is non-diagonal in the single configuration basis.

Given that it is energetically allowed, an interaction between a fully bound excited state configuration and a configuration that includes an electron in a continuum state leads to autoionization. This phenomenon can also be described as a relaxation process, where an atom in a excited state decays via the ejection of an electron. In a famous paper from 1961, U. Fano showed that the interference between an ionizing transition via an autoionizing state and a direct transition to a single electron continuum state leads to sharp asymmetric variations in the ionization cross section [97].

Paper **V** investigated the phase of the dipole transition amplitude resulting from such interference between ionization channels. More specifically we used a wavelength tunable APT generated in argon gas to map out the phase variation across the Fano-resonance induced by the $3s^1 3p^6 4p$ excited state configuration in argon. The left hand panel in Fig. 4.8 shows a schematic energy level diagram containing the relevant states and transitions. Harmonic 17 of 800 nm has a photon energy ($\sim$26.4 eV) that closely matches the transition energy needed to excite the resonance. The bound excited state decays via configuration interaction (V) to the s and d continua with an ionic core state in the $3s^2 3p^5$ configuration. Interference between this channel and the direct transition channel induces a local variation in the phase of the total transition amplitude, which then in turn affects the phase of sidebands 16 and 18 in an interferometric measurement.

While tuning the central frequency of harmonic 17 across the resonance, which was achieved by shifting the central frequency of the driving laser pulse (see Section 2.2), it could not be guaranteed that the group delay or group delay dispersion of the attosecond pulses would remain constant. The analysis of the spectrograms could, therefore, not be conducted by simply referencing them to each other. However, assuming that the phase of the transition amplitudes associated with the other harmonic orders only varies marginally within the tuned energy range, it was possible to use

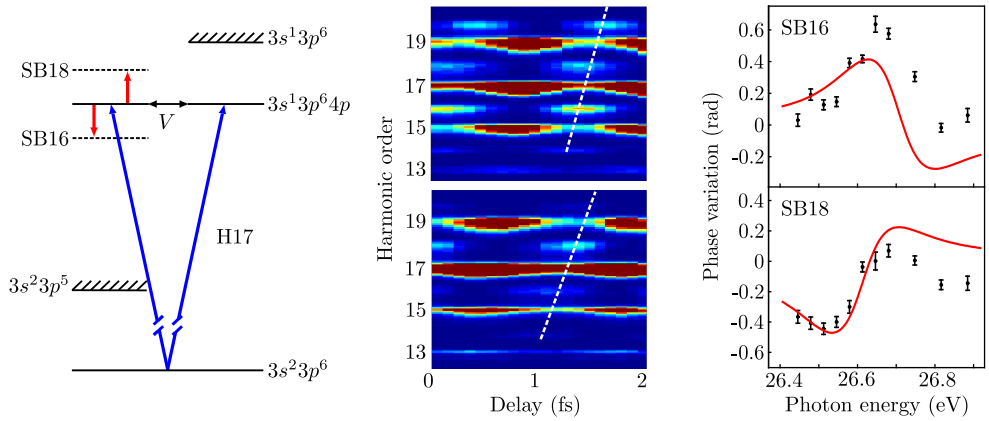

Figure 4.8: Right, schematic energy level diagram and transitions relevant for the experiment. Middle, illustration of the analysis strategy used to obtain a fixed phase reference. The color scale in the spectrograms have been saturated in order to make the weak sidebands visible. Left Experimental results and comparison with theoretical calculations.

the sidebands that are not affected by the resonance as an internal reference. Since the APT is expected to have a linear chirp, i.e the attochirp, a deviation of sidebands 18 and 16 from a straight line connecting the other sideband maxima is attributed to the ionizing transition involving harmonic 17. The middle panel of Fig. 4.8 illustrates this procedure for two spectrograms recorded with harmonic 17 on the far red side of the resonance (lower) and close to the center (upper). The result from this analysis is displayed in the rightmost panel. The graph shows the phase deviation of sidebands 18 and 16 from the fitted line as a function of the photon energy of harmonic 17. It clearly does not map out a π phase variation with opposite signs for sideband 16 and 18 respectively, as expected in the most simple situation where one bound state channel interacts with one continuum channel.

There are three main reasons for this unexpected behavior. Firstly, as mentioned previously there are two interacting continuum channels (s and d) in the single photon transition. As a consequence, the two photon matrix element, where the autoionizing state acts as an intermediate state, must be expressed as a coherent sum of two contributions, which significantly smoothens and flattens its phase variation. Secondly, the spectral width of the harmonics are comparable to the width of the resonance, why analyzing the sideband phase after having integrated over its bandwidth has an averaging effect that further smoothens and broadens the actual phase variation. This effect is further reinforced by the fact that the probing pulse has a finite duration and thus a certain bandwidth. Lastly, the asymmetry between the variation of sidebands 16 and 18 can be attributed to the blue shift of the harmonics due to a partly ionized generation medium. This results in a situation where two probe photons do not exactly match the energy gap between the harmonic lines. When combined with an energy-dependent phase variation across the bandwidth of the harmonic, this effect creates an asymmetry between the quantum pathways associated with absorption and emission of a probe field photon.

The experimental results match well with theoretical calculations accounting for

all the mentioned effects. The red curves in Fig. 4.8 were obtained from calculations of the two-photon matrix elements in combination with a model of the RABBITT method which accounts for the finite duration of both the harmonic pulses and the probe pulse [98].

Chapter 5

Summary and Outlook

5.1 Summary

This thesis presents results from a series of experiments that applied photoelectron interferometry to the study of photoemission delays in various atomic systems and for different emission mechanisms.

In the study presented in Paper **I**, the relative group delay between electrons emitted from the $3s$ and $3p$ shells of Argon was measured. Close to a photon energy of 40 eV the $3s$ ionization cross section goes through a minima induced by inter-shell correlation, which is also expected to have a strong effect on the photoemission delay. This experimental work stimulated a number of theoretical studies investigating this effect as well as the influence of doubly excited states [69, 70, 73].

In Paper **II** photoemission delays of the outer valence shells of argon, neon and helium were compared. The interferometric method was extended to allow photoemission delays from different atoms to be referenced to each other. The most relevant reference system is the helium atom as its simple two-electron structure allows for highly accurate theoretical calculations. Combining these relative measurements with calculations makes it possible to retrieve accurate estimates of photoemission time delays on an absolute rather than relative time scale.

Combining photoelectron interferometry with electron coincidence spectroscopy enabled a novel type of experiment for investigating the delay in photoemission associated with a two electron continuum wave packet (Paper **III**). The continuum electron pairs were created from double photoionization of xenon. The experiment demonstrated that a coherent manipulation of the two-electron wave packet by an IR pulse gives rise to an interferometric signal. Furthermore, since the emission of two electrons is a result of electronic correlations, this type of experiments could generate vital input for theoretical models going beyond the single active electron approach.

In the work presented in Paper **V** the aim was not to measure the group delay of a continuum wave packet but rather the phase of a two-photon dipole transition in the vicinity of a resonance. This was accomplished by tuning the photon energy of one harmonic across the range of a resonance induced by a autoionizing state in argon. This approach allowed a significant phase distortion to be mapped out, together with the cross section profile. This experiment demonstrates a new way to characterize

the interaction between a bound state and an ionization continuum, a method that goes beyond measuring the cross section profile. For example, in this particular case, the phase of the two-photon transition matrix element proved to be influenced by the existence of two interacting continuum channels.

The RABBITT technique was also applied in the work presented in Paper **IV**, where we study the synchronization between an APT and the laser pulse giving rise to it. Here, a temporal walk-off depending on the density of the generation gas medium was observed. The results show that the macroscopic response of the generation medium influences the timing of the APT in the sub-cycle of the driving field. These findings are complementary to previous studies that focused on aspects of the atomic response.

In Paper **VI** it is demonstrated that low order harmonics generated from a gas target can enhance the high order harmonic generation from a second gas target. Paper **VII** presents plans for seeding a free-electron laser with harmonics from a gas target placed in-line with the electron beam. My contribution to these two publications consisted in running a computer code for simulation of gas generated harmonics [99]. Finally, Paper **VIII** describes the design and tests of an electron spectrometer that allows for a full reconstruction of the photoelectron momenta.

5.2 Outlook

The studies on photoemission delays presented in this thesis were conducted with a photoelectron spectrometer that integrates over the emission angle of the electrons. An angular resolved detection technique is to prefer in cases where the ionizing transition is not limited to one single or dominant angular channel, since the group delay of the wave packet then depends on the emission angle.

An interesting candidate for a study with angular resolved detection is ionization from the valence shell of argon in an energy region close to the $3p \rightarrow \epsilon d$ Cooper minima. Here the photoemission delay is expected to vary strongly with emission angle due to the mixing of s and d partial waves [100, 101]. The Velocity Map Imaging Spectrometer (VMIS) is one type of instrument that provides angular resolved photoelectron spectra and which has been widely used in combination with HHG sources. The spectrometer presented in Paper **VIII** is partly based on this technique. More recently, reaction microscopes have enabled angular resolved attosecond experiments utilizing HHG sources. These instruments enable a full reconstruction of the momenta of the charged particles resulting from a ionization event via coincident position sensitive detection of both electrons and ions. In ref. [102] a reaction microscope was used in combination with the RABBITT technique to measure the delay in photoemission from helium. The result shows that there is a significant angular anisotropy in the group delay of the wave packet created by a two-color two-photon transition, due to the presence of two degenerate final states with different angular momenta.

Coincidence electron spectroscopy is based on the requirement that each laser shot should result in at most one ionization event. Conducting experiments that demand coincident electron detection using a 1 kHz laser system is therefore very time consuming. Long data acquisition times are a challenge for the type of experiments presented in this thesis, since long acquisition times mean that the interferometric stability required to measure time shifts of tenths of attoseconds has to be maintained

during long periods of time. Hopefully, however, an implementation of the plans for the new interferometric setup presented in Section 3.4.1 will make time-consuming experiments less of a challenge and more of a routine.

In a slightly longer perspective, experiments that build on single particle counting will preferably be conducted using lasers with a higher repetition rate than 1 kHz. Recently a 200 kHz repetition rate laser system was installed in the Lund High-Power Laser Facility. The amplifier chain is based on Optical Parametric Chirped Pulse Amplification (OPCPA) and is specified to deliver 8 fs pulses with an energy of 17 μJ and a central wavelength of 850 nm. Current work is progressing to construct a HHG source driven by this laser system [22] in combination with an optical interferometric setup and a reaction microscope end-station.

As was demonstrated in Paper **V**, frequency tunable attosecond pulses provide the means to investigate the narrow bandwidth phase distortion of a transition matrix element induced by an ionizing resonance. If the bandwidth of the harmonic driving a resonant transition is wide enough to cover the full bandwidth of the resonance and the electron spectrometer resolution is good enough to resolve it, the spectral phase profile of a two-photon resonant transition can be retrieved from one single spectrogram. This was recently shown by a research group from the University of Paris-Saclay. In a joint experimental effort this method is now being applied to the study of other resonances. One interesting example is the experiment theoretically modeled in [103] that is concerned with a series of autoionizing doubly excited states in helium. It is also of interest to revisit the previously examined argon resonance using this method and compare the results with those in Paper **V**.

Another phenomenon which also involves autoionization is Auger decay. In this process, which follows after the ionization of an inner shell or core level electron, the excited ion decays via a reconfiguration and ejection of a second electron. Using a single attosecond pulse and a few cycle IR pulse, Drescher et al. conducted a pump-probe experiment that temporally resolved the decay of an $M_{4,5}$-shell ($3p_{3/2,5/2}$) vacancy in krypton [104]. During the last year of this thesis work we have worked on measuring the decay of an $N_{4,5}$-shell ($4d_{3/2,5/2}$) vacancy in xenon using the interferometric method. Inner shell electron spectroscopy requires higher photon energies than were used in the previously presented spectroscopic studies. To ionize the xenon $4d$-shell we use a broadband frequency-comb of harmonics generated in neon, spanning a photon energy range between 75 and 105 eV. Such a broad band excitation means that the photoelectrons and Auger electrons overlap in energy. As a result, coincident detection of the emitted electron pairs is required to disentangle the spectral features.

Figure 5.1 shows a spectra recorded with XUV radiation only. A simulation of the coincidence spectra based on spectroscopic data [105] provides an identification of all the spectral features. The most intense peaks, which do not overlap with any other features in the spectra, can be assigned to the $N_{4,5}O_1O_1$ Auger processes. Here the $4d_{3/2,5/2}$ vacancy decays to a doubly ionized configuration of two vacancies in the $5s$-shell (O_1). The energy of these Auger electrons is low, around 10 eV, so the fastest electron of the pair can be unambiguously identified as the photoelectron over an energy range of more than 30 eV. Each peak in the two rows along the fast electron energy axis can therefore be associated with a photon energy of certain a harmonic order, as exemplified in the figure. The analysis of the two-color two-photon (IR and XUV) ionization data has for these reasons focused on the $N_{4,5}O_1O_1$ process. Unfortunately, this experiment has proven to be very challenging under the current

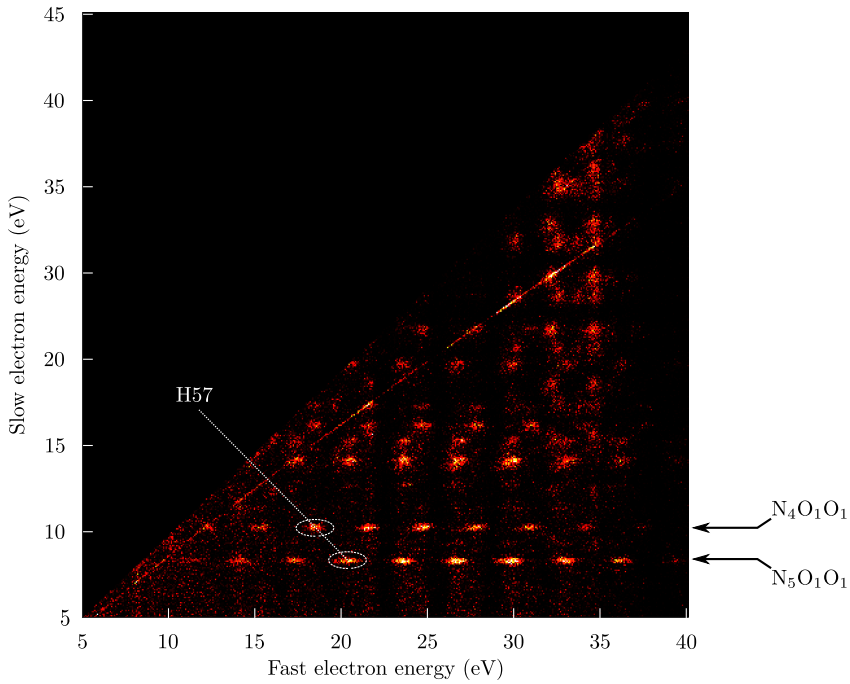

Figure 5.1: Coincidence spectrum of xenon $N_{4,5}OO$ Auger decay.

conditions. Each single spectrum in the spectrogram requires almost an hour of acquisition time. Keeping the probe pulse delay and the laser system stable during a long enough period of time to record a full data set still remains a challenge and requires more work.

With the methods presented in this thesis, phase shifts of electronic matter waves can be accessed in the spectral domain. These methods, which have been developed within the attosecond science community during the last decade, thus give access to a new physical observable. Undoubtedly this will, via the interplay between experimental observations and their theoretical interpretation, generate a better understanding of dynamics in complex electron systems. While this thesis deals with atomic systems exclusively, there is no fundamental limitation that prevents more complex systems to be investigated. Photoelectron interferometry has for example been demonstrated to be applicable in condensed matter physics, where it was used to resolve the dynamics in photoemission from a surface.

Comments on the papers

I **Photoemission-time-delay measurements and calculations close to the 3s-ionization-cross-section minimum in Ar**
In this paper, we present new measurements of the relative photoionization time delays between electrons originating from the 3s and 3p subshells in argon, together with theoretical calculations. I took part in the experiments.

II **Measurements of relative photoemission time delays in noble gas atoms**
The photoemission time delays for valence electrons from argon, neon and helium are measured and referenced to each-other. The results are compared to theoretical calculations. I conducted the experiments together with another student and contributed to the preparation of the manuscript via discussions and by feedback.

III **Double ionization probed on the attosecond timescale**
The electron emission time in one-photon double ionization of xenon is measured and referenced to the single ionization time delay. The results are interpreted and compared to theoretical calculations. I took part in the preparations and conduction of the experiment.

IV **Attosecond pulse walk-off in high-order harmonic generation**
A temporal walk-off of attosecond pulses in High-order harmonic generation is measured and explained using an on-axis phase matching model. I had a leading role in conducting the experiments, analyzed the data, developed the ideas for interpreting the results, did the simulations presented in the paper and wrote a major part of the manuscript.

V **Spectral phase measurement of a Fano resonance using tunable attosecond pulses**
Using a tunable attosecond pulse-train, we measure the phase variation of the photoionization probability amplitude as a function of excitation energy in the proximity of the $3s^2 3p^6 \rightarrow 3s^1 3p^6 4p$ autoionizing resonance in argon. The results are compared with theoretical calculations. I contributed largely to the construction of the experimental setup and preformed the experiments together with two other authors. I also contributed to the data analysis, preparation of figures for the manuscript and the theoretical interpretation through discussions.

VI **Efficient high-order harmonic generation boosted by below-threshold harmonics**
This paper presents an experiment where high-order harmonics are generated in a dual gas cell setup. The results show that the low-order harmonics, created in the first cell, boosts high-order harmonic generation in the second cell. I contributed to this work by performing numerical simulations that supported the argument that low-order harmonics were responsible for the boosting effect.

VII **Seeded Coherent Harmonic Generation with in-line Gas Target**
This conference proceeding presents a plan for seeding the test-FEL at MAX-lab with harmonics of a Ti:sapphire laser beam, generated in a gas target. The presented scheme features a new approach, to bring the gas target in-line with the electron beam. I conducted numerical simulations of harmonic generation in these conditions, whose results were fed to a different code for simulation of FEL.

VIII **Multi-purpose two- and three-dimensional momentum imaging of charged particles for attosecond experiments at 1 kHz repetition rate**
This paper presents the design and tests of a two-sided momentum imaging spectrometer. The test results demonstrates the performance of the spectrometer in two different modes of operation, that allows for either a 2D or 3D reconstruction of charged particle momenta. I contributed by operating the HHG-source used in one of the tests.

Acknowledgments

I have learned many things during my years as a PhD student at the Atomic Physics division in Lund, both about physics and about the world of science. I have also learned many things about myself. For all this knowledge and for all the experiences I had during this time I am truly grateful.

First of all, I would like to thank my supervisor Anne L'Huillier for giving me this opportunity and for guiding me through my studies. She have encouraged me to go my own way and kept me going even when things were hard. I would also like thank my co-supervisors, Johan Mauritsson, for his helpful creative ideas and for sharing my interest for teaching and Mathieu Gisselbrecht, for teaching me about both physics and life, and for always knowing how to motivate me.

I would also like express my gratitude to all present and former members of the Lund Attosecond Physics group and other people that I had the privilege to work with during these years.

A special thanks I would like to direct to the crew of Attolab: Cord Arnold, Diego Guénot, Marija Kotur, Esben Witting Larsen, Samuel Bengtsson, Marcus Isinger, Anne Harth, Neven Ibrakovič, Maïte Louisy, Jana Preclíková and Stefan Plogmaker. With you I have spent many hours, during both days and nights, conducting challenging experiments, having creative discussions and not to forget, having fun. I would also like to direct a special thanks to Erik Månsson whose hard work was essential for this thesis.

I would also like to thank the other members of the Attosecond Physics group: Per Johnsson, Miguel Miranda, Eleonora Lorek, Stefanos Carlström, Linnea Rading, Sylvain Maclot, Bastian Manschwetus, Hampus Wikmark, Filippo Campi, Jan Lahl, Christoph Heyl, Piotr Rudawski, Fernando Brizuela, Chen Guo, Hélène Coudert-Alteirac, Arthur Losquin, Yu-Chen Cheng, Byunghoon Kim and Thomas Fordell. You have all contributed to a creative and pleasant working environment and always been there if help was needed. Together we have had a great deal of fun, also after working hours.

I would also like to thank Marcus Dahlstöm, for teaching me about free electron wave packets and Kathrin Klünder, for her work on the new interferometric setup.

During my time in Lund I had the opportunity to be part of a number of collaborations. I thus would like to acknowledge and thank: Katalin Varjú and Emeric Balogh, for interesting discussions on phase-matching of high-order harmonics and for their contributions to our paper. Raimund Feifel and Richard Squibb, for lending us their electron spectrometer and for a fruitful collaboration. The group at MAX-lab which joined us in a bold project with a tight time frame. Thank you Sverker Werin,

Francesca Curbis, Filip Lindau and Erik Mansten. I also would like to acknowledge Alfred Maquet, Richard Taïeb, Anatoli Kheifets, Eva Lindroth, Thomas Carette, Fernando Martín, Luca Argenti and Álvaro Jiménez-Galán for the work they have done in providing the theory for this thesis work.

I am also grateful for the positive working environment that the Atomic Physics division offers, which was an important reason to why I applied for a position there. Thank you Claes-Göran Wahlström for leading the division and Anne Petersson Jungbeck, Jakob Testad and Åke Johansson for making sure that the every day work the division runs smoothly.

Finally, I would like to express my deep gratitude to my family. Without your help and patience this thesis would not have been completed.

References

1. M. Ferray, A. L'Huillier, X. F. Li, L. A. Lompre, G. Mainfray and C. Manus. *Multiple-harmonic conversion of 1064 nm radiation in rare gases.* J. Phys. B **21**, L31 (1988).

2. A. McPherson, G. Gibson, H. Jara, U. Johann, T. S. Luk, I. A. McIntyre, K. Boyer and C. K. Rhodes. *Studies of multiphoton production of vacuum-ultraviolet radiation in the rare gases.* J. Opt. Soc. Am. B **4**, 595–601 (1987).

3. G. Farkas and C. Tóth. *Proposal for attosecond light pulse generation using laser induced multiple-harmonic conversion processes in rare gases.* Phys. Lett. A **168**, 447 (1992).

4. P. M. Paul, E. S. Toma, P. Breger, G. Mullot, F. Augé, Ph. Balcou, H. G. Muller and P. Agostini. *Observation of a train of attosecond pulses from high harmonic generation.* Science **292**, 1689 (2001).

5. S. R. Leone, C. W. McCurdy, J. Burgdorfer, L. S. Cederbaum, Z. Chang, N. Dudovich, J. Feist, C. H. Greene, M. Ivanov, R. Kienberger, U. Keller, M. F. Kling, Z.-H. Loh, T. Pfeifer, A. N. Pfeiffer, R. Santra, K. Schafer, A. Stolow, U. Thumm and M. J. J. Vrakking. *What will it take to observe processes in 'real time'?* Nat. Photonics **8**, 162–166 (2014).

6. M. Chini, K. Zhao and Z. Chang. *The generation, characterization and applications of broadband isolated attosecond pulses.* Nat. Photonics **8**, 178–186 (2014).

7. K. T. Kim, D. M. Villeneuve and P. B. Corkum. *Manipulating quantum paths for novel attosecond measurement methods.* Nat. Photonics **8**, 187–194 (2014).

8. F. Lepine, M. Y. Ivanov and M. J. J. Vrakking. *Attosecond molecular dynamics: fact or fiction?* Nat. Photonics **8**, 195–204 (2014).

9. F. Krausz and M. I. Stockman. *Attosecond metrology: from electron capture to future signal processing.* Nat. Photonics **8**, 205–213 (2014).

10. K. Zhao, Q. Zhang, M. Chini, Y. Wu, X. Wang and Z. Chang. *Tailoring a 67 attosecond pulse through advantageous phase-mismatch.* Opt. Lett. **37**, 3891–3893 (2012).

11. P. Johnsson, J. Mauritsson, T. Remetter, A. L'Huillier and K. J. Schafer. *Attosecond Control of Ionization by Wave-Packet Interference.* Phys. Rev. Lett. **99**, 233001 (2007).

12. Ch. Neidel, J. Klei, C.-H. Yang, A. Rouzée, M. J. J. Vrakking, K. Klünder, M. Miranda, C. L. Arnold, T. Fordell, A. L'Huillier, M. Gisselbrecht, P. Johnsson, M. P. Dinh, E. Suraud, P.-G. Reinhard, V. Despré, M. A. L. Marques and F. Lépine. *Probing Time-Dependent Molecular Dipoles on the Attosecond Time Scale.* Phys. Rev. Lett. **111**, 033001 (2013).

13. F. Calegari, D. Ayuso, A. Trabattoni, L. Belshaw, S. De Camillis, S. Anumula, F. Frassetto, L. Poletto, A. Palacios, P. Decleva, J. B. Greenwood, F. MartÃn and M. Nisoli. *Ultrafast electron dynamics in phenylalanine initiated by attosecond pulses.* Science **346**, 336–339 (2014).

14. V. Véniard, R. Taïeb and A. Maquet. *Phase dependence of (N+1) - color (N>1) ir-uv photoionization of atoms with higher harmonics.* Phys. Rev. A **54**, 721 (1996).

15. H. G. Muller. *Reconstruction of attosecond harmonic beating by interference of two-photon transitions.* Appl. Phys. B **74**, 17 (2002).

16. C. Iaconis and I. A. Walmsley. *Spectral phase interferometry for direct electric field reconstruction of ultrashort optical pulses.* Opt. Lett. **23**, 792 (1998).

17. K. Klünder, J. M. Dahlström, M. Gisselbrecht, T. Fordell, M. Swoboda, D. Guénot, P. Johnsson, J. Caillat, J. Mauritsson, A. Maquet, R. Taïeb and A. L'Huillier. *Probing Single-Photon Ionization on the Attosecond Time Scale.* Phys. Rev. Lett. **106**, 143002 (2011).

18. P. A. Franken, A. E. Hill, C. W. Peters and G. Weinreich. *Generation of optical harmonics.* Phys. Rev. Lett. **7**, 118 (1961).

19. T. H. Maiman. *Stimulated optical radiation in Ruby.* Nature **187**, 493 (1960).

20. M. Krebs, S. Hädrich, S. Demmler, J. Rothhardt, A. Zaïr, L. Chipperfield, J. Limpert and A. Tünnermann. *Towards isolated attosecond pulses at megahertz repetition rates.* Nat. Photonics **7**, 555–559 (2013).

21. E. Lorek, E. W. Larsen, C. M. Heyl, S. Carlström, D. Paleĉek, D. Zigmantas and J. Mauritsson. *High-order harmonic generation using a high-repetition-rate turnkey laser.* Rev. Sci. **85**, 123106 (2014).

22. P. Rudawski, A. Harth, C. Guo, E. Lorek, M. Miranda, C. M. Heyl, E. W. Larsen, J. Ahrens, O. Prochnow, T. Binhammer, U. Morgner, J. Mauritsson, A. L'Huillier and C. L. Arnold. *Carrier-envelope phase dependent high-order harmonic generation with a high-repetition rate OPCPA-system.* Eur. Phys. J. D **69**, 70 (2015).

23. T. Brabec, Ch. Spielmann, P. F. Curley and F. Krausz. *Kerr lens mode locking.* Opt. Lett. **17**, 1292–1294 (1992).

24. D. E. Spence, P. N. Kean and W. Sibbett. *60-fsec pulse generation from a self-mode-locked Ti:sapphire laser.* Opt. Lett. **16**, 42 (1991).

25. D. Strickland and G. Mourou. *Compression of amplified chirped optical pulses.* Opt. Commun. **56**, 219 (1985).

26. S. Backus, C. G. Durfee, M. M. Murnane and H. C. Kapteyn. *High power ultrafast lasers.* Rev. Sci. Instrum. **69**, 1207–1223 (1998).

27. P. F. Moulton. *Spectroscopic and laser characteristics of Ti:Al_2O_3.* J. Opt. Soc. Am. B **3**, 125–133 (1986).

28. A. Stingl, M. Lenzner, Ch. Spielmann, F. Krausz and R. Szipöcs. *Sub-10-fs mirror-dispersion-controlled Ti:sapphire laser.* Opt. Lett. **20**, 602–604 (1995).

29. I. D. Jung, F. X. Kärtner, N. Matuschek, D. H. Sutter, F. Morier-Genoud, G. Zhang, U. Keller, V. Scheuer, M. Tilsch and T. Tschudi. *Self-starting 6.5-fs pulses from a Ti:sapphire laser.* Opt. Lett. **22**, 1009 (1997).

30. U. Morgner, F. X. Kärtner, S. H. Cho, Y. Chen, H. A. Haus, J. G. Fujimoto, E. P. Ippen, V. Scheuer, G. Angelow and T. Tschudi. *Sub-two-cycle pulses from a Kerr-lens mode-locked Ti:sapphire laser.* Opt. Lett. **24**, 411 (1999).

31. G. Cheriaux, P. Rousseau, F. Salin, J. P. Chambaret, Barry Walker and L. F. Dimauro. *Aberration-free stretcher design for ultrashort-pulse amplification.* Opt. Lett. **21**, 414–416 (1996).

32. E. Treacy. *Optical pulse compression with diffraction gratings.* IEEE J. Quant. Electron. **5**, 454 – 458 (1969).

33. O. E. Martinez. *Grating and prism compressors in the case of finite beam size.* J. Opt. Soc. Am. B **3**, 929 (1986).

34. P. B. Corkum. *Plasma perspective on strong-field multiphoton ionization.* Phys. Rev. Lett. **71**, 1994 (1993).

35. K. C. Kulander, K. J. Schafer and J. L. Krause. *Dynamics of short-pulse excitation, ionization and harmonic conversion.* In *Super-Intense Laser-Atom Physics.* Plenum Press, New York (1993).

36. M. Lewenstein, Ph. Balcou, M.Yu. Ivanov, A. L'Huillier and P. B. Corkum. *Theory of high-order harmonic generation by low-frequency laser fields.* Phys. Rev. A **49**, 2117 (1994).

37. J. M. Dahlström. *Light-Matter Interaction on the Attosecond Timescale.* PhD thesis Lund University (2011).

38. P. Salières, B. Carré, L. Le Déroff, F. Grasbon, G. G. Paulus, H. Walther, R. Kopold, W. Becker, D. B. Milošević, A. Sanpera and M. Lewenstein. *Feynman's Path-Integral Approach for Intense-Laser-Atom Interactions.* Science **292**, 902 (2001).

39. Ph. Antoine, A. L'Huillier and M. Lewenstein. *Attosecond Pulse Trains Using High-Order Harmonics.* Phys. Rev. Lett. **77**, 1234 (1996).

40. O. Smirnova, M. Spanner and M. Ivanov. *Analytical solutions for strong field-driven atomic and molecular one- and two-electron continua and applications to strong-field problems.* Phys. Rev. A **77**, 033407 (2008).

41. A. L'Huillier, P. Balcou, S. Candel, K. J. Schafer and K. C. Kulander. *Calculations of high-order harmonic-generation processes in xenon at 1064 nm.* Phys. Rev. A **46**, 2778 (1992).

42. C. G. Wahlström, J. Larsson, A. Persson, T. Starczewski, S. Svanberg, P. Salieres, Ph. Balcou and A. L'Huillier. *High-order harmonic generation in rare gases with an intense short-pulse laser.* Phys. Rev. A **48**, 4709 (1993).

43. T. Popmintchev, M.-C. Chen, D. Popmintchev, P. Arpin, S. Brown, S. Ališauskas, G. Andriukaitis, T. Balciunas, O. D. Mücke, A. Pugzlys, A. Baltuska, B. Shim, S. E. Schrauth, A. Gaeta, C. Hernández-Garcia, L. Plaja, A. Becker, A. Jaron-Becker, M. M. Murnane and H. C. Kapteyn. *Bright Coherent Ultrahigh Harmonics in the keV X-ray Regime from Mid-Infrared Femtosecond Lasers.* Science **336**, 1287–1291 (2012).

44. A. D. Shiner, C. Trallero-Herrero, N. Kajumba, H.-C. Bandulet, D. Comtois, F. Légaré, M. Giguère, J-C. Kieffer, P. B. Corkum and D. M. Villeneuve. *Wavelength Scaling of High Harmonic Generation Efficiency.* Phys. Rev. Lett. **103**, 073902 (2009).

45. J. Tate, T. Auguste, H. G. Muller, P. Salieres, P. Agostini and L. F. DiMauro. *Scaling ofWave-Packet Dynamics in an Intense Midinfrared Field.* Phys. Rev. Lett. **98**, 013901 (2007).

46. E. Constant, D. Garzella, P. Breger, E. Mével, Ch. Dorrer, C. Le Blanc, F. Salin and P. Agostini. *Optimizing High Harmonic Generation in Absorbing Gases: Model and Experiment.* Phys. Rev. Lett. **82**, 1668 (1999).

47. S. Kazamias, D. Douillet, F.Weihe, C. Valentin, A. Rousse, S. Sebban, G. Grillon, F. Augé, D. Hulin and Ph. Balcou. *Global Optimization of High Harmonic Generation.* Phys. Rev. Lett. **90**, 193901 (2003).

48. A. L'Huillier, X. F. Li and L. A. Lompré. *Propagation effects in high-order harmonic generation in rare gases.* JOSA B **7**, 527–536 (1990).

49. L. Roos, E. Constant, E. Mevel, Ph. Balcou, D. Descamps, M. B. Gaarde, A. Valette, R. Haroutounian and A. L´Huillier. *Controlling phase-matching of high-order harmonic generation by manipulating the fundamental field.* Phys. Rev. A **60**, 5010 (1999).

50. A. Paul, R. A. Bartels, R. Tobey, H. Green, S. Weiman, I. P. Christov, M. M. Murnane, H. C. Kapteyn and S. Backus. *Quasi-phase-matched generation of coherent extreme-ultraviolet light.* Nature **421**, 51 (2003).

51. M.V. Ammosov, N.B. Delone and V. Krainov. *Tunnel ionization of complex atoms and of atomic ions in an alternating electric field.* Sov. Phys. JETP **64**, 1191 (1986).

52. P. Rudawski, C. M. Heyl, F. Brizuela, J. Schwenke, A. Persson, E. Mansten, R. Rakowski, L. Rading, F. Campi, B. Kim, P. Johnsson and A. L'Huillier. *A high-flux high-order harmonic source.* Rev. Sci. Inst. **84**, – (2013).

53. M. Lewenstein, P. Salières and A. L'Huillier. *Phase of the atomic polarization in high-order harmonic generation.* Phys. Rev. A **52**, 4747 (1995).

54. P. Salières, A. L'Huillier and M. Lewenstein. *Coherence control of high-order harmonics.* Phys. Rev. Lett. **74**, 3776 (1995).

55. Y. Mairesse, A. de Bohan, L. J. Frasinski, H. Merdji, L. C. Dinu, P. Monchicourt, P. Breger, M. Kovacev, T. Auguste, B. Carré, H.G. Muller, P. Agostini and P. Salieres. *Optimization of Attosecond Pulse Generation.* Phys. Rev. Lett. **93**, 163901 (2004).

56. R. López-Martens, K. Varjú, P. Johnsson, J. Mauritsson, Y. Mairesse, P. Salières, M. B. Gaarde, K. J. Schafer, A. Persson, S. Svanberg, C.-G. Wahlström and A. L'Huillier. *Amplitude and phase control of attosecond light pulses.* Phys. Rev. Lett. **94**, 033001 (2005).

57. Z. Chang, A. Rundquist, H. Wang, I. Christov, H. C. Kapteyn and M. M. Murnane. *Temporal phase control of soft-x-ray harmonic emission.* Phys. Rev. A **58**, R30 (1998).

58. K. Varjú, Y. Mairesse, B. Carre, M. B. Gaarde, P. Johnsson, S. Kazamias, R. Lopez-Martens, J. Mauritsson, K. J. Schafer, Ph. Balcou, A. L'Huillier and P. Salières. *Frequency chirp of harmonic and attosecond pulses.* J. Mod. Opt. **52**, 379 (2005).

59. D. G. Lee, J.-H. Kim, K.-H. Hong and C. H. Nam. *Coherent Control of High-Order Harmonics with Chirped Femtosecond Laser Pulses.* Phys. Rev. Lett. **87**, 243902 (2001).

60. J.-H. Kim and C. H. Nam. *Plasma-induced frequency chirp of intense femtosecond lasers and its role in shaping high-order harmonic spectral lines.* Phys. Rev. A **65**, 033801 (2002).

61. T. Ruchon, C. P. Hauri, K. Varjú, E. Mansten, M. Swoboda, R. López-Martens and A. L'Huillier. *Macroscopic effects in attosecond pulse generation.* New. J. Phys. **10 No. 2**, 025027 (2008).

62. S. A. Aseyev, Y. Ni, L. J. Frasinski, H. G. Muller and M. J. J. Vrakking. *Attosecond Angle-Resolved Photoelectron Spectroscopy.* Phys. Rev. Lett. **91**, 223902 (2003).

63. L. C. Dinu, H. G. Muller, S. Kazamias, G. Mullot, F Augé, Ph. Balcou, P. M. Paul, M. Kovačev, P. Breger and P. Agostini. *Measurement of the Subcycle Timing of Attosecond XUV Bursts in High-Harmonic Generation.* Phys. Rev. Lett. **91**, 063901 (2003).

64. Y. Mairesse, A. de Bohan, L. J. Frasinski, H. Merdji, L. C. Dinu, P. Monchicourt, P. Breger, M. Kovačev, R. Taïeb, B. Carré, H. G. Muller, P. Agostini and P. Salières. *Attosecond synchronization of high-harmonic soft X-rays.* Science **302**, 1540 (2003).

65. R. Pazourek, S. Nagele and J. Burgdörfer. *Attosecond chronoscopy of photoemission.* Rev. Mod. Phys. **87**, 765–802 (2015).

66. M. Swoboda, J. M. Dahlström, T. Ruchon, P. Johnsson, J. Mauritsson, A. L'Huillier and K.J. Schafer. *Intensity dependence of laser-assisted attosecond photoionization spectra.* Laser Physics **19**, 1591–1599 (2009).

67. E. S. Toma and H. G. Muller. *Calculation of matrix elements for mixed extreme-ultraviolet-infrared two-photon above-threshold ionization of argon.* J. Phys. B **35**, 3435 (2002).

68. A. S. Kheifets and I. A. Ivanov. *Delay in Atomic Photoionization.* Phys. Rev. Lett. **105**, 233002 (2010).

69. A. S. Kheifets. *Time delay in valence-shell photoionization of noble-gas atoms.* Phys. Rev. A **87**, 063404 (2013).

70. T. Carette, J. M. Dahlström, L. Argenti and E. Lindroth. *Multiconfigurational Hartree-Fock close-coupling ansatz: Application to the argon photoionization cross section and delays.* Phys. Rev. A **87**, 023420 (2013).

71. C. Palatchi, J. M. Dahlström, A. S. Kheifets, I. A. Ivanov, D. M. Canaday, P. Agostini and L. F. DiMauro. *Atomic delay in helium, neon, argon and krypton.* J. Phys. B **47**, 245003 (2014).

72. J. M. Dahlström and E. Lindroth. *Study of attosecond delays using perturbation diagrams and exterior complex scaling.* J. Phys. B **47**, 124012 (2014).

73. M. Magrakvelidze, M. E.-A. Madjet, G. Dixit, M. Ivanov and H. S. Chakraborty. *Attosecond time delay in valence photoionization and photorecombination of argon: A time-dependent local-density-approximation study.* Phys. Rev. A **91**, 063415 (2015).

74. J. M. Dahlström, D. Guénot, K. Klünder, M. Gisselbrecht, J. Mauritsson, A. L'Huillier, A. Maquet and R. Taïeb. *Theory of attosecond delays in laser-assisted photoionization.* Chem. Phys. **414**, 53–64 (2013).

75. Y. Mairesse and F. Quéré. *Frequency-resolved optical gating for complete reconstruction of attosecond bursts.* Phys. Rev. A **71**, 011401(R) (2005).

76. M. Kitzler, N. Milosevic, A. Scrinci and T. Brabec. *Quantum Theory of Attosecond XUV Pulse Measurement by Laser Dressed Photoionization.* Phys. Rev. Lett. **88**, 173904 (2002).

77. P. Kruit and F. H. Read. *Magnetic field paralleliser for 2π electron-spectrometer and electron-image magnifier.* J. Phys. E **16**, 313 (1983).

78. A. M. Rijs, E. H. G. Backus, C. A. de Lange, N. P. C. Westwood and M. H. M. Janssen. *'Magnetic bottle' spectrometer as a versatile tool for laser photoelectron spectroscopy.* J. Electron Spectrosc. **112**, 151 – 162 (2000).

79. C.-Y. Cha, G. Ganteför and W. Eberhardt. *New experimental setup for photoelectron spectroscopy on cluster anions.* Rev. Sci. Instrum. **63**, 5661–5666 (1992).

80. J. H. D. Eland, O. Vieuxmaire, T. Kinugawa, P. Lablanquie, R. I. Hall and F. Penent. *Complete Two-Electron Spectra in Double Photoionization: The Rare Gases Ar, Kr, and Xe.* Phys. Rev. Lett. **90**, 053003 (2003).

81. M. Chini, H. Mashiko, H. Wang, S. Chen, C. Yun, S. Scott, S. Gilbertson and Z. Chang. *Delay control in attosecond pump-probe experiments.* Opt. Express **17**, 21459–21464 (2009).

82. M. Sabbar, S. Heuser, R. Boge, M. Lucchini, L. Gallmann, C. Cirelli and U. Keller. *Combining attosecond XUV pulses with coincidence spectroscopy.* Rev. Sci. Instrum. **85**, 103113 (2014).

83. T. K. Jensen. Construction and Characterization of an Interferometer for the Stabilization of Attosecond Experiments (2015). Student Paper Lund University.

84. S. Ek. Interferometer Design for Attosecond Experiments (2015). Student Paper Lund University.

85. X. He, M. Miranda, J. Schwenke, O. Guilbaud, T. Ruchon, C. Heyl, E. Georgadiou, R. Rakowski, A. Persson, M. B. Gaarde and A. L'Huillier. *Spatial and spectral properties of the high-order harmonic emission in argon for seeding applications.* Phys. Rev. A **79**, 063829 (2009).

86. E. P. Wigner. *Lower Limit for the Energy Derivative of the Scattering Phase Shift.* Phys. Rev. **98**, 145–147 (1955).

87. H. Friedrich. *Theoretical atomic physics.* Springer Verlag (1994).

88. C. A. A. de Carvalho and H. M. Nussenzveig. *Time delay.* Physics Reports **364**, 83 – 174 (2002).

89. J. M. Dahlström, A. L'Huillier and A. Maquet. *Introduction to attosecond delays in photoionization.* J. Phys. B **45**, 183001 (2012).

90. M. Baggash and H. Rottke. *Phase differences in the photoemission from krypton in the fine-structure-split ionization channels* $^2P_{3/2}$ *and* $^2P_{1/2}$. Phys. Rev. A **92**, 013424 (2015).

91. M. Ya. Amusia, V. K. Ivanov, N. A. Cherepkov and L. V. Chernysheva. *Interference effects in photoionization of noble gas atoms outer s-subshells.* Phys. Lett. A **40**, 361–362 (1972).

92. M. Sabbar, S. Heuser, R. Boge, M. Lucchini, T. Carette, E. Lindroth, L. Gallmann, C. Cirelli and U. Keller. *Resonance Effects in Photoemission Time Delays.* Phys. Rev. Lett. **115**, 133001 (2015).

93. C. Cirelli, M. Sabbar, S. Heuser, R. Boge, M. Lucchini, L. Gallmann and U. Keller. *Energy dependent photoemission time delays of noble gas atoms using coincidence attosecond streaking.* IEEE J. Quant. Electron. **21**, 8700307 (2015).

94. R. Kienberger, E. Goulielmakis, M. Uiberacker, A. Baltuška, V. Yakovlev, F. Bammer, A. Scrinzi, Th. Westerwalbesloh, U. Kleineberg, U. Heinzmann, M. Drescher and F. Krausz. *Atomic transient recorder.* Nature **427**, 817 (2004).

95. T. Åberg. *Asymptotic Double-Photoexcitation Cross Sections of the Helium Atom.* Phys. Rev. A **2**, 1726–1729 (1970).

96. S. L. Sorensen, T. Åberg, J. Tulkki, E. Rachlew-Källne, G. Sundström and M. Kirm. *Argon 3s autoionization resonances.* Phys. Rev. A **50**, 1218 (1994).

97. U. Fano. *Effects of configuration interaction on intensities and phase shifts.* Phys. Rev. **124**, 1866 (1961).

98. Á. J. Galán, F. Martín and L. Argenti. *Two-photon finite-pulse model for resonant transitions in attosecond experiments.* arXiv preprint arXiv:1509.05814, Accepted in Phys. Rev. A (2015).

99. L. Roos. *Optimisation and Application of Intense High-Order Harmonic Pulses.* PhD thesis Lund University (2001).

100. J. M. Dahlström and E. Lindroth. *Study of attosecond delays using perturbation diagrams and exterior complex scaling.* J. Phys. B **47**, 124012 (2014).

101. J. Wätzel, A. S. Moskalenko, Y. Pavlyukh and J. Berakdar. *Angular resolved time delay in photoemission.* J. Phys. B **48**, 025602 (2015).

102. S. Heuser, Á. J. Galán, C. Cirelli, M. Sabbar, R. Boge, M. Lucchini, L. Gallmann, I. Ivanov, A. S. Kheifets, J. M. Dahlström, E. Lindroth, L. Argenti, F. Martín and U. Keller. *Time delay anisotropy in photoelectron emission from the isotropic ground state of helium.* arXiv preprint arXiv:1503.08966v2 (2015).

103. Á. J. Galán, L. Argenti and F. Martín. *Modulation of Attosecond Beating in Resonant Two-Photon Ionization.* Phys. Rev. Lett. **113**, 263001 (2014).

104. M. Drescher, M. Hentschel, R. Kienberger, M. Uiberacker, V. Yakovlev, A. Scrinzi, Th Westerwalbesloh, U. Kleineberg, U. Heinzmann and F. Krausz. *Time-resolved atomic inner-shell spectroscopy.* Nature **419**, 803–807 (2002).

105. A. Kivimäki, L. Pfeiffer, H. Aksela, E. Nõmmiste and S. Aksela. *Intensities of the xenon $N_{4,5}OO$ Auger electron spectrum revisited.* J. Electron Spectrosc. **101 - 103**, 43 – 47 (1999).